NEW TRENDS IN HIGH-ENERGY PHYSICS

Budva, Becici, Montenegro
2–8 October 2016

Proceedings of the Conference

JOINT INSTITUTE FOR NUCLEAR RESEARCH

NEW TRENDS IN HIGH-ENERGY PHYSICS

Conference

Budva, Becici, Montenegro
2–8 October 2016

Proceedings of the Conference

Dubna 2018

УДК 539.1(063)
ББК 22.3я431
N52

The contributions are reproduced directly from the originals.

New Trends in High-Energy Physics: Proceedings of the Conference
N52 (Budva, Becici, Montenegro, 2–8 October 2016). — Dubna: JINR, 2018. — 322 p.

ISBN 978-5-9530-0486-2

The Conference on New Trends in High-Energy Physics organized by the Joint Institute for Nuclear Research, Dubna, and Bogolyubov Institute for Theoretical Physics, National Academy of Sciences of Ukraine, was held at the Hotel Splendid, Conference Hall, Budva, Becici, Montenegro, on 2–8 October 2016.

The present Proceedings contain direct reproductions of authors' originals (reviews and short communications) that arrived at the Organizing Committee and are grouped somewhat loosely. We have united a number of sections. The contributions within each section are ordered according to the conference program. More conference information and pictures can be found on our site: http://indico-new.jinr.ru/event/ntihep2016.

Новые тенденции в физике высоких энергий: Труды конференции (Будва, Бечичи, Черногория, 2–8 октября 2016 г.). — Дубна: ОИЯИ, 2018. — 322 с.

ISBN 978-5-9530-0486-2

Конференция «Новые тенденции в физике высоких энергий», организованная Объединенным институтом ядерных исследований (Дубна) и Институтом теоретической физики им. Н.Н. Боголюбова НАН Украины (Киев), проходила в конференц-зале гостиницы «Splendid» (Черногория, Будва, Бечичи) 2–8 октября 2016 г.

Данный сборник содержит материалы (обзоры и короткие сообщения), присланные авторами в оргкомитет, сгруппированные в свободном порядке. Мы объединили ряд разделов. Статьи в каждом разделе упорядочены в соответствии с программой конференции. Более подробную информацию о конференции, а также фотографии можно найти на сайте: http://indico-new.jinr.ru/event/ntihep2016.

УДК 539.1(063)
ББК 22.3я431

ISBN 978-5-9530-0486-2

CONTENTS

SECTION "NEW COLLIDERS, FACILITIES, DETECTORS, COMPUTING AND DATA ANALYSES TECHNIQUES"

CONFERENCE PROGRAM

3 October 2016

09:00 - 10:30 **INTRODUCTION**
Chair: V. Bednyakov

09:00 N. Russakovich. **Opening Talk**
09:20 S. Bilenky. **Neutrino in the Standard Model and beyond**
09:55 D. Kazakov. **High energy behavior of maximally supersymmetric gauge theories**

10:30-10:50 **Coffee break**

10:50-12:30 **SECTION: "STANDARD MODEL AND BEYOND"**
Chair: V. Glagolev

10:50 G. Prodi. **The gravitational wave observatory and its first discoveries**
11:30 A. Krolak. **First detection of gravitational wave signals**
12:00 S. Dubnicka. **Prediction of Λ-hyperon magnetic FF and ratio $|G_E^\Lambda/G_M^\Lambda|$ in time-like region**

12:30-14:30 **Lunch time**

14:30-16:00 **SECTION: "ADVANCES IN THEORETICAL PHYSICS"**
Chair: D. Kazakov

14:30 A. Gladyshev. **Search for supersymmetry: the present status**
15:00 M. Krivoruchenko. **Longitudinal vector form factor in the pion-beta decay**
15:30 O.V. Nitescu. **New phase space calculations for β^+ and EC decay modes**

16:00-16:20 **Coffee break**

16:20-17:20 **SECTION: "ADVANCES IN THEORETICAL PHYSICS"**
Chair: A. Gladyshev

16:20 P. Matak. **Left-left squarks mixing in $K^+ \to \pi^+ \nu\nu$ decay**
16:50 N. Gromov. **Particles evolution in the early universe**

12:30-14:30 **Lunch time**

14:30-16:00 **PARALLEL SECTION: "STANDARD MODEL AND BEYOND"**
Chair: S. Dubnicka

14:30 N. Raicevic. **HERA Results on proton structure and hard QCD**
15:00 L. Adamczyk. **Diffractions at HERA**
15:30 M. Pesek. **Polarized Drell-Yan measurement at COMPASS**

16:00-16:20 **Coffee break**

16:20-17:50 **PARALLEL SECTION: "NEW FACILITIES, DETECTORS, COMPUTING AND DATA ANALYSES TECHNIQUES"**
Chair: N. Atanov

16:20 V. Baranov. **Particle tracking in the PEN experiment**
16:50 A. Simonenko. **The increase of the light collection from scintillation strip with hole for WLS fiber using various types of fillers**
17:20 Yu. Usov. **^{3}He-^{4}He dilution refrigerators, results, traditions, 50 years anniversary**

4 October 2016

09:00 - 10:30 **SECTION "NEUTRINO AND ASTROPARTICLE PHYSICS"**
Chair: R. Bernabei

09:00 Z. Djurcic. **Deep underground neutrino experiment: status and prospects**
09:30 D. Naumov. **Latest results from the Daya Bay reactor neutrino experiment**
10:00 Z. Djurcic. **Physics results from NOvA neutrino oscillation experiment**

10:30-10:50 **Coffee break**

10:50 - 12:30 **SECTION "NEUTRINO AND ASTROPARTICLE PHYSICS"**
Chair: D. Naumov

10:50 R. Bernabei. **Dark matter particles in the galactic halo**
11:30 I. Tkachev. **Axions as dark matter**
12:00 J.K. Hwang. **Elementary particles, dark candidate and new extended Standard Model**

12:30-14:30 **Lunch time**

14:30-16:00 **SECTION "NEUTRINO AND ASTROPARTICLE PHYSICS"**
Chair: I. Tkachev

14:30 T. Yano. **The recent results from Super-K**
15:00 V. Paolone. **Overview of recent results from the T2K experiment**
15:30 D. Svirida. **DANSS reactor antineutrino project: status and proof of principle**

16:00-16:20 **Coffee break**

16:20-17:50 **SECTION: "ADVANCES IN THEORETICAL PHYSICS"**
Chair: G. Lykasov

16:20 M. Ivanov. **Heavy quark physics and XYZ states in covariant quark model**

16:50 A. Liptaj. **Rare decay of heavy mesons in covariant confined quark model**

17:20 A. Afanasiev. **How to differentiate function based on integration operation**

12:30-14:30 **Lunch time**

14:30-16:00 **PARALLEL SECTION: "STANDARD MODEL AND BEYOND"**

Chair: M. Ivanov

14:30 D. Madigozhin. **Searches for lepton number violation and resonances in the $K^+ \to \pi\mu\mu$ decays at the NA48/2 experiment**

15:00 M. Mirra. **Neutral pion form factor measurement by the NA62 experiment**

15:30 J. Pinzinno. **Search for $K^+ \to \pi^+\nu\nu$ at NA62**

16:00-16:20 **Coffee break**

16:20-18:20 **PARALLEL SECTION: "NEW FACILITIES, DETECTORS, COMPUTING AND DATA ANALYSES TECHNIQUES"**

Chair: B. Sabirov

16:20 A. Volkov. **New type straws: properties and quality**

16:50 N. Khomutov. **Using the cathode surface of straw tube for measuring the track coordinate along the wire and increasing rate capability**

17:20 P. Zarubin. **Diffraction dissociation of relativistic nuclei in nuclear track emulsion**

17:50 I. Zarubina. **Recent applications of the technique of nuclear track emulsion**

5 October 2016

09:00 - 10:30 **SECTION "STANDARD MODEL AND BEYOND"**

Chair: G. Mitselmakher

09:00 A. Ivanov. **Search for new physics with CMS**

09:30 I. Yeletskikh. **Search for new physics at TeV scale in dilepton final states at ATLAS experiment**

10:00 G. Lykasov. **Heavy quark distributions in nucleon: collider tests**

10:30-10:50 **Coffee break**

10:50 - 12:30 **SECTION "STANDARD MODEL AND BEYOND"**

Chair: B. Kopeliovich

10:50 O. Igonkina. **Search for new exotic phenomena with the ATLAS detector at the LHC**

11:30 I. Tsukerman. **Review of Higgs results from the ATLAS experiment**

12:00 G. Mitselmakher. **Review of Higgs results from the CMS experiment**

12:30-14:30 **Lunch time**

09:00 - 10:30 **PARALLEL SECTION "NEUTRINO AND ASTROPARTICLE PHYSICS"**

Chair: V. Paolone

09:00 J. Kisiel. **ICARUS experiment: status and perspectives**

09:30 V. Pantuev. **Direct search of keV sterile neutrino in tritium beta decay by 'Troitsk ν-mass" experiment**

10:00 A. Babic. **Neutrinoless double-beta decay with emission of single electron**

10:30-10:50 **Coffee break**

EXCURSION

6 October 2016

09:00 - 10:30 **SECTION "STANDARD MODEL AND BEYOND"**
Chair: V. Glagolev

09:00 F. Happacher. **The Mu2e experiment at Fermilab**
09:30 I. Logashenko. **A new measurement of the anomalous magnetic moment of muon at Fermilab**
10:00 A. Dubnickova. **Reduction of total precise error of Muon g-2 anomaly and QED $\alpha(M^2z)$ by unitary&analytic model description of pseudoscalas meson nonet EM structure**

10:30-10:50 **Coffee break**

10:50 - 12:30 **SECTION "STANDARD MODEL AND BEYOND"**
Chair: R. Tsenov

10:50 R. Shicker. **ALISE results in pp, pA and AA collisions at the LHC**
11:30 Yu. Kulchitsky. **Two-particle Bose-Einstein correlations in pp collisions at 0.9 and 7 TeV measured with the ATLAS detector**
12:00 N. Pukhaeva. **Bose-Einstein correlation and color reconnection in particle physics**

12:30-14:30 **Lunch time**

14:30-16:00 **SECTION "STANDARD MODEL AND BEYOND"**
Chair: A. Dubnickova

14:30 D. Pocanic. **PEN and Nab: new precision tests of lepton and quark-lepton universality**
15:00 G. Rutar. **In search of $\mu \rightarrow e\gamma$: final result of the MEG experiment**
15:30 R. Tsenov. **A very intense neutrino super beam experiment for leptonic CP violation discovery based on the European spallation source linac**

16:00-16:20 **Coffee break**

16:20-17:50 **SECTION: "ADVANCES IN THEORETICAL PHYSICS"**
Chair: V. Melezhik

16:20 B. Kopeliovich. **Breakdown of QCD factorization in hard hadronic diffraction**

16:50 L. Csernai. **Shear, turbulence and its observable consequences in heavy ion reactions**
17:20 M. Nardi. **Heavy flavors in nucleus-nucleus and proton-nucleus collisions**

10:30-10:50 **Coffee break**

10:50 - 12:30 **PARALLEL SECTION "ADVANCES IN THEORETICAL PHYSICS"**
Chair: M. Hnatic

10:50 L. Jenkovszky. **Alastic and inelastic diffraction at the LHC**
11:30 C. Adamuscin. **Numerical values of f^F, f^D, f^S coupling constants in SU(3) invariant interaction lagrangian of vector-meson nonet with $1/2^+$ octet baryons**
12:00 E. Bartos. **Proton charge padius and its consistency with the experiments**

12:30-14:30 **Lunch time**

14:30-16:00 **PARALLEL SECTION: " ADVANCES IN THEORETICAL PHYSICS "**
Chair: L. Jenkovszky

14:30 M. Hnatic. **Quantum field theory methods in classical physics**
15:00 O. Solovtsova. **Twenty years of the analytic perturbation theory in QCD**
15:30 V. Melezhik. **Quantum simulations with sold atoms^ from solid state to high energy physics and cosmology**

16:00-16:20 **Coffee break**

16:20-17:50 **PARALLEL SECTION: "NEW FACILITIES, DETECTORS, COMPUTING AND DATA ANALYSES TECHNIQUES"**
Chair: N. Khomutov

16:20 B. Sabirov. **New technology application to modernization of Electron-positron linear collider (ILC)**
16:50 N. Atanov. **Solar-blind photodetectors with AlGaN photocathodes for light registration in UVC range**
17:20 A. Zaitsev. **Manifestation of the unstable nuclei in relativistic dissociation of the ^{10}B and ^{11}C nuclei**

7 October 2016

09:00 - 10:30 **SECTION "NEW COLLIDERS FOR BARYONIC MATTER STUDY"**
Chair: S. Dubnicka

09:00 R. Tsenov. **Status of the NICA project**
09:30 M. Pandurovich. **The CLIC physics potential**
10:00 V. Ryabov. **Recent results from PHENIX experiment at RHIC**

10:30-10:50 **Coffee break**

10:50 – 11:50 **SECTION "NEW COLLIDERS FOR BARYONIC MATTER STUDY"**
Chair: L. Jenkovszky

10:50 D. Kotov. **PHENIX results on leading particles and jets measured in Cu+Au collisions at RHIC**
11:30 L. Jenkovszky. **Closing**

EXCURSION

20:00 **FAREWELL PARTY**

SECTION "NEUTRINO, ASTROPARTICLE PHYSICS, STANDARD MODEL AND BEYOND"


There is no simple limit, where
This means that one cannot simply reduce the UV divergence and non-
renormalizability of a theory is not imposed when summing the whole
series
The knowledge of all loop form of the UV divergences makes it be
exploited


Comments on the phenomenology of massive excitations
The Standard Model and neutrinos
The simplest mechanism of the generation of neutrino masses


NEW TRENDS
IN HIGH-ENERGY PHYSICS
SPLENDID


NEW TRENDS
IN HIGH-ENERGY PHYSICS
2 October 2014 - 8 October 2014
SPLENDID


Prediction of Λ-hyperon magnetic FF and ratio
| G_E^Λ(t) | / | G_M^Λ(t) | in time-like region


SPLENDID


NEW TRENDS


NEW TRENDS
IN HIGH ENERGY PHYSICS


SPLENDID


NEW TRENDS
Jadran

Overview of neutrino masses and mixing

S. M. Bilenky

Joint Institute for Nuclear Research, Dubna, R-141980, Russia

Abstract

The status of neutrino oscillations is presented. The Standard Model and the Weinberg effective Lagrangian mechanism of the neutrino mass generation are discussed from the point of view of economy and simplicity.

1 Introduction

Idea of neutrino masses, mixing and oscillations was proposed by B. Pontecorvo in 1958 in Dubna [1]. This idea was further developed in the seventies by B. Pontecorvo, V. Gribov and myself [2, 3]. Different experiments on the search for neutrino oscillations were proposed at that time.

It took about thirty years of heroic efforts of many people to discover neutrino oscillations, first in the atmospheric Super-Kamiokande experiment [4] then in the solar SNO experiment [5] and in the reactor KamLAND experiment [6]. Strong indications in favor of neutrino transitions in the sun were found earlier in the pioneer Davis solar neutrino experiment [7] and in the solar neutrino experiments Kamiokande [8], GALLEX [9] and SAGE [10]. Discovery of neutrino oscillations was confirmed by the K2K [11], MINOS [12], T2K [13] and NOvA [14] accelerator neutrino experiments, by the Daya Bay [15], RENO [16] and Double Chooz [17] reactor neutrino experiments and by the solar neutrino experiment BOREXINO [18].

Discovery of the neutrino oscillations is the major recent discovery in the particle physics. In spite the full understanding of the origin of small neutrino masses and peculiar neutrino mixing requires new experimental data and, apparently, new theoretical ideas it is a common belief that small neutrino masses is a first beyond the Standard Model phenomenon found in the particle physics. In 2015 for the discovery of the neutrino oscillations T. Kajita and A. McDonald were awarded by the Nobel Prize.

In this talk I will consider

1. Present status of neutrino oscillations.
2. Role of neutrino in the Standard Model.
3. The most plausible (and the simplest) beyond the Standard Model mechanism of the generation of small neutrino masses.

2 Status of neutrino oscillations

Analysis of neutrino oscillation data is based on the assumption that neutrino interaction is the SM charged current and neutral current interaction given by the Lagrangians

$$\mathcal{L}_I^{CC}(x) = -\frac{g}{2\sqrt{2}} j_\alpha^{CC}(x) W^\alpha(x) + \text{h.c.}, \quad j_\alpha^{CC}(x) = 2 \sum_{l=e,\mu,\tau} \bar{\nu}_{lL}(x) \gamma_\alpha l_L(x) \tag{1}$$

and

$$\mathcal{L}_I^{NC}(x) = -\frac{g}{2\cos\theta_W} j_\alpha^{NC}(x) Z^\alpha(x), \quad j_\alpha^{NC}(x) = \sum_{l=e,\mu,\tau} \bar{\nu}_{lL}(x) \gamma_\alpha \nu_{lL}(x). \tag{2}$$

In the case of the neutrino mixing we have (see, for example, the review [19])

$$\nu_{lL}(x) = \sum_{i=1}^{3} U_{li}\, \nu_{iL}(x), \quad l = e, \mu, \tau \tag{3}$$

Here U is the unitary Pontecorvo-MNS [1, 20] mixing matrix and $\nu_i(x)$ is the field of the neutrino with mass m_i.

If the total lepton number L is conserved, ν_i are Dirac particles ($L(\nu_i) = -L(\bar{\nu}_i) = 1$). In this case the PNMS mixing matrix U^D is characterized by three mixing angles $\theta_{12}, \theta_{23}, \theta_{13}$ and one CP phase δ. If there are no conserved lepton numbers, ν_i are Majorana particles. The 3×3 mixing matrix has in this case the form

$$U^{Mj} = U^D\, S(\bar{\alpha})\,, \tag{4}$$

where $S(\bar{\alpha})$ is the phase matrix which is characterized by additional two Majorana phases: $S_{ik}(\bar{\alpha}) = S_i \delta_{ik}$, $S_1 = 1$, $S_{2,3} = e^{i\bar{\alpha}_{2,3}}$.

The CC Lagrangian (1) determines the notion of the *flavor neutrinos* ν_e, ν_μ, ν_τ. Flavor muon neutrino ν_μ is a particle which is produced together with μ^+ in the decay $\pi^+ \to \mu^+ + \nu_\mu$ or induces the reaction $\nu_\mu + N \to \mu^- + X$ etc. The state of the flavor neutrino ν_l with momentum $\vec{p}$ is given by *a coherent superposition of the states of neutrinos with definite masses*

$$|\nu_l\rangle = \sum_{i=1}^{3} U_{li}^* |\nu_i\rangle\,. \tag{5}$$

Here $|\nu_i\rangle$ is the state of neutrino with mass m_i, momentum $\vec{p}$ and energy $E_i = \sqrt{p^2 + m_i^2} \simeq E + \frac{m_i^2}{2E}$ ($p^2 \gg m_i^2$). This relation is a consequence of the Heisenberg uncertainty relation. The relation (5) means that we can not resolve production of ultrarelativistic neutrinos with different masses in weak decays and neutrino reactions.

Small neutrino mass-squared differences can be resolved in special experiments with a large distance between neutrino source and neutrino detector. A possibility to resolve neutrino mass-squared differences is based on the time-energy uncertainty relation [21]

$$\Delta E\, \Delta t \geq 1\,. \tag{6}$$

In the neutrino case

$$\Delta E = |E_i - E_k| \simeq \frac{|\Delta m_{ki}^2|}{2E}, \quad \Delta t = t \simeq L. \tag{7}$$

Here $\Delta m_{ki}^2 = m_i^2 - m_k^2$ and L is the distance between neutrino source and detector. From (6) we obtain the following condition

$$\frac{|\Delta m_{ki}^2|}{2E}\, L \geq 1\,. \tag{8}$$

Thus in order to reveal the production of neutrinos with energy difference $|E_i - E_k|$ we need to perform an experiment at a source-detector distance L which satisfy the inequality (8).

If at the time $t = 0$ the flavor neutrino ν_l is produced at the time $t > 0$ the neutrino state is given by

$$|\nu_l\rangle_t = e^{-iHt}\, |\nu_l\rangle = \sum_i |\nu_i\rangle\, e^{-iE_i t}\, U_{li}^* = \sum_{l'} |\nu_{l'}\rangle \left(\sum_i U_{l'i}\, e^{-iE_i t}\, U_{li}^*\right). \tag{9}$$

Here H is the free Hamiltonian. From (9) for the probability of the $\nu_l \to \nu_{l'}$ transition we find the following expression

$$P(\nu_l \to \nu_{l'}) = |\sum_i U_{l'i}\, e^{-2i\Delta_{pi}}\, U_{li}^*|^2 = |\delta_{l'l} - 2i \sum_{i \neq p} U_{l'i}\, e^{-i\Delta_{pi}} \sin\Delta_{pi}\, U_{li}^*|^2\,, \tag{10}$$

where p is an arbitrary fixed index and $\Delta_{pi} = \frac{\Delta m_{pi}^2 L}{4E}$.

For the probability of $\bar{\nu}_l \to \bar{\nu}_{l'}$ transition we have

$$P(\bar{\nu}_l \to \bar{\nu}_{l'}) = |\delta_{l'l} - 2i \sum_{i \neq p} U_{l'i}^*\, e^{-i\Delta_{pi}} \sin\Delta_{pi}\, U_{li}|^2 \tag{11}$$

From (4) follows that

$$U_{l'i}^{Mj} U_{li}^{Mj*} = U_{l'i}^D U_{li}^{D*}\,. \tag{12}$$

We conclude from (10), (11) and (12) that the study of neutrino oscillations does not allow to reveal the nature of neutrinos with definite masses (Dirac or Majorana?) [22].

It follows from (10) and (11) that $\nu_l \to \nu_{l'}$ ($\bar{\nu}_l \to \bar{\nu}_{l'}$) transition probability is given by the following expression

$$\mathrm{P}(\nu_l \to \nu_{l'})(\mathrm{P}(\bar{\nu}_l \to \bar{\nu}_{l'})) = \delta_{l'l} - 4\sum_i |U_{li}|^2(\delta_{l'l} - |U_{l'i}|^2)\,\sin^2\Delta_{pi}$$
$$+8\sum_{i>k}[\mathrm{Re}\,(U_{l'i}U^*_{li}U^*_{l'k}U_{lk})\,\cos(\Delta_{pi}-\Delta_{pk})$$
$$\pm\,\mathrm{Im}\,(U_{l'i}U^*_{li}U^*_{l'k}U_{lk})\,\sin(\Delta_{pi}-\Delta_{pk})]\,\sin\Delta_{pi}\sin\Delta_{pk}. \qquad (13)$$

Usually neutrino masses are labeled in such a way that

$$m_2 > m_1, \qquad \Delta m^2_{12} = \Delta m^2_S > 0\,, \qquad (14)$$

where Δm^2_S is called the solar mass-squared difference. From analysis of the neutrino oscillation data it was found that another neutrino mass-squared difference Δm^2_A, which is called atmospheric, is about 30 times larger than the solar one. There are two possibilities for the third mass m_3 and, correspondingly, for the neutrino mass spectrum

1. Normal ordering (NO) $m_3 > m_2 > m_1$, $\quad \Delta m^2_{23} = \Delta m^2_A$.
2. Inverted ordering (IO) $m_2 > m_1 > m_3$, $\quad |\Delta m^2_{13}| = \Delta m^2_A$.

Determination of the character of the neutrino mass spectrum is one of the major problem of the present and future neutrino oscillation experiments. Future reactor neutrino experiments JUNO [23] and RENO-50 [24], in which a distance between reactors and the detector will be about 60 km, are planned to solve this problem. From (13) for the probability of the reactor $\bar{\nu}_e$'s to survive in the case of the normal and inverted neutrino mass spectrum we find the following expressions

$$\mathrm{P}^{\mathrm{NO}}(\bar{\nu}_e \to \bar{\nu}_e) = 1 - \sin^2 2\theta_{13}\sin^2\Delta_A$$
$$-(\cos^4\theta_{13}\sin^2 2\theta_{12} + \cos^2\theta_{12}\sin^2 2\theta_{13})\sin^2\Delta_S$$
$$-2\sin^2 2\theta_{13}\cos^2\theta_{12}\cos(\Delta_A+\Delta_S)\sin\Delta_A\sin\Delta_S. \qquad (15)$$

and

$$\mathrm{P}^{\mathrm{IO}}(\bar{\nu}_e \to \bar{\nu}_e) = 1 - \sin^2 2\theta_{13}\sin^2\Delta_A$$
$$-(\cos^4\theta_{13}\sin^2 2\theta_{12} + \sin^2\theta_{12}\sin^2 2\theta_{13})\sin^2\Delta_S$$
$$-2\sin^2 2\theta_{13}\sin^2\theta_{12}\cos(\Delta_A+\Delta_S)\sin\Delta_A\sin\Delta_S. \qquad (16)$$

The values of the neutrino oscillation parameters obtained from the global analysis of existing neutrino oscillation data are presented in the Table I.

Table I. The values of the neutrino oscillation parameters [25]

Parameter	Normal Ordering	Inverted Ordering
$\sin^2\theta_{12}$	$0.306^{+0.012}_{-0.012}$	$0.306^{+0.012}_{-0.012}$
$\sin^2\theta_{23}$	$0.441^{+0.027}_{-0.021}$	$0.587^{+0.020}_{-0.024}$
$\sin^2\theta_{13}$	$0.02166^{+0.00075}_{-0.00075}$	$0.02179^{+0.00076}_{-0.00076}$
δ (in °)	(261^{+51}_{-59})	(277^{+40}_{-46})
Δm^2_S	$(7.50^{+0.19}_{-0.17})\cdot 10^{-5}$ eV^2	$(7.50^{+0.19}_{-0.17})\cdot 10^{-5}$ eV^2
Δm^2_A	$(2.524^{+0.039}_{-0.040})\cdot 10^{-3}$ eV^2	$(2.514^{+0.038}_{-0.041})\cdot 10^{-3}$ eV^2

Thus existing data do not allow to distinguish the normal and inverted neutrino mass ordering and we see from Table I that

1. Neutrino oscillations parameters are known with accuracies (3 -10)%.
2. The CP phase δ is practically unknown.

The major aims of future neutrino oscillation experiments are

- to determine neutrino oscillation parameters with 1% accuracy,
- to establish the neutrino mass ordering,
- to measure the CP phase δ.

Apparently, future neutrino experiments could reveal a true mechanism of generation of small neutrino masses and peculiar neutrino mixing which is very different from the quark mixing. In the last part of this brief overview we will discuss the plausible mechanism of the generation of small (Majorana) neutrino masses.

3 Neutrino in the Standard Model

I will start with a few historical remarks. In 1928 Dirac proposed the four-component equation for a relativistic spin 1/2 particle. Now we know the origin of four components: the four-component Dirac field $\psi(x)$ (in the framework of QFT) is *the field of particles and antiparticles.*

In 1929 Weyl put the following question: can we find for a relativistic spin 1/2 particle a two-component equation? Weyl introduced the two-component spinors

$$\psi_L(x) = \frac{1}{2}(1-\gamma_5)\psi(x), \quad \psi_R(x) = \frac{1}{2}(1-\gamma_5)\psi(x). \qquad (17)$$

and showed that $\psi_L(x)$ and $\psi_R(x)$ satisfy the following two-component equations (which are called Weyl equations)

$$i\gamma^\alpha \partial_\alpha \psi_L(x) = 0, \quad i\gamma^\alpha \partial_\alpha \psi_R(x) = 0 \tag{18}$$

The Weyl equations, however, are not invariant under the space inversion

$$'_{L,R}(x') = \eta\gamma^0 \psi_{L,R}(x), \tag{19}$$

where $x' = (x^0, -\vec{x})$ and η is a phase factor.

In the thirties (and many years later) there was a common belief that the conservation of the parity is a law of nature. This was the reason why the Weyl equations were rejected.

After discovery of the parity violation in weak decays it was assumed that neutrino is a massless, Weyl particle and neutrino field is $\nu_L(x)$ or $\nu_R(x)$ (the two-component neutrino theory by Landau [26], Lee and Yang [27] and Salam [28]).

From the two-component theory followed that

1. the large violation of parity in the β-decay and other weak processes had to be observed,

2. the helicity of neutrino (antineutrino) had to be equal to -1 (+1) in the case of $\nu_L(x)$ and +1 (-1) in the case of $\nu_R(x)$.

The crucial test of the two-component neutrino theory was performed by the classical Goldhaber et al experiment[29] in which the neutrino helicity was measured. The authors of the experiment concluded: "our result is compatible with 100 % negative helicity of neutrino" (neutrino field is $\nu_L(x)$).

The field $\nu_L(x)$ is the field of left-handed Dirac neutrino ($L = 1, \quad h = -1$) and right-handed Dirac antineutrino ($L = -1, \quad h = 1$). However, theories with massless Dirac and Majorana neutrinos are equivalent. Thus $\nu_L(x)$ can be considered as a field of left-handed ($h = -1$) and right-handed ($h = 1$) Majorana neutrino. Let us stress that *the two-component neutrino is the most economical possibility: two degrees of freedom.* In the general Dirac case there are four degrees of freedom.

The Standard Model started with the theory of the two-component, massless, left-handed neutrino. It is based on the following principles

1. The local gauge $SU_L(2) \times U_Y(1)$ invariance of massless fields.

2. The unification of the weak and electromagnetic interactions.

3. The Brout-Englert-Higgs mechanism of mass generation.

The Standard Model is in a perfect agreement with experiment: its most impressive prediction, existence of the scalar Higgs boson, was confirmed by recent LHC experiments. We will present some arguments that the Standard Model teach us that *the simplest, most economical possibilities are likely to be correct.*

Neutrinos are produced in weak decays together with leptons. $SU_L(2)$ is *the simplest symmetry* which allows to unify leptons and neutrinos (and up and down quarks). The fields of left-handed, massless, Weyl fields of neutrinos and leptons are components of doublets

$$\overset{lep}{}_{eL} = \begin{pmatrix} \nu'_{eL} \\ e'_L \end{pmatrix}, \quad \overset{lep}{}_{\mu L} = \begin{pmatrix} \nu'_{\mu L} \\ \mu'_L \end{pmatrix}, \quad \overset{lep}{}_{\tau L} = \begin{pmatrix} \nu'_{eL} \\ e'_L \end{pmatrix}. \tag{20}$$

The leptonic electromagnetic current is given by the expression

$$j^{EM}_\alpha = -(\sum_{l=e,\mu,\tau} \bar{l}'_L \gamma_\alpha l'_L + \sum_{l=e,\mu,\tau} \bar{l}'_R \gamma_\alpha l'_R) \tag{21}$$

in which left-handed *and right-handed* lepton fields enter. Thus in order to include the electromagnetic interaction we have to enlarge the symmetry group. The *minimal enlargement* is $SU(2)_L \times U_Y(1)$ group, where $U_Y(1)$ is the group of the hypercharge Y determined by the Gell-Mann-Nishijima relation

$$Q = T_3 + \frac{1}{2}Y, \tag{22}$$

where Q is the charge and T_3 is the third projection of the isospin.

From the requirements of the local $SU(2)_L \times U_Y(1)$ invariance follow that gauge vector fields must exist. The standard electroweak interaction of fermions and vector gauge $W^\pm, Z^0$ bosons and γ-quanta

$$\mathcal{L}_I = \left(-\frac{g}{2\sqrt{2}} j^{CC}_\alpha W^\alpha + \text{h.c}\right) - \frac{g}{2\cos\theta_W} j^{\text{NC}}_\alpha Z^\alpha - j^{EM}_\alpha A^\alpha \tag{23}$$

is the *minimal* (compatible with the local gauge invariance) interaction.

The Standard Model mechanism of mass generation is the Brout-Englert-Higgs mechanism of the spontaneous symmetry breaking [30, 31]. It is based on the assumption of the existence of scalar Higgs fields. In order to generate masses of $W^\pm$ and Z^0 vector bosons three Goldsone degrees of freedom are needed. Thus *a minimal possibility* is a doublet of complex Higgs fields (four degrees of freedom). In such a theory it is predicted that *one neutral scalar Higgs boson* must exist. This prediction was perfectly confirmed by the LHC experiments.

Lepton (and quark) masses and mixing are generated by the $SU_L(2) \times U_Y(1)$ invariant Yukawa interaction. For leptons we have

$$\mathcal{L}_Y^{lep} = -\sqrt{2} \sum_{l_1,l_2} \bar{\psi}_{l_1 L}^{lep} Y_{l_1 l_2} l'_{2R}\, \phi + \text{h.c.} \tag{24}$$

Here

$$\phi = \begin{pmatrix} \phi_+ \\ \phi_0 \end{pmatrix} \tag{25}$$

is the Higgs doublet and Y is a complex 3×3 Yukawa matrix. If we choose

$$\phi = \begin{pmatrix} 0 \\ \frac{v+H}{\sqrt{2}} \end{pmatrix} \tag{26}$$

where $v = (\sqrt{2}G_F)^{-1/2} \simeq 246$ GeV is the vacuum expectation value (vev) of the Higgs field and H is the field of the Higgs boson, the electroweak symmetry will be spontaneously broken and Yukawa interaction (24) generates the Dirac mass term

$$\mathcal{L}^D = -\sum_{l_1,l_2} \bar{l}'_{1L}\, Y_{l_1 l_2}\, l'_{2R}\, v + \text{h.c} = -\sum_{\text{l=e,}\mu,\tau} \text{m}_\text{l}\, \bar{\text{l}}\, \text{l}, \tag{27}$$

where

$$m_l = y_l\, v. \tag{28}$$

Here m_l is the lepton mass, and the Yukawa coupling y_l is the eigenvalue of the matrix Y.

The characteristic feature of the Brout-Englert-Higgs mechanism of the mass generation is a *proportionality of the lepton masses to the vacuum expectation value* v (masses of quarks, $W^\pm$ and Z^0 bosons are also proportional to v).

The Unification of the weak and electromagnetic interactions requires that in the Standard Model Lagrangian enter left-handed and right-handed fields of charged fermions. Thus for the generation of the Dirac lepton (and quark) masses via the Yukawa interaction we do not need additional degrees of freedom.

Neutrino have no direct electromagnetic interaction. In order to generate neutrino masses via the standard mechanism of the spontaneous symmetry breaking we need to assume that in Standard Model Lagrangian enter not only left-handed neutrino fields but also right-handed fields (additional degrees of freedom). On the basis of general arguments of economy and simplicity it is natural to assume that *neutrinos in the Standard Model are*

massless, two-component, left-handed Weyl particles.[1] In order to generate neutrino masses and mixing we need a new beyond the Standard Model mechanism.

4 The most economical beyond the Standard Model mechanism of neutrino mass generation

A neutrino mass term is a Lorenz-invariant product of left-handed and right-handed components of neutrino fields. Can we build a neutrino mass term if we use only left-handed fields ν_{lL}? The answer to this question was given many years ago by Gribov and Pontecorvo [2]. It is possible to built a neutrino mass term in which only flavor fields ν_{lL} enter, *if we assume that the total lepton number L is not conserved.* In fact, in this case we can built the following mass term

$$\mathcal{L}^{\text{M}} = -\frac{1}{2} \sum_{l',l} \bar{\nu}_{l'L}\, M_{l'l} (\nu_{lL})^c + \text{h.c.}. \tag{29}$$

Here the conjugated field $(\nu_{lL})^c = C(\bar{\nu}_{lL})^T$ is *right-handed component* (C is the matrix of the charge conjugation) and M is a 3×3 symmetrical matrix.

The Lagrangian (29) is not invariant under the global phase transformations (does not conserve the total lepton number L). As a result, after the diagonalization of the mass matrix

$$M = U\, m\, U^T, \quad U^\dagger U = 1, \quad m_{ik} = m_i \delta_{ik}, \quad m_i > 0 \tag{30}$$

we come to the standard Majorana mass term

$$\mathcal{L}^{\text{Mj}} = -\frac{1}{2} \sum_{i=1}^{3} m_i\, \bar{\nu}_i \nu_i \tag{31}$$

Here

$$\nu_i = \nu_i^c = C\bar{\nu}_i^T \tag{32}$$

[1] If we assume that neutrino masses are generated by the Higgs mechanism, in this case we have $m_i = y_i^\nu\, v$. Absolute values of neutrino masses at present are not known. From existing upper bounds on neutrino masses and from neutrino oscillation data we can conclude that the heaviest neutrino mass m_3 is in the range ($5 \cdot 10^{-2} \leq m_3 \leq 1$ eV) and the Yukawa constant y_3^ν is in the range ($2 \cdot 10^{-13} \leq y_3^\nu \leq 4 \cdot 10^{-12}$). For other particles of the third family we have $y_t \simeq 0.7$, $y_b \simeq 1.7 \cdot 10^{-2}$, $y_\tau \simeq 0.7 \cdot 10^{-2}$. Thus, the neutrino Yukawa coupling y_3^ν is more than nine orders of magnitude smaller than Yukawa couplings of other particles of the third family. It is very unlikely that neutrino masses are of the same origin as masses of lepton and quarks.

is the field of the Majorana neutrino with the mass m_i. The flavor field ν_{lL} is given by the mixture of the fields of the Majorana neutrinos with definite masses

$$\nu_{lL} = \sum_{i=1}^{3} U_{li}\ \nu_{iL}, \quad l = e, \mu, \tau. \tag{33}$$

The approach to the neutrino masses and mixing, we have considered, is purely phenomenological one. Neutrino masses m_i and elements of the mixing matrix U are *parameters* which must be determined from experiments. The relation (33) gives a framework which allow us to analyze the data of neutrino oscillation experiments, experiments on the search for neutrinoless double β-decay etc. We have no any explanation of the smallness of neutrino masses.

However, it is important to stress that *the Majorana mass term (29) is only possible mass term which can be built with the help of left-handed neutrino fields* ν_{lL}.

We will consider now the effective Lagrangian approach [32] which allow us

- to obtain the Majorana mass term for neutrinos,
- to find some explanation of the smallness of neutrino masses,
- to predict existence of heavy Majorana fermions.

The method of the effective Lagrangian is a powerful, general method which allows to describe effects of a beyond the Standard Model physics. The effective Lagrangian is a nonrenormalizable dimension five or more operator invariant under the $SU_L(2) \times U_Y(1)$ transformations and built from the Standard Model fields. In order to generate the neutrino mass term we need to built an effective Lagrangian which is quadratic in the neutrino fields.

Let us consider the $SU_L(2) \times U_Y(1)$ invariant product

$$(\bar{\psi}^{lep}_{lL}\ \tilde{\phi})\ , \tag{34}$$

where ψ^{lep}_{lL} is the lepton doublet (see (20)) and $\tilde{\phi} = i\tau_2\phi^*$ is the conjugated Higgs doublet. After the spontaneous breaking of the electroweak symmetry we have

$$(\bar{\psi}^{lep}_{lL}\ \tilde{\phi}) = \frac{v+H}{\sqrt{2}}\bar{\nu}'_{lL}\ . \tag{35}$$

From this expression it is obvious that the $SU_L(2)\times U_Y(1)$ invariant effective Lagrangian [32]

$$\mathcal{L}^{\rm eff}_I = -\frac{1}{\Lambda}\sum_{l_1,l_2}(\bar{\psi}^{lep}_{l_1L}\tilde{\phi})\ X'_{l_1l_2}\ C\ (\bar{\psi}^{lep}_{l_2L}\tilde{\phi})^T + \text{h.c.} \tag{36}$$

generates a neutrino mass term. The operator in Eq. (36) has a dimension five. Thus Λ has a dimension of a mass and X' is a dimensionless 3×3 symmetrical matrix. Let us stress the following

1. The Lagrangian (36) is the only possible dimension five effective Lagrangian which can generate a neutrino mass term.
2. The effective Lagrangian (36) does not conserve the total lepton number L.
3. The constant Λ characterizes a scale of a beyond the Standard Model physics.

After the spontaneous symmetry breaking the Lagrangian (36) generates the Majorana mass term

$$\mathcal{L}^{\rm M} = -\frac{1}{2}\frac{v^2}{\Lambda}\sum_{l_1,l_2}\bar{\nu}_{l_1L}\,X_{l_1l_2}(\nu_{l_2L})^c + \text{h.c.}. \tag{37}$$

The symmetrical matrix X can be presented in the diagonal form

$$X = U\ x\ U^T, \quad U^\dagger\ U = 1, \quad x_{ik} = x_i\delta_{ik}, \quad x_i > 0. \tag{38}$$

From (37) and (38) we have

$$\mathcal{L}^{\rm M} = -\frac{1}{2}\sum_{i=1}^{3} m_i\ \bar{\nu}_i\nu_i, \quad \nu_{lL} = \sum_{i=1}^{3} U_{li}\ \nu_{iL} \tag{39}$$

Here

$$\nu_i = \nu_i^c = C\ \bar{\nu}_i^T \tag{40}$$

is the field of the neutrino Majorana with the mass

$$m_i = \frac{v^2}{\Lambda}\ x_i\ , \tag{41}$$

where x_i is the eigenvalue of the matrix X.

As we discussed before, the Standard Model masses are proportional to $v \simeq 246$ GeV with dimensionless coefficients. Standard Model neutrino

masses can be small only if coefficients of proportionality are extremely small.

Majorana neutrino masses generated by the effective Lagrangian (36) are proportional to $\frac{v}{\Lambda}\, v$. We have in this case an additional factor

$$\frac{v}{\Lambda} = \frac{\text{scale of SM}}{\text{scale of a new physics}}. \tag{42}$$

Smallness of neutrino masses can be ensured if we assume that a scale Λ of a new lepton number violating physics is much larger than the electroweak scale v. This is a natural assumption, no fine-tuning is required.

Uncertainties connected with the factors x_i do not allow to determine the scale of a new physics Λ in a model independent way. Nevertheless $\Lambda \gg v$ apparently is the most plausible possibility. In fact, let us assume hierarchy of neutrino masses ($m_1 \ll m_2 \ll m_3$). In this case for the third family we find

$$\Lambda \simeq x_3 \frac{v^2}{m_3} \simeq x_3 \frac{v^2}{\sqrt{\Delta m^2_A}}. \tag{43}$$

From this relation we have

$$\Lambda \simeq 1.2 \cdot 10^{15}\, x_3 \text{ GeV}. \tag{44}$$

If we assume that $\Lambda \simeq$ TeV in this case $x_3 \simeq 10^{-12}$ (too small, fine tuning). If $x_3 \simeq 1$ in this case $\Lambda \simeq 10^{15}$ GeV (GUT scale).

The effective Lagrangian (36) could be a result of an exchange of virtual heavy Majorana leptons between lepton-Higgs pairs.[2] In fact, let us assume that exist heavy Majorana leptons N_i ($i = 1, 2, ...n$), singlets of $SU_L(2) \times U_Y(1)$ group, which have the following $SU_L(2) \times U_Y(1)$ invariant Yukawa interaction

$$\mathcal{L}^Y_I = -\sqrt{2} \sum_{l,i} \bar{\psi}^{lep}_{lL}\, \tilde{\phi}\, y'_{li}\, N_{iR} + \text{h.c.}\,. \tag{45}$$

Here y'_{li} are dimensionless Yukawa coupling constants and $N_i = N^c_i$ is the field of Majorana leptons with mass M_i.

In the second order of the perturbation theory at $Q^2 \ll M^2_i$ (Q is the momentum of the virtual N_i) we obtain effective Lagrangian

$$\mathcal{L}^{\text{eff}} = -\sum_{l_1,l_2} (\bar{\psi}^{lep}_{l_1 L}\, \tilde{\phi}) \left(\sum_i y'_{l_1 i} \frac{1}{M_i} y'_{l_2 i}\right) (\tilde{\phi}^T\, (\,{}^{lep}_{l_2 L})^c) + \text{h.c.}. \tag{46}$$

[2]The classical example of an effective Lagrangian is the Fermi Lagrangian of the β-decay. As we know today, this Lagrangian is generated by the exchange of the virtual charged $W^{\pm}$-bosons between $e - \nu$ and $p - n$ pairs. It is a product of the Fermi constant which has dimension M^{-2} and the dimension six four-fermion operator.

This Lagrangian coincides with the Weinberg effective Lagrangian (36). The matrix $\frac{1}{\Lambda}\, X'$ is given by the relation

$$\frac{1}{\Lambda}\, X'_{l_1 l_2} = \sum_i y'_{l_1 i} \frac{1}{M_i} y'_{l_2 i} \tag{47}$$

After the spontaneous symmetry breaking from (46) we find the following Majorana mass term

$$\mathcal{L}^{\text{M}} = -\frac{1}{2} \sum_{l_1,l_2} \bar{\nu}_{l_1 L} \left(\sum_i y_{l_1 i} \frac{v^2}{M_i} y_{l_2 i}\right) (\nu_{l_2 L})^c + \text{h.c.}. \tag{48}$$

Here $y = V^{\dagger}_L y'$ where the matrix V_L connects flavor and primed neutrino fields ($\nu'_L = V_L \nu_L$).

It follows from (48) that the scale of a new lepton-number violating physics is determined by masses of heavy Majorana leptons. In spite for uncertainties connected with Yukawa coupling constants y_{li}, it is natural to assume that $M_i \gg v$. Let us notice that the mechanism of the generation of neutrino masses, we have considered, is equivalent to the standard seesaw mechanism [33].

The effective Lagrangian (seesaw) mechanism of the neutrino mass generation imply that

1. neutrinos with definite masses ν_i are Majorana particles. Investigation of the neutrinoless double β-decay of some even-even nuclei is the most sensitive way of determination of the nature of neutrinos with definite masses. The probability of this process is proportional to the effective Majorana mass $m_{\beta\beta} = \sum_{i=1}^{3} U^2_{ei} m_i$. From existing data it follows that $|m_{\beta\beta}| \leq (1.4 - 4.5)\ 10^{-1}$ eV. In future experiments the sensitivity $|m_{\beta\beta}| \simeq$ a few 10^{-2} eV will be reached (see review [34])

2. the number of neutrinos with definite masses must be equal to the number of the flavor neutrinos (three), i.e. no transitions of flavor neutrinos into sterile states are allowed. Indications in favor of such transitions were obtained in several short baseline experiments: LSND ($\bar{\nu}_\mu \to \bar{\nu}_e$), MiniBooNE ($\nu_\mu \to \nu_e$, $\bar{\nu}_\mu \to \bar{\nu}_e$), reactor ($\bar{\nu}_e \to \bar{\nu}_e$) and source ($\nu_e \to \nu_e$). However, in the recent experiments (MINOS, DayaBay, IceCube) no indications in favor of transitions into sterile states were found and strong tension with old data were obtained. More than 20 new accelerator, reactor and source experiments on the search for sterile neutrinos are in preparation at present (see [35, 36]).

3. heavy Majorana leptons with masses much larger than v must exist. Such leptons can be produced in the early Universe. Their CP violating decays is one of the most attractive explanation of the barion asymmetry of the Universe (see review [37]).

5 Conclusion

We reviewed here briefly the status of neutrino mixing and oscillations.

We stressed that from the success of the Standard Model we can conclude that in the framework of general principles, the Standard Model is based on, Nature chooses the simplest possibilities. Massless, two-component, Weyl particle is the simplest possibility for the Standard Model neutrino.

There is one possible lepton number violating effective Lagrangian which (after spontaneous symmetry breaking) generates the Majorana neutrino mass term, the only possible neutrino mass term in the case of the left-handed neutrino fields. Neutrino masses in the effective Lagrangian approach are naturally small because a new, lepton-number violating scale Λ is much larger than the electroweak scale v. The effective Lagrangian which generate the neutrino mass term is the only effective Lagrangian of the dimension five (proportional to $\frac{1}{\Lambda}$). This means that *neutrino masses are the most sensitive probe of a new physics at a scale which is much larger than the electroweak scale.*

I acknowledge the support of the RFFI grant 16-02-01104 and I am thankful the theory group of TRIUMF for the hospitality.

References

[1] B. Pontecorvo, J.Exptl. Theoret. Phys. **33**, 549(1957) [Sov. Phys. JETP **6**, 429(1958)]; J.Exptl. Theoret. Phys. **34**, 247(1958) [Sov. Phys. JETP **7**, 172(1958)].

[2] V. Gribov and B. Pontecorvo, Phys. Lett. **B28**, 493 (1969).

[3] S.M. Bilenky and B. Pontecorvo, Phys. Rep. **41**, 225 (1978).

[4] Y. Fukuda *et al.*, Super-Kamiokande Collaboration , Phys. Rev.Lett. **81**, 1562 (1998).

[5] Q. R. Ahmad *et al.* , SNO Collaboration, Phys. Rev. Lett. **89**, 011301 (2002).

[6] T. Araki *et al.* ,KamLAND Collaboration, Phys. Rev. Lett.**94**, 081801 (2005).

[7] B. T. Cleveland *et al.*, Astrophys. J. **496**, 505 (1998).

[8] Y. Fukuda *et al.*, Kamiokande, Phys. Rev. Lett. **77** , 1683 (1996).

[9] M. Altmann*et al.*, GNO Collaboration, Phys. Lett. **B616**, 174 (2005).

[10] J. N. Abdurashitov *et al.*, SAGE Collaboration, J. Exp. Theor.Phys. **95**, 181 (2002).

[11] M. H. Ahn *et al.*, K2K Collaboration, Phys. Rev. **D74**, 072003 (2006).

[12] P. Adamson *et al.*, MINOS Collaboration, Phys. Rev. Lett. **110**, 251801, (2013).

[13] K. Abe *et al.*, T2K Collaboration, Phys. Rev. Lett. **112**, 18180 (2014).

[14] P. Adamson *et al.*, NOvA Collaboration, arXiv:1701.05891.

[15] F. An *et al.*, Daya Bay Collaboration, Phys. Rev. Lett. **112**, 061801, (2014).

[16] S. B. Kim *et al.*, RENO Collaboration, Phys. Rev. Lett. **108**, 191802, (2012).

[17] Y. Abe *et al.*, Double Chooz Collaboration, Phys. Lett. **B723**, 66 (2013).

[18] G. Bellini *et al.*, BOREXINO Collaboration, Nature. **512**, 383 (2014).

[19] S. M. Bilenky and S.T. Petcov, Rev.Mod.Phys. **59**, 671 (1987).

[20] Z. Maki, M. Nakagava and S. Sakata, Prog. Theor. Phys. **28**, 870 (1962).

[21] S. M. Bilenky, F. von Feilitzsch and W. Potzel, J. Phys. **G 38**, 115002 (2011).

[22] S. M. Bilenky, J. Hosek and S.T. Petcov, Phys. Lett. **94**, 495 (1980).

[23] F. An *et al.*,JUNO Collaboration, J. Phys. G **43** no.3, 030401 (2016), arXiv:1507.05613.

[24] S. B. Kim, Nucl. Part. Phys. Proc. **265-266**, 93 (2015), arXiv:1412.2199.

[25] I. Esteban, M. C. Gonzalez-Garcia, M. Maltoni, I. Martinez-Soler and T. Schwetz, JHEP **1701**, 087 (2017), arXiv:1611.01514.

[26] L. D. Landau, Nucl. Phys. **3** , 127 (1957).

[27] T. D. Lee and C. N. Yang, Phys. Rev. **105**, 1671 (1957).

[28] A. Salam, Nuovo Cim. **5** , 299 (1957).

[29] M. Goldhaber, L. Grodzins and A. W. Sunyar, Phys. Rev. **109**, 1015 (1958).

[30] F. Englert, R. Brout, Phys. Rev. Lett. **13**, 321 (1964).

[31] P. W. Higgs, Phys. Lett. **12**, 132 (1964).

[32] S. Weinberg, Phys. Rev. Lett. **19**, 1264 (1967).

[33] P. Minkowski, Phys. Lett. **B 67**, 421(1977); M. Gell-Mann, P. Ramond and R. Slansky, in *Supergravity*, p. 315, edited by F. van Nieuwenhuizen and D. Freedman, North Holland, Amsterdam, (1979); T. Yanagida, Proc. of the *Workshop on Unified Theory and the Baryon Number of the Universe*, KEK, Japan, (1979); S.L. Glashow, NATO Adv.Study Inst. Ser. B Phys. **59**, 687 (1979); R.N. Mohapatra and G. Senjanović, Phys. Rev. **D23**, 165 (1981).

[34] S. M. Bilenky and C. Giunti, Int. J. Mod. Phys. A **30** no.04n05, 1530001 (2015), arXiv:1411.4791.

[35] C. Giunti, M. Laveder, Y.F. Li, H.W. Long, Phys.Rev. **D88**, 073008 (2013), arXiv:1308.5288.

[36] J. Kopp, P. A. N. Machado, M. Maltoni, T. Schwetz, JHEP **1305**, 050 (2013), arXiv:1303.3011.

[37] S. Davidson , E. Nardi, Y. Nir, Phys. Rept. **466**, 105 (2008), arXiv:0802.2962.

Dark Matter Particles in the Galactic Halo

R. Bernabei[a,b,1], P. Belli[a,b], A. Di Marco[a,b], V. Merlo[a,b], F. Montecchia[b,2], F. Cappella[c,d], A. d'Angelo[c,d], A. Incicchitti[c,d], V. Caracciolo[e], R. Cerulli[e], C.J. Dai[f], H.L. He[f], H.H. Kuang[f], X.H. Ma[f], X.D. Sheng[f], R.G. Wang[f], Z.P. Ye[f,g]

[a] *Dipartimento di Fisica, Università di Roma "Tor Vergata", I-00133 Rome, Italy*

[b] *INFN – Tor Vergata, I-00133 Rome, Italy*

[c] *Dipartimento di Fisica, Università di Roma "La Sapienza", I-00185 Rome, Italy*

[d] *INFN – Roma, I-00185 Rome, Italy*

[e] *INFN, Laboratori Nazionali del Gran Sasso, I-67010 Assergi AQ, Italy*

[f] *Key Laboratory of Particle Astrophysics, IHEP, 100049 Beijing, P. R. China*

[g] *University of Jing Gangshan, Ji'an, Jiangxi, China*

Abstract

Many experimental observations and theoretical arguments have pointed out that a large fraction of the Universe is composed by Dark Matter (DM) particles. Many possibilities are open on the nature and interaction types of such relic particles. Here main results, obtained by exploiting the model independent DM annual modulation signature for the presence of DM particles in the galactic halo by DAMA, are summarized. Some other recent efforts and results on DM investigation are mentioned as well.

[1] rita.bernabei@roma2.infn.it

[2] also Dip. di Ingegneria Civile e Ingegneria Informatica, Università di Roma "Tor Vergata", I-00133 Rome, Italy

1 Introduction

Experimental observations and theoretical arguments pointed out that most of the matter in the Universe has a non baryonic nature and is in form of DM particles. Many candidates, having different nature and with different and various interaction types, have been proposed as DM particles in theories beyond the Standard Model of particle physics. Depending on the DM candidate, the interaction processes can be various. Moreover, many experimental and theoretical uncertainties exist and must be properly considered in a suitable interpretation and comparison among experiments aiming the direct detection of DM particles.

Large efforts are dedicated all over the world to investigate the DM with different strategies and techniques that can give complementary information. In particular, the DM indirect search – that is the study of possible products either of decay or of annihilation in the galactic halo or in celestial body of some DM candidate – is performed as by-product of experiments located underground, under-water, under-ice, or in space. The interpretation of such a study is strongly dependent on the chosen assumptions for the modeling of the background and is restricted to some DM candidates with peculiar features and within some particular scenario. On the other hand, experiments at accelerators may prove – when they can state a solid model independent result – the existence of some possible DM candidates, but they could never credit by themselves that a certain particle is a/the only solution for DM particle(s). Moreover, DM candidate particles and scenarios (even e.g. in the case of the neutralino candidate) exist which cannot be investigated at accelerators.

In order to pursue a widely sensitive direct detection of DM particles in the galactic halo, a model independent approach, a ultra-low-background suitable target material, a very large exposure and the full control of running conditions are strictly necessary.

2 DM model independent signature

To obtain a reliable signature for the presence of DM particles in the galactic halo, it is necessary to exploit a suitable model independent signature: with the present technology, one feasible and able to test a large range of cross sections and of DM particle halo densities, is the so-called DM annual modulation signature [1]. The annual modulation of the signal rate originates from the Earth revolution around the Sun. In fact, as a consequence of its annual revolution around the Sun, which is moving in the Galaxy traveling with respect to the Local Standard of Rest towards the star Vega

near the constellation of Hercules, the Earth should be crossed by a larger flux of DM particles around ~2 June (when the Earth orbital velocity is summed to the one of the solar system with respect to the Galaxy) and by a smaller one around ~2 December (when the two velocities are subtracted). Thus, this signature has a different origin and peculiarities than effects correlated with seasons (consider the expected value of the phase as well as the other requirements listed below). This DM annual modulation signature is very distinctive since the effect induced by DM particles must simultaneously satisfy all the following requirements: (1) the rate must contain a component modulated according to a cosine function; (2) with one year period; (3) with a phase that peaks roughly around ~ 2nd June; (4) this modulation must be present only in a well-defined low energy range, where DM particles can induce signals; (5) it must be present only in those events where just a single detector, among all the available ones in the used set-up, actually "fires" (*single-hit* events), since the probability that DM particles experience multiple interactions is negligible; (6) the modulation amplitude in the region of maximal sensitivity has to be $\lesssim 7\%$ in case of usually adopted halo distributions, but it may be significantly larger in case of some particular scenarios such as e.g. those in Ref. [2, 3]. This signature is model independent and might be mimicked only by systematic effects or side reactions able to simultaneously satisfy all the requirements given above; no one is available. At present status of technology it is the only DM model independent signature available in direct DM investigation that can be effectively exploited.

3 DAMA DM annual modulation results with highly radiopure NaI(Tl)

The DM annual modulation signature has been exploited with large exposure – using highly radiopure NaI(Tl) as target material – by the former DAMA/NaI ($\simeq$ 100 kg sensitive mass) experiment [4, 5, 6, 7, 8, 9, 10, 11, 12, 13], and by the currently running DAMA/LIBRA ($\simeq$ 250 kg sensitive mass) [14, 15, 16, 17, 18, 19, 20, 21, 22, 23, 24, 25, 26, 27, 28, 29, 30], within the DAMA project. The DAMA project is dedicated to the development and use of low background scintillators for underground physics.

In particular, the experimental observable in DAMA experiments is the modulated component of the signal in NaI(Tl) target and not the constant part of it, as done in the other approaches.

The full description of the DAMA/LIBRA set-up and performances during the phase1 and phase2 (presently running) and other related arguments

have been discussed in details in Refs. [14, 15, 16, 17, 19, 20, 26, 21, 30] and references therein. Here we just remind that the sensitive part of this set-up is made of 25 highly radiopure NaI(Tl) crystal scintillators (5-rows by 5-columns matrix) having 9.70 kg mass each one. In each detector two 10 cm long UV light guides (made of Suprasil B quartz) act also as optical windows on the two end faces of the crystal, and are coupled to two low background photomultipliers (PMTs) working in coincidence at single photoelectron level. The low background 9265-B53/FL and 9302-A/FL PMTs, developed by EMI-Electron Tubes with dedicated R&Ds, were used in the phase1; for details see Ref. [14, 8, 10, 30] and references therein. The detectors are housed in a sealed low-radioactive copper box installed in the center of a low-radioactive Cu/Pb/Cd-foils/polyethylene/paraffin shield; moreover, about 1 m concrete (made from the Gran Sasso rock material) almost fully surrounds (mostly outside the barrack) this passive shield, acting as a further neutron moderator. A threefold-levels sealing system prevents the detectors to be in contact with the environmental air of the underground laboratory [14]. The light response of the detectors during phase1 typically ranges from 5.5 to 7.5 photoelectrons/keV, depending on the detector. The hardware threshold of each PMT is at single photoelectron, while a software energy threshold of 2 keV electron equivalent (hereafter keV) is used [14, 8]. Energy calibration with X-rays/γ sources are regularly carried out in the same running condition down to few keV [14]; in particular, double coincidences due to internal X-rays from ^{40}K (which is at ppt levels in the crystals) provide (when summing the data over long periods) a calibration point at 3.2 keV close to the software energy threshold (for details see Ref. [14]). The radiopurity, the procedures and details are discussed in Ref. [14, 15, 16, 17, 21, 30] and references therein.

The data of DAMA/LIBRA–phase1 correspond to 1.04 ton $\times$ yr collected in 7 annual cycles; when including also the data of the DAMA/NaI experiment the total exposure is 1.33 ton $\times$ yr collected in 14 annual cycles. In order to investigate the presence of an annual modulation with proper features in the data, many analyses have been carried out. All these analyses point out the presence of an annual modulation satisfying all the requirements of the signature [15, 16, 17, 21, 30]. In Fig. 1, as example, it is plotted the time behaviour of the experimental residual rate of the *single-hit* scintillation events for DAMA/LIBRA–phase1 in the (2–6) keV energy interval. When fitting the *single-hit* residual rate of DAMA/LIBRA–phase1 together with the DAMA/NaI ones, with the function: $A\cos\omega(t-t_0)$, considering a period $T = \frac{2\pi}{\omega} = 1$ yr and a phase $t_0 = 152.5$ day (June 2^{nd}) as expected by the DM annual modulation signature, the following modulation amplitude is obtained: $A = (0.0110 \pm 0.0012)$ cpd/kg/keV, corresponding

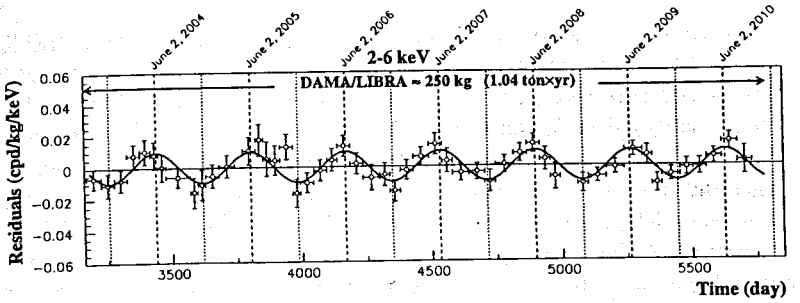

Figure 1: Experimental residual rate of the *single-hit* scintillation events measured by DAMA/LIBRA–phase1 in the (2–6) keV energy interval as a function of the time. The superimposed curve is the cosinusoidal function behaviour $A\cos\omega(t-t_0)$ with a period $T = \frac{2\pi}{\omega} = 1$ yr, a phase $t_0 = 152.5$ day (June 2^{nd}) and modulation amplitude, A, equal to the central values obtained by best fit on the data points of the entire DAMA/LIBRA–phase1. The dashed vertical lines correspond to the maximum expected for the DM signal (June 2^{nd}), while the dotted vertical lines correspond to the minimum.

to 9.2 σ C.L..

When the period, and the phase are kept free in the fitting procedure, the modulation amplitude is (0.0112 ± 0.0012) cpd/kg/keV (9.3 σ C.L.), the period $T = (0.998 \pm 0.002)$ year and the phase $t_0 = (144 \pm 7)$ day, values well in agreement with expectations for a DM annual modulation signal. In particular, the phase is consistent with about June 2^{nd} and is fully consistent with the value independently determined by Maximum Likelihood analysis [17].

For completeness, we recall that a slight energy dependence of the phase could be expected in case of possible contributions of non-thermalized DM components to the galactic halo, such as e.g. the SagDEG stream [12, 31, 32] and the caustics [33]. For more details see Ref. [17].

The modulation amplitudes singularly calculated for each annual cycle of DAMA/NaI and DAMA/LIBRA–phase1 are compatible among them and are normally fluctuating around their best fit values [15, 16, 17, 21, 30].

The DAMA/LIBRA–phase1 *single-hit* residuals of Fig. 1 and those of DAMA/NaI have also been investigated by a Fourier analysis. The data analysis procedure has been described in details in Ref. [21]. A clear peak corresponding to a period of 1 year is evident for the (2–6) keV energy interval; the same analysis in the (6–14) keV energy region shows only aliasing peaks instead. Neither other structure at different frequencies has been observed (see also Ref. [21]).

Absence of any other significant background modulation in the energy spectrum has been verified in energy regions not of interest for DM; e.g. the measured rate integrated above 90 keV, R_{90}, as a function of the time has been analysed [17]. Similar result is obtained in other energy intervals. It is worth noting that the obtained results account of whatever kind of background and, in addition, no background process able to mimic the DM annual modulation signature (that is able to simultaneously satisfy all the peculiarities of the signature and to account for the measured modulation amplitude) is available (see also discussions e.g. in Ref. [14, 15, 16, 17, 20, 21, 25, 34, 35, 36, 37, 38, 39, 40]).

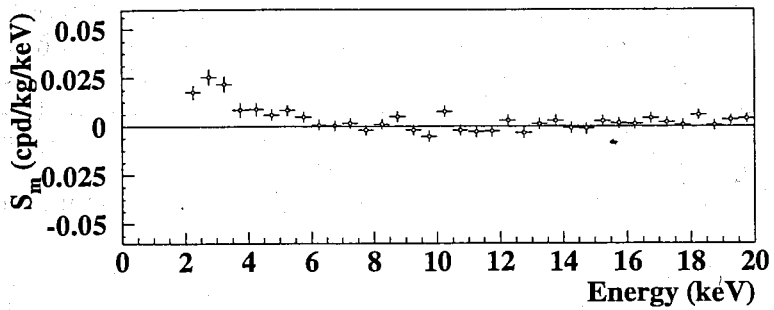

Figure 2: Energy distribution of the S_m variable for the total cumulative exposure 1.33 ton×yr. The energy bin is 0.5 keV. A clear modulation is present in the lowest energy region, while S_m values compatible with zero are present just above. In fact, the S_m values in the (6–20) keV energy interval have random fluctuations around zero with χ^2 equal to 35.8 for 28 degrees of freedom (upper tail probability of 15%).

A further relevant investigation in the DAMA/LIBRA–phase1 data has been performed by applying the same hardware and software procedures, used to acquire and to analyse the *single-hit* residual rate, to the *multiple-hit* one. In fact, since the probability that a DM particle interacts in more than one detector is negligible, a DM signal can be present just in the *single-hit* residual rate. Thus, the comparison of the results of the *single-hit* events with those of the *multiple-hit* ones corresponds practically to compare between them the cases of DM particles beam-on and beam-off. This procedure also allows an additional test of the background behaviour in the same energy interval where the positive effect is observed. In particular, while a clear modulation, satisfying all the peculiarities of the DM annual modulation signature, is present in the *single-hit* events, the fitted modulation amplitude for the *multiple-hit* residual rate is well compatible with zero:

$-(0.0005 \pm 0.0004)$ cpd/kg/keV in the energy region (2–6) keV [17]. Thus, again evidence of annual modulation with the features required by the DM annual modulation signature is present in the *single-hit* residuals (events class to which the DM particle induced events belong), while it is absent in the *multiple-hit* residual rate (event class to which only background events belong). Similar results were also obtained for the last two annual cycles of the DAMA/NaI experiment [11]. Since the same identical hardware and the same identical software procedures have been used to analyse the two classes of events, the obtained result offers an additional strong support for the presence of a DM particle component in the galactic halo.

The annual modulation present at low energy can also be pointed out by depicting – as a function of the energy – the modulation amplitude, $S_{m,k}$, obtained by maximum likelihood method considering T =1 yr and $t_0 = 152.5$ day. For such purpose the likelihood function of the *single-hit* experimental data in the $k-$th energy bin is defined as: $\mathbf{L_k} = \mathbf{\Pi}_{ij} e^{-\mu_{ijk}} \frac{\mu_{ijk}^{N_{ijk}}}{N_{ijk}!}$, where N_{ijk} is the number of events collected in the i-th time interval (hereafter 1 day), by the j-th detector and in the k-th energy bin. N_{ijk} follows a Poisson's distribution with expectation value $\mu_{ijk} = [b_{jk} + S_{ik}] M_j \Delta t_i \Delta E \epsilon_{jk}$. The b_{jk} are the background contributions, M_j is the mass of the $j-$th detector, Δt_i is the detector running time during the i-th time interval, ΔE is the chosen energy bin, ϵ_{jk} is the overall efficiency. Moreover, the signal can be written as $S_{ik} = S_{0,k} + S_{m,k} \cdot \cos\omega(t_i - t_0)$, where $S_{0,k}$ is the constant part of the signal and $S_{m,k}$ is the modulation amplitude. The usual procedure is to minimize the function $y_k = -2ln(\mathbf{L_k}) - const$ for each energy bin; the free parameters of the fit are the $(b_{jk} + S_{0,k})$ contributions and the $S_{m,k}$ parameter. Hereafter, the index k is omitted for simplicity.

In Fig. 2 the obtained S_m are shown in each considered energy bin (there $\Delta E = 0.5$ keV) when the data of DAMA/NaI and DAMA/LIBRA–phase1 are considered. It can be inferred that positive signal is present in the (2–6) keV energy interval, while S_m values compatible with zero are present just above. In fact, the S_m values in the (6–20) keV energy interval have random fluctuations around zero with χ^2 equal to 35.8 for 28 degrees of freedom (upper tail probability of 15%). All this confirms the previous analyses.

As described in Ref. [15, 16, 17, 21, 30], the observed annual modulation effect is well distributed in all the 25 detectors at 95% C.L.

Among further additional tests, the analysis of the modulation amplitudes as a function of the energy separately for the nine inner detectors and the remaining external ones has been carried out for the entire DAMA/LIBRA–phase1. The obtained values are fully in agreement; in

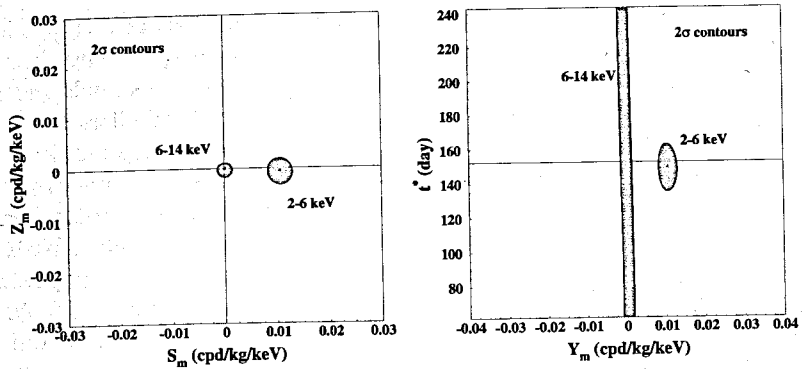

Figure 3: 2σ contours in the plane (S_m, Z_m) (*left*) and in the plane (Y_m, t^*) (*right*) for the (2–6) keV and (6–14) keV energy intervals. The contours have been obtained by the maximum likelihood method, considering the cumulative exposure of DAMA/NaI and DAMA/LIBRA–phase1. A modulation amplitude is present in the lower energy intervals and the phase agrees with that expected for DM induced signals. See text.

fact, the hypothesis that the two sets of modulation amplitudes as a function of the energy belong to same distribution has been verified by χ^2 test, obtaining: $\chi^2/d.o.f. = 3.9/4$ and $8.9/8$ for the energy intervals (2–4) and (2–6) keV, respectively ($\Delta E = 0.5$ keV). This shows that the effect is also well shared between inner and outer detectors.

Let us, finally, release the assumption of a phase $t_0 = 152.5$ day in the procedure to evaluate the modulation amplitudes. In this case the signal can be written as:

$$\begin{aligned} S_{ik} &= S_{0,k} + S_{m,k}\cos\omega(t_i - t_0) + Z_{m,k}\sin\omega(t_i - t_0) \\ &= S_{0,k} + Y_{m,k}\cos\omega(t_i - t^*). \end{aligned} \qquad (1)$$

For signals induced by DM particles one should expect: i) $Z_{m,k} \sim 0$ (because of the orthogonality between the cosine and the sine functions); ii) $S_{m,k} \simeq Y_{m,k}$; iii) $t^* \simeq t_0 = 152.5$ day. In fact, these conditions hold for most of the dark halo models; however, as mentioned above, slight differences can be expected in case of possible contributions from non-thermalized DM components, such as e.g. the SagDEG stream [12, 31, 32] and the caustics [33].

Considering cumulatively the data of DAMA/NaI and DAMA/LIBRA–phase1 the obtained 2σ contours in the plane (S_m, Z_m) for the (2–6) keV and (6–14) keV energy intervals are shown in Fig. 3–*left* while in Fig. 3–*right* the obtained 2σ contours in the plane (Y_m, t^*) are depicted.

Finally, setting S_m in eq. (1) to zero, the Z_m values as function of the energy have also been determined by using the same procedure. The values of Z_m are well compatible with zero, as expected [15, 16, 17].

No modulation has been found in any possible source of systematics or side reactions; thus, cautious upper limits on possible contributions to the DAMA/LIBRA–phase1 measured modulation amplitude have been obtained (see Refs. [15, 16, 17, 9, 10, 11, 20, 26]). It is worth noting that they do not quantitatively account for the measured modulation amplitudes, and also are not able to simultaneously satisfy all the many requirements of the signature. Similar analyses have also been performed for the DAMA/NaI data [10, 11].

Table 1: Summary of the contributions to the total neutron flux at LNGS; the value, $\Phi_{0,k}^{(n)}$, the relative modulation amplitude, η_k, and the phase, t_k, of each component is reported. It is also reported the counting rate, $R_{0,k}$, in DAMA/LIBRA for *single-hit* events, in the $(2-6)$ keV energy region induced by neutrons, muons and solar neutrinos, detailed for each component. The modulation amplitudes, A_k, are reported as well, while the last column shows the relative contribution to the annual modulation amplitude observed by DAMA/LIBRA, $S_m^{exp} \simeq 0.0112$ cpd/kg/keV [17]. For details see Ref. [26] and references therein.

	Source	$\Phi_{0,k}^{(n)}$ (neutrons cm^{-2} s^{-1})	η_k	t_k	$R_{0,k}$ (cpd/kg/keV)	$A_k = R_{0,k}\eta_k$ (cpd/kg/keV)	A_k/S_m^{exp}
SLOW neutrons	thermal n ($10^{-2} - 10^{-1}$ eV)	1.08×10^{-6}	$\simeq 0$ however $\ll 0.1$	-	$< 8 \times 10^{-6}$	$\ll 8 \times 10^{-7}$	$\ll 7 \times 10^{-5}$
	epithermal n (eV-keV)	2×10^{-6}	$\simeq 0$ however $\ll 0.1$	-	$< 3 \times 10^{-3}$	$\ll 3 \times 10^{-4}$	$\ll 0.03$
FAST neutrons	fission, $(\alpha, n) \to$ n (1-10 MeV)	$\simeq 0.9 \times 10^{-7}$	$\simeq 0$ however $\ll 0.1$	-	$< 6 \times 10^{-4}$	$\ll 6 \times 10^{-5}$	$\ll 5 \times 10^{-3}$
	$\mu \to$ n from rock (> 10 MeV)	$\simeq 3 \times 10^{-9}$	0.0129	end of June	$\ll 7 \times 10^{-4}$	$\ll 9 \times 10^{-6}$	$\ll 8 \times 10^{-4}$
	$\mu \to$ n from Pb shield (> 10 MeV)	$\simeq 6 \times 10^{-9}$	0.0129	end of June	$\ll 1.4 \times 10^{-3}$	$\ll 2 \times 10^{-5}$	$\ll 1.6 \times 10^{-3}$
	$\nu \to$ n (few MeV)	$\simeq 3 \times 10^{-10}$	0.03342*	Jan. 4th*	$\ll 7 \times 10^{-5}$	$\ll 2 \times 10^{-6}$	$\ll 2 \times 10^{-4}$
	direct μ	$\Phi_0^{(\mu)} \simeq 20\ \mu$ m^{-2}d^{-1}	0.0129	end of June	$\simeq 10^{-7}$	$\simeq 10^{-9}$	$\simeq 10^{-7}$
	direct ν	$\Phi_0^{(\nu)} \simeq 6 \times 10^{10}\ \nu$ cm^{-2}s^{-1}	0.03342*	Jan. 4th*	$\simeq 10^{-5}$	3×10^{-7}	3×10^{-5}

* The annual modulation of solar neutrino is due to the different Sun-Earth distance along the year; so the relative modulation amplitude is twice the eccentricity of the Earth orbit and the phase is given by the perihelion.

Sometimes naive statements were put forward as the fact that in nature several phenomena may show some kind of periodicity. It is worth noting that the point is whether they might mimic the annual modulation signature in DAMA/NaI and in DAMA/LIBRA, i.e. whether they might be not

only quantitatively able to account for the observed modulation amplitude but also able to contemporaneously satisfy all the requirements of the DM annual modulation signature. The same is for side reactions too. This has already been deeply investigated and discussed in DAMA literature.

In particular, in Refs. [20, 26] a quantitative evaluation why the neutrons, the muons and the solar neutrinos cannot give any significant contribution to the DAMA annual modulation results and cannot mimic this signature is outlined. Table 1 summarizes the safety upper limits on the contributions to the observed modulation amplitude due to the total neutron flux at LNGS, either from (α, n) reactions, from fissions and from muons' and solar-neutrinos' interactions in the rocks and in the lead around the experimental set-up; the direct contributions of muons and solar neutrinos are reported there too.

No systematic effects or side reactions able to account for the whole observed modulation amplitude and to simultaneously satisfy all the requirements of the exploited DM signature have been found. A detailed discussion about all the related arguments can be found in Refs. [14, 15, 16, 17, 20, 21, 25, 9, 10, 11, 26, 30].

4 Implications and comparisons

The long-standing annual-modulation evidence measured in DAMA experiments is model-independent, i.e. without any a-priori assumption of theoretical interpretations of the identity of DM and specifics of its interactions. It can be related to a variety of interaction mechanisms of DM particles with the detector materials and is compatible with a wide set of scenarios regarding the nature of the DM candidate and related astrophysical, nuclear and particle physics. For example, some of the scenarios available in literature and the different parameters are discussed in Refs. [10, 11, 7, 12, 4, 13, 6, 5, 15, 21, 30] and references therein, and recently e.g. in Refs. [41, 28] . Further large literature is available on the topics (see for example in Ref. [21]) and many possibilities are open.

It is worth noting that no other experiment exists, whose result can be – at least in principle – directly compared in a model-independent way with those by DAMA/NaI and DAMA/LIBRA. Some activities claim model-dependent exclusion under many largely arbitrary assumptions (see for example discussions in Ref. [10, 15, 11, 42, 43, 44]). Moreover, often some critical points exist in their experimental aspects, as mentioned above, and the existing experimental and theoretical uncertainties are generally not considered in their presented single model dependent result; moreover, implications of the DAMA results are often presented in incorrect/partial/unupdated way. Both the accounting of the existing uncertainties and the existence of alternative scenarios (see literature) allow one to note that model dependent results by indirect and direct experiments actually are not in conflict with the DAMA model independent result.

The model independent annual modulation effect observed by the DAMA experiments has been investigated in terms of many DM candidates. Here we just recall the recent case of a mirror-type dark matter candidates in some scenarios [28, 29].

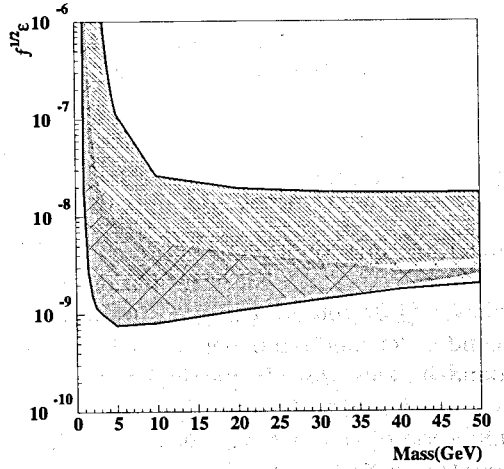

Figure 4: Allowed regions for the $\sqrt{f}\epsilon$ parameter as function of mirror hydrogen mass, obtained by marginalizing all the models for each considered scenario. The allowed intervals identify the $\sqrt{f}\epsilon$ values corresponding to C.L. larger than 5σ from the *null hypothesis*, that is $\sqrt{f}\epsilon = 0$. The allowed regions corresponding to five different scenarios are depicted in different hatching; the black line is the overall boundary; for details see Ref. [28].

In particular, in the framework of asymmetric mirror matter, the DM originates from hidden (or shadow) gauge sectors which have particles and interaction content similar to that of ordinary particles. It is assumed that the mirror parity is spontaneously broken and the electroweak symmetry breaking scale v' in the mirror sector is much larger than that in the Standard Model, $v = 174$ GeV. In this case, the mirror world becomes a heavier and deformed copy of our world, with mirror particle masses scaled in different ways with respect to the masses of the ordinary particles. Then, in this scenario dark matter would exist in the form of mirror hydrogen composed of mirror proton and electron, with mass of about 5 GeV which is a rather

interesting mass range for dark matter particles.

The data analysis in the Mirror DM model framework allows the determination of the $\sqrt{f}\epsilon$ parameter (where f is the fraction of DM in the Galaxy in form of mirror atoms and ϵ is the coupling constant). In the analysis several uncertainties on the astrophysical, particle physics and nuclear physics models have been taken into account in the calculation. The obtained values of the $\sqrt{f}\epsilon$ parameter in the case of mirror hydrogen atom ranges between 7.7×10^{-10} to 1.1×10^{-7}; they are well compatible with cosmological bounds [28].

In addition, releasing the assumption $M_{A'} \simeq 5m_p$, the allowed regions for the $\sqrt{f}\epsilon$ parameter as function of $M_{A'}$, mirror hydrogen mass, obtained by marginalizing all the models for each considered scenario, are shown in Fig. 4.

5 Diurnal modulation

The results obtained by investigating the presence of possible diurnal variation in the low-energy *single-hit* scintillation events collected by DAMA/LIBRA–phase1 (1.04 ton × year exposure) have been analysed in terms of a DM second order model-independent effect due to the Earth diurnal rotation around its axis [25]. In particular, the data were analysed using the sidereal time referred to Greenwich, often called GMST.

This daily modulation of the rate on the sidereal time, expected when taking into account the contribution of the Earth rotation velocity, has several requirements as the DM annual modulation effect does. The interest in this signature is that the ratio R_{dy} of this diurnal modulation amplitude over the annual modulation amplitude is a model independent constant at given latitude; considering the LNGS latitude one has $R_{dy} = \frac{S_d}{S_m} \simeq 0.016$.

Taking into account R_{dy} and the DM annual modulation effect pointed out by DAMA/LIBRA–phase1 for *single-hit* events in the low energy region, it is possible to derive the diurnal modulation amplitude expected for the same data. In particular, when considering the (2–6) keV energy interval, the observed annual modulation amplitude in DAMA/LIBRA–phase1 is: (0.0097 ± 0.0013) cpd/kg/keV [17] and the expected value of the diurnal modulation amplitude is $\simeq 1.5\times 10^{-4}$ cpd/kg/keV.

Fig. 5 shows the time and energy behaviour of the experimental residual rates of *single-hit* events both as a function of solar (*left*) and of sidereal (*right*) time, in the (2–6) keV interval. The used time bin is 1 (either solar or sidereal) hour.

The null hypothesis (absence of residual rate diurnal variation) has been tested by a χ^2 test and run test [25]. Thus, the presence of any significant

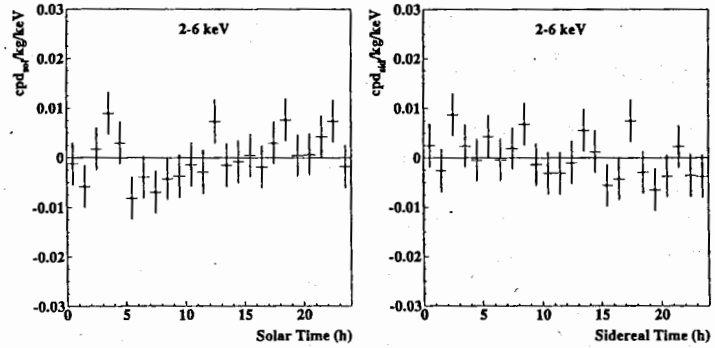

Figure 5: Experimental model-independent diurnal residual rate of the *single-hit* scintillation events, measured by DAMA/LIBRA–phase1 in the (2–6) keV energy interval as a function of the hour of the solar (*left*) and sidereal (*right*) day. The experimental points present the errors as vertical bars and the associated time bin width (1 hour) as horizontal bars. The cumulative exposure is 1.04 ton × yr. See Ref. [25] for details.

diurnal variation and of time structures can be excluded at the reached level of sensitivity (see Fig. 5).

In order to compare the experimental data with the DM diurnal effect due to the Earth rotation around its axis, the sidereal diurnal modulation amplitude of the (2–6) keV energy interval is taken into account: $A_d^{exp} = -(1.0 \pm 1.3) \times 10^{-3}$ cpd/kg/keV. Following the Feldman-Cousins procedure an upper limit can be obtained for the measured diurnal modulation amplitude: $A_d^{exp} < 1.2 \times 10^{-3}$ cpd/kg/keV (90% C.L.); thus, the effect of DM diurnal modulation (expected amplitude $\simeq 1.5\times 10^{-4}$ cpd/kg/keV) is out the present sensitivity [25].

In conclusion, at that level of sensitivity of DAMA/LIBRA–phase1 the presence of a significant diurnal variation and of diurnal time structures in the data can be excluded for both the cases of solar and sidereal time. In particular, the sidereal diurnal modulation amplitude – expected on the basis of the DAMA DM annual modulation results and because of the Earth diurnal motion – cannot be investigated at the present sensitivity; DAMA/LIBRA–phase2, presently running, with a lower software energy threshold [19] can also offer the possibility to increase sensitivity to such an effect.

6 Daily effect on the sidereal time due to the shadow of the Earth

The results obtained in the investigation of possible diurnal effects for low-energy *single-hit* scintillation events of DAMA/LIBRA–phase1 have been analysed in terms of Earth Shadow Effect, a model-dependent effect that is expected for DM candidates inducing only nuclear recoils and having high cross-section (σ_n) with ordinary matter [27].

In fact a diurnal variation of the low energy rate could be expected for these specific candidates, because of the different thickness of the shield due to the Earth during the sidereal day, eclipsing the wind of DM particles. The induced effect should be a daily variation of their velocity distribution, and therefore of the signal rate measured deep underground. However, this effect is very small and would be appreciable only in case of high cross-section spin independent coupled candidates. Such candidates must constitute a little fraction (ξ) of the Galactic dark halo in order to fulfil the positive DAMA result on annual modulation. By the fact, this analysis decouples ξ from σ_n. Considering the measured DM annual modulation effect and the absence – at the present level of sensitivity – of diurnal effects, the analysis selects allowed regions in the three-dimensional space: ξ, σ_n and DM particle mass in some model scenarios; for details see Ref. [27].

7 $ZnWO_4$ anisotropic scintillator for Dark Matter investigation with the directionality technique

An independent evidence can be obtained by pursuing a different approach, but effective only for those DM candidate particles able to induce just nuclear recoils: the directionality [45]. This strategy is based on the correlation between the arrival direction of the DM particles (and thus of the induced nuclear recoils) and the Earth motion in the Galactic rest frame. Because of the rotation of the Milky Way, the Galactic disc passes through the halo of DM and the Earth is crossed by a wind of DM particles apparently flowing along a direction opposite to that of solar motion. Since the Earth rotates around its axis, the average direction of DM particles with respect to an observer fixed on the Earth changes during the sidereal day. Thus, the directions of the induced nuclear recoils are expected to be strongly correlated with the impinging direction of the considered DM candidates while the background events are not.

In principle, an experiment able to measure the nuclear track might be suitable to investigate the directionality. One possibility is to use low pressure gas detector (such as Time Projection Chambers, TPC) where the range of recoiling nuclei is of the order of mm. However, a realistic experiment with low pressure TPC can be limited e.g. by the necessity of an extreme operational stability, of large detector size and of a great spatial resolution in order to reach a significant sensitivity. The limitations affecting experiments aiming to measure recoil tracks, can be overcome by using the anisotropic scintillation detectors [46, 47]. In this case there is no necessity of a track detection and recognition (in solid detectors the range of recoiling nuclei is typically of order of μm). In these detectors the quenching for heavy particles and the scintillation pulse shape depend on the incoming direction of the heavy particles relatively to the crystal axes and the information on the presence of DM induced recoils is given by a peculiar variation of the measured counting rate during the sidereal day [48].

7.1 The main features of the $ZnWO_4$ anisotropic scintillator

Recently, measurements and R&D works have shown that the $ZnWO_4$ scintillators can offer suitable features for a DM experiment based on the directionality. In this crystal scintillator the light output for heavy particles (p, α, nuclear recoils) depends on the direction of such particles with respect to the crystal axes while the response to γ/β radiation is isotropic; the scintillation decay time also shows the same property. In addition to the anisotropy, the recently developed $ZnWO_4$ scintillators have very good level of radiopurity [49], and can work at energy threshold of few keV [50]. The $ZnWO_4$ offers also a high atomic weight and the possibility to realize crystals with masses of some kg [51]. Moreover, three target nuclei with very different masses are present in this detector (Zn, W and O), giving sensitivity to both small and large mass for the considered DM candidates.

Recently, radiopurity and double beta decay processes of zinc and tungsten have been further studied at LNGS using new developed $ZnWO_4$ detectors with masses $0.1 - 0.7$ kg [49, 50, 52, 53]. The growth of the crystals, the scintillation properties, the pulse shape discrimination capability, the anisotropic properties, the residual radioactive contamination and the possible applications have been deeply studied [49, 54, 55, 51, 52, 53, 56, 57]. The obtained results are very promising and an R&D to produce $ZnWO_4$ crystals having higher radiopurity is ongoing. In particular, an R&D to improve $ZnWO_4$ crystals radiopurity by re-crystallization (recently demon-

strated for $CdWO_4$ crystal [56]) is in progress.

In the measured $ZnWO_4$ scintillators the radioactive contamination is: < 0.002 mBq/kg for ^{228}Th and ^{226}Ra (~ 0.5 ppt for ^{232}Th and ~ 0.2 ppt for ^{238}U, assuming the secular equilibrium of the ^{232}Th and ^{238}U chains), < 0.02 mBq/kg for ^{40}K; the total α activity is 0.18 mBq/kg [49].

As previously mentioned, the study of the directionality with the $ZnWO_4$ detectors is based on the anisotropic properties of these scintillators. Fig. 6 shows the dependence of the α/β light ratio (quenching factor) on energy and direction of the α beam relatively to the crystal planes in a $ZnWO_4$ crystal [57].

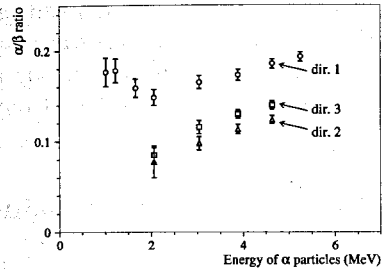

Figure 6: Dependence of the α/β ratio on the energy of α particles measured with $ZnWO_4$ scintillator. The crystal was irradiated in the directions perpendicular to (010), (001) and (100) crystal planes (directions 1, 2 and 3, respectively). The anisotropic behaviour of the crystal is evident [57].

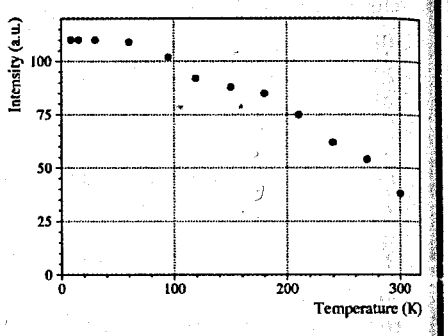

Figure 7: Dependence of the light output of the $ZnWO_4$ as a function of the temperature, for excitation with ^{241}Am α particles [55].

As shown in Fig. 6, the quenching factor for α particles measured along direction 1 is about 1.5 times larger than that measured along direction 2, and about 1.4 times larger than that measured along direction 3. On the contrary, the anisotropy of the light response of the $ZnWO_4$ scintillator disappears in case of electron excitation. Moreover for $ZnWO_4$, as reported in Ref. [57], also the shape of the scintillation pulse depends on the type of irradiation; this feature allows one to discriminate $\gamma(\beta)$ events from those induced by α particles. This pulse shape discrimination capability can be of interest not only for a DM experiment but also for double beta decay searches. Measurements with a neutron beam to study the anisotropy response of the crystal for recoils at keV energy range will be performed in near future [58].

Another feature of this scintillator, important for a DM experiment, is the relatively high light output which is about 13-20% of the Na(Tl) scintillator. It has been observed that the light output largely increase when the crystal scintillator working temperature is decreased [55] (see Fig. 7).

8 Conclusions and Perspectives

The cumulative exposure with ultra low background NaI(Tl) target by the former DAMA/NaI and DAMA/LIBRA–phase1 is 1.33 ton $\times$ yr (orders of magnitude larger than those available in the field) giving a model-independent positive evidence at 9.3 σ C.L. for the presence of DM candidates in the galactic halo with full sensitivity to many kinds of astrophysical, nuclear and particle physics scenarios. Other rare processes have also been searched for by DAMA/LIBRA-phase1 (see for details Refs. [22, 23, 24]) and by DAMA/NaI [60].

After the phase1, an important upgrade has been performed when all the PMTs have been replaced with new ones having higher Quantum Efficiency (QE). In this new configuration a software energy threshold below 2 keV has been reached [19]. DAMA/LIBRA is thus in its phase2, and after optimization periods it is continuously running with higher sensitivity.

The main goals of DAMA/LIBRA–phase2 are: (1) to increase the experimental sensitivity thanks to the lower software energy threshold of the experiment; (2) to improve the corollary investigation on the nature of the DM particle and related astrophysical, nuclear and particle physics arguments; (3) to investigate other signal features; (4) to investigate rare processes other than DM with high sensitivity.

Future improvements to increase the sensitivity of the set-up can be considered by using high QE and ultra-low background PMTs directly coupled to the NaI(Tl) crystals. In this way a further large improvement in the light collection and a further lowering of the software energy threshold would be obtained. Thus, R&D's towards the phase3 of DAMA/LIBRA are in progress.

Finally, the perspectives of a pioneering experiment with anisotropic $ZnWO_4$ detectors to further explore, with the directionality approach, those DM candidate particles inducing just nuclear recoils have been addressed.

9 Acknowledgement

We acknowledge the INR-Kiev group led by Prof. F.A. Danevich for the invaluable contribution to the development – among the others – of the $ZnWO_4$ crystal scintillators and for the fruitful collaboration with the DAMA group.

References

[1] A.K. Drukier, K. Freese, and D.N. Spergel, *Phys. Rev. D* **33**, 3495 (1986); K. Freese, J. A. Frieman and A. Gould, *Phys. Rev. D* **37**, 3388 (1988).

[2] D. Tucker-Smith and N. Weiner, *Phys. Rev. D* **64**, 043502 (2001).

[3] K. Freese et al., *Phys. Rev. D* **71**, 043516 (2005); K. Freese et al., *Phys. Rev. Lett.* **92**, 11301 (2004).

[4] R. Bernabei et al., *Int. J. Mod. Phys. A* **22**, 3155 (2007).

[5] R. Bernabei et al., *Mod. Phys. Lett. A* **23**, 2125 (2008).

[6] R. Bernabei et al., *Phys. Rev. D* **77**, 023506 (2008).

[7] R. Bernabei et al., *Int. J. Mod. Phys. A* **21**, 1445 (2006).

[8] R. Bernabei et al., *Il Nuovo Cim. A* **112**, 545 (1999).

[9] R. Bernabei et al., *Eur. Phys. J. C* **18**, 283 (2000).

[10] R. Bernabei el al., *La Rivista del Nuovo Cimento* **26** n.1, 1-73 (2003).

[11] R. Bernabei et al., *Int. J. Mod. Phys. D* **13**, 2127 (2004).

[12] R. Bernabei et al., *Eur. Phys. J. C* **47**, 263 (2006).

[13] R. Bernabei et al., *Eur. Phys. J. C* **53**, 205 (2008).

[14] R. Bernabei et al., *Nucl. Instr. and Meth. A* **592**, 297 (2008).

[15] R. Bernabei et al., *Eur. Phys. J. C* **56**, 333 (2008).

[16] R. Bernabei et al., *Eur. Phys. J. C* **67**, 39 (2010).

[17] R. Bernabei et al., *Eur. Phys. J. C* **73**, 2648 (2013).

[18] P. Belli et al., *Phys. Rev. D* **84**, 055014 (2011).

[19] R. Bernabei et al., *J. of Instr.* **7**, P03009 (2012).

[20] R. Bernabei et al., *Eur. Phys. J. C* **72**, 2064 (2012).

[21] R. Bernabei et al., *Int. J. of Mod. Phys. A* **28**, 1330022 (2013).

[22] R. Bernabei et al., *Eur. Phys. J. C* **62**, 327 (2009).

[23] R. Bernabei et al., *Eur. Phys. J. C* **72**, 1920 (2012).

[24] R. Bernabei et al., *Eur. Phys. J. A* **49**, 64 (2013).

[25] R. Bernabei et al., *Eur. Phys. J. C* **74**, 2827 (2014).

[26] R. Bernabei et al., *Eur. Phys. J. C* **74**, 3196 (2014).

[27] R. Bernabei et al., *Eur. Phys. J. C* **75**, 239 (2015).

[28] A. Addazi et al, *Eur. Phys. J. C* **75**, 400 (2015).

[29] R. Cerulli et al, *Eur. Phys. J. C* **77**, 83 (2017).

[30] DAMA coll., *Int. J. of Mod. Phys. A* **31**, 1642001–11 (2016).

[31] K. Freese et al., *Phys. Rev. D* **71**, 043516 (2005); *New Astr. Rev.* **49**, 193 (2005); astro-ph/0310334; astro-ph/0309279.

[32] G. Gelmini, P. Gondolo, *Phys. Rev. D* **64**, 023504 (2001).

[33] F.S. Ling, P. Sikivie and S. Wick, *Phys. Rev. D* **70**, 123503 (2004).

[34] R. Bernabei et al., *AIP Conf. Proceed.* **1223**, 50 (2010) [arXiv:0912.0660].

[35] R. Bernabei et al., *J. Phys.: Conf. Series* **203**, 012040 (2010) [arXiv:0912.4200]; *http://taup2009.lngs.infn.it/slides/jul3/nozzoli.pdf*, talk given by F. Nozzoli.

[36] R. Bernabei et al., in the volume *Frontier Objects in Astrophysics and Particle Physics*, ed. S.I.F. (Vulcano, 2010), p. 157 [arXiv:1007.0595].

[37] R. Bernabei et al., *Can. J. Phys.* **89**, 11 (2011).

[38] R. Bernabei et al., *Physics Procedia* **37**, 1095 (2012).

[39] R. Bernabei et al., arXiv:1210.6199.

[40] R. Bernabei et al., arXiv:1211.6346.

[41] S. Scopel et al., arXiv:1512.08577, to appear in the Proceed. of the 14th Marcel Grossmann Meeting.

[42] R. Bernabei et al., in *Liquid Noble gases for Dark Matter searches: a synoptic survey* (Exorma Ed., Roma, ISBN 978-88-95688-12-1, 2009), pp. 1–53; arXiv:0806.0011v2.

[43] R. Bernabei et al., *Int. J. Mod. Phys. A* **30**, 1530053 (2015), 73 pages.

[44] J.I. Collar and D.N. McKinsey, arXiv:1005.0838; arXiv:1005.3723; J.I. Collar, arXiv:1006.2031; arXiv:1010.5187; arXiv:1103.3481; arXiv:1106.0653; arXiv:1106.3559.

[45] D.N. Spergel, *Phys. Rev. D* **37**, 1353 (1988).

[46] P. Belli et al., *In Nuovo Cim. C* **15**, 475 (1992).

[47] R. Bernabei et al., *Eur. Phys. J. C* **28**, 203 (2003).

[48] F. Cappella et al., *Eur. Phys. J. C* **73**, 2276 (2013).

[49] P. Belli et al., *Nucl. Instrum. Meth. A* **626-627**, 31 (2011).

[50] P. Belli et al., *J. Phys. G* **38**, 115107 (2011).

[51] E.N. Galashov et al., *Functional Materials* **16**, 63 (2009).

[52] P. Belli et al., *Phys. Lett. B* **658**, 193 (2008).

[53] P. Belli et al., *Nucl. Phys. A* **826**, 256 (2009).

[54] L.L. Nagornaya et al., *IEEE Trans. Nucl. Sci.* **55**, 1469 (2008).

[55] L.L. Nagornaya et al., *IEEE Trans. Nucl. Sci.* **56**, 994 (2009).

[56] A.S. Barabash et al., *Nucl. Instrum. Meth. A* **833**, 77 (2016).

[57] F.A. Danevic et al., *Nucl. Instrum. Meth. A* **544**, 553 (2005).

[58] C. Taruggi, ROM2F/2016/06.

[59] V.I. Tretyak, *Astropart. Phys.* **33**, 40 (2010).

[60] R. Bernabei et al., *Phys. Lett. B* **408**, 439 (1997); P. Belli et al., *Phys. Lett. B* **460**, 236 (1999); R. Bernabei et al., *Phys. Rev. Lett.* **83**, 4918 (1999); P. Belli et al., *Phys. Rev. C* **60**, 065501 (1999); R. Bernabei et al., *Il Nuovo Cimento A* **112**, 1541 (1999); R. Bernabei et al., *Phys. Lett. B* **515**, 6 (2001); F. Cappella et al., *Eur. Phys. J.-direct C* **14**, 1 (2002); R. Bernabei et al., *Eur. Phys. J. A* **23**, 7 (2005); R. Bernabei et al., *Eur. Phys. J. A* **24**, 51 (2005).

Elementary particles, dark matters, cosmic rays and extended standard model

Jae - Kwang Hwang
JJJ Physics Laboratory, Brentwood, TN 37027, USA

Three generations of leptons and quarks correspond to the lepton charges (LC) in the present work. Then, the leptons have the electric charges (EC) and lepton charges (LC). The quarks have the EC, LC and color charges (CC). Three heavy leptons and three heavy quarks are introduced to make the missing third flavor of EC. Then the three new particles which have the electric charges (EC) are proposed as the bastons (dark matters) with the rest masses of 26.121 eV/c^2, 42.7 GeV/c^2 and 1.9 10^{15} eV/c^2. These new particles are applied to explain the origins of the astrophysical observations like the ultra-high energy cosmic rays and super-nova 1987A anti neutrino data. The 3.5 keV x ray peak observed from the cosmic x-ray background spectra is originated not from the pair annihilations of the dark matters but from the x-ray emission of the Q1 baryon atoms. The new force carrying bosons for the dark matters, leptons and quarks are introduced for the further researches.

1. Introduction

The new physics search beyond standard model has been done by the extended standard models with the new particles. These new particles include the SUSY particles, techniquarks, leptoquarks, Z-prime boson, W-prime boson and heavy quarks (T, B, X and Y), sterile ν, neutralinos, X- and Y- bosons, WIMPS, axions, preons. But there are no experimental evidences for these new particles. The previously known models including the string theory and the supersymmetry model have been developed on the unquantized space. In the present work, the three-dimensional quantized space model is introduced as the new extended standard model for the new elementary particles in Tables 1 and 2. The three dark matters (B1,B2,B3), three heavy leptons (Le, Lμ, Lτ) and three heavy quarks (Q1, Q2,Q3) are introduced. The rest masses of the quarks, leptons and dark matters are calculated by using the simple equations to show the energy scales. These new particles can be indirectly searched for from the astronomical observations like the cosmic rays and cosmic gamma rays. The unsolved questions of the astronomical observations are explained by using the decays and interactions of these new particles in the present work. For example, the ultra-high energy cosmic rays are proposed to be originated from the decays and annihilations of the hadrons including the new heavy quarks (Q1,Q2,Q3). The super-nova 1987A is discussed in the relation with the B1 dark matter. And the observed 18.7 keV, 3.5 keV and 74.9 keV x-ray peaks are emitted from the Q1 baryon atoms.

2. Three-dimensional quantized space model and dark matters

In Table 1, the leptons and quarks have the same properties of the three generations. Three generations separate the leptons and quarks with the same electric charges (EC). Three generations are called as the lepton charges (LC) or lepton flavors in the present work. The difference between the quarks and leptons is that the quarks have the three color flavors or three color charges (CC) of red (r), green (g) and blue (b) but the leptons do not. The quarks with the same charges of EC and LC are separated with three color charges (CC). Because the lepton charges and color charges have the three flavors, the electric charges are expected to have the three flavors. But the electric charges of the leptons and quarks have two flavors. The particles with the same lepton charges are separated with two electric charges of 0 and -1 for the leptons and 2/3 and -1/3 for the quarks. The electric charges are quantized on the basis of the electron electric charge of -1 in
Table 1. Therefore, the heavy quarks with the electric charge of -4/3 and heavy leptons with the electric charge of -2 for the third missing electric charges are added to complete the three flavors of EC, LC and CC in the quarks and leptons in Table 1. The elementary fermions in Table 1 can be explained only by the three-dimensional quantized spaces [1,2]. Each flavor corresponds to each dimensional axis in Table. 1. This work needs the further researches on the new concepts.

Table 1. Elementary fermions in the three-dimensional quantized space model. The bastons (Dark matters) interact gravitationally but not electromagnetically with the electrons, protons and quarks because the bastons do not have the lepton and color charges.

	Bastons (EC)		Leptons(EC,LC)				Quarks(EC,LC,CC)			
	EC		EC				EC			
X1	-2/3	B1	0	ν_e	ν_μ	ν_τ	2/3	u	c	t
X2	-5/3	B2	-1	e	μ	τ	-1/3	d	s	b
X3	-8/3	B3	-2	Le	Lμ	Lτ	-4/3	Q1	Q2	Q3
Total	-5		-3				-1			
	Dark matters		LC				LC			
X4			-2/3	ν_e	e	Le	0	u	d	Q1
X5	Each flavor (charge) corresponds to each dimensional axis.		-5/3	ν_μ	μ	Lμ	-1	c	s	Q2
X6			-8/3	ν_τ	τ	Lτ	-2	t	b	Q3
Total			-5				-3			
							CC			
X7	Baryon: CC = -5 (3 quarks)						-2/3(r)			
X8	Meson: CC = 0 (quark - anti quark)						-5/3(g)			
X9	Paryon: LC = -5 (3 leptons)						-8/3(b)			
Total	Koron: LC = 0 (lepton - anti lepton)						-5			

Only the electric charges have been quantized on the basis of the electron electric charge of -1. First, the new heavy leptons and new heavy quarks have the electric charges of -2 and -4/3, respectively in Table 1. Then the sum of three electric charges is -3 for the leptons and -1 for the quarks. The summed electric charge (-3) of the leptons is decreased by -2 when compared with the summed electric charge (-1) of the quarks. In Table 1, systematically three particles called as the bastons are expected. The sum of three electric charges is -5 for these new particles called as bastons. The electric charges for the bastons are -2/3, -5/3 and -8/3 which make the summed electric charge of -5. The three-dimensional quantized spaces with the summed charges of -5, -3 and -1 are colored in blue, red and green, respectively in Table 1. Let's build up the three-dimensional quantized spaces of the leptons and quarks from the three-dimensional quantized space of the bastons. The three-dimensional quantized space of the bastons is in blue in Table 1. The leptons have the three-dimensional quantized spaces in red and in blue in Table 1. The quarks have the three-dimensional quantized spaces in green, in red and in blue in Table 1. Therefore, the leptons are made by adding the three-dimensional quantized space in red to the bastons. The lepton charges of the leptons are the same as the electric charges of the bastons. And the quarks are made by adding the three-dimensional quantized space in green to the leptons. The lepton charges of the quarks are the same as the electric charges of the leptons and the color charges of the quarks are the same as the lepton charges of the leptons and the electric charges of the bastons in Table 1. Therefore, all quantized charges of the elementary fermions can be assigned as shown in Table 1. Then, the lepton charges are 0, -1 and -2 for the quarks and -2/3, -5/3 and -8/3 for the leptons. And the color charges for quarks are -2/3, -5/3 and -8/3. Therefore, the leptons and quarks should be described as (EC,LC) and (EC,LC,CC), respectively as shown in Table 1. Therefore, the bastons are described as (EC). These new particles have the properties the same as the dark matters have. These new particles interact gravitationally but not electromagnetically with the electrons, protons and quarks because the bastons do not have the lepton and color charges. Then, the bastons are the dark matters. Also, the leptons interact gravitationally but not electromagnetically with the quarks because the leptons do not have the color charges. The leptons can interact electromagnetically with the hadrons like protons because the hadrons of the mesons and baryons have the color charges of 0 and -5, respectively [1,2]. It is called as the hadronization.

The leptons have the electric charges of 0 for the neutrinos and -1 for the electron, muon and tau in terms of the standard model. The weak force carrying bosons have the electric charges of 0 for the Z boson and -1 for the W^- boson in terms of the standard model. These Z and W^- bosons do not care about the lepton charges. These Z and W^- bosons are separated as the Z(0,LC) and W(-1,LC) bosons with the three generations (three lepton charges) in the present extended standard model of Table 2. The rest masses of the Z and W^- bosons in the standard model correspond to the rest masses of the Z(0,0) and W(-1,0) bosons in Table 2,

respectively. The quarks have the electric charges of 2/3 for the u, c and t quarks and -1/3 for the d, s and b quarks in terms of the standard model. The strong force carrying bosons have the electric charges of 0 and double color charges for the massless gluon bosons in terms of the standard model. The electric force carrying boson of the photon has the electric charge of 0. But in the present extended standard model, the new heavy leptons have the electric charge of -2 and the new heavy quarks have the electric charge of -4/3. And the force carrying bosons with the electric charges of 0, -1 and -2 are possible as shown in Table 2. Because the lepton charges and color charges are quantized in Table 1, the corresponding force carrying Z, W and Y bosons for the bastons, leptons and quarks are newly proposed to have the EC, LC and CC charges of 0, -1 and -2, respectively, in Table 2.

Table 2. Complete table of the elementary bosons in the three-dimensional quantized space model.

	Dark matter force		Weak force (EC,LC)			Strong force (EC,LC,CC)			
	EC		EC			EC			
X1	0	Z(0)	0	Z(0,0)	Z(0,−1)	Z(0,−2)	0	Z(0,0)	Z(0,−1)	Z(0,−2)
X2	-1	W(-1)	-1	W(-1,0)	W(-1,-1)	W(-1,-2)	-1	W(-1,0)	W(-1,-1)	W(-1,-2)
X3	-2	Y(-2)	-2	Y(-2,0)	Y(-2,-1)	Y(-2,-2)	-2	Y(-2,0)	Y(-2,-1)	Y(-2,-2)
Total	-3		-3				-3			
			LC				LC			
X4			0	Z(0,0)	W(−1,0)	Y(−2,0)	0	Z(0,0)	W(−1,0)	Y(−2,0)
X5			-1	Z(0,-1)	W(-1,-1)	Y(-1,-1)	-1	Z(0,-1)	W(-1,-1)	Y(-1,-1)
X6			-2	Z(0,-2)	W(-1,-2)	Y(-2,-2)	-2	Z(0,-2)	W(-1,-2)	Y(-2,-2)
Total			-3				-3			
							CC			
X7	Z, W, gluons (SM) → Z(0,LC),W(-1,LC), Z(0,0,CC) (ESM)						0			
X8							-1			
X9	Z/W/Y(EC,LC,0) ⟷ Z/W/Y(EC,LC)						-2			
Total	Z/W/Y(EC,0) ⟷ Z/W/Y(EC)						-3			
	Z/W/Y(-1,0)CC(-2) = Z/W/Y(-1,0,-2)									

By using Tables 1 and 2, all interactions between the elementary particles can be successfully described by using these massive Z, W and Y bosons with the short force range in Fig. 1. In Fig. 1, the Z(0,0,CC) bosons with CC values of 0, -1 and -2 can play the same roles as the gluons do. In fact the massless gluons are replaced with the massive Z/W/Y(EC,LC,CC) bosons in Table 2. Then, the strong force carrying bosons are Z/W/Y(EC,LC,CC) bosons for the quarks, and the weak force carrying bosons are Z/W/Y(EC,LC) bosons for the leptons. And the dark matter force carrying bosons are newly proposed by the Z/W/Y(EC) bosons for the bastons in Table 2. In the present extended standard model, the three charge conservations of EC, LC and CC should be considered. The standard model has

the conservation rules of many quantum numbers such as baryon number, lepton number, B-L symmetry, hyper charge, weak charge, electric charge, color charge, quark flavor quantum number, lepton family number and x-charge. However, the present model has only one conservation rule of EC, LC and CC charges.

Because the neutrinos have the nonzero lepton charges in Table 1, the neutrinos are not the Majorana particles. Therefore, the neutrinoless double beta decay is not possible. The dark matters can interact with the leptons as shown in Fig. 2. The B1-e and B1- μ interactions in Fig. 2 can enhance the numbers of the cosmic ν_e and ν_μ neutrinos when the electrons and muons get through the dense dark matter clouds near the galaxy center. Also, the B1 dark matters can be produced from the LHC accelerator. The observation of the enhanced ν_e neutrinos will be the indirect evidence of the B1 dark matters produced from the LHC accelerator. The LHC and cosmic neutrino experiments will be interesting.

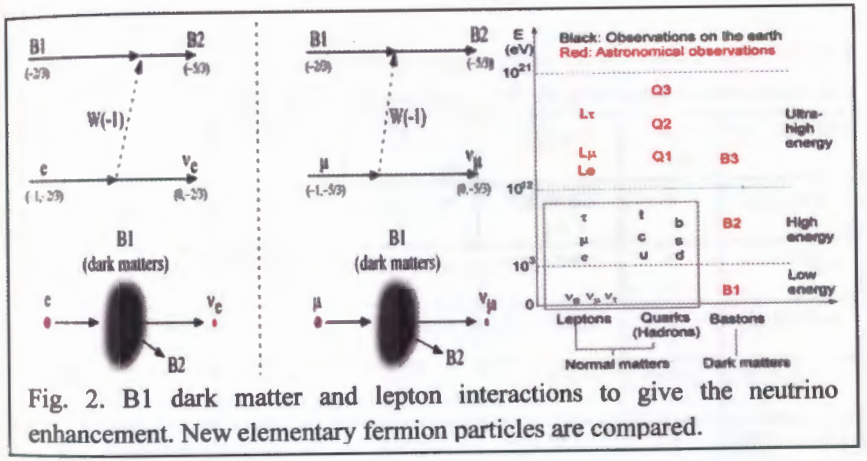

Fig. 2. B1 dark matter and lepton interactions to give the neutrino enhancement. New elementary fermion particles are compared.

3. Origins of high and ultra-high energy cosmic rays

And the rest mass energies of the leptons with the charge configuration of (EC,LC) and bastons (dark matters) with the charge configuration of (EC) are calculated by using the simple equations under the assumptions of E(B2) = 42.7 GeV and $E(\nu_\tau)$ = 0.1 eV.

$F(EC,LC) = -23.24488 + 7.26341|EC| - 1.13858EC^2 + 0.62683|LC| + 0.22755LC^2$

$E = 8.1365\ 10^{38+2F}$ eV for leptons

$E = 17.1501\ 10^{38+2F}$ eV for bastons (dark matters)

Only the EC and LC charges of the leptons and bastons are used for the calculations of the rest masses. The rest masses of the leptons and bastons (dark matters) are compared with the experimental values in Table 3. The rest mass energies of the leptons and dark matters are calculated in order to show the energy scales of these particles by using the simple equations. The parameter values are assigned by fitting the experimental rest mass energies. Then, the unknown neutrino masses and the masses of the heavy leptons (Le, Lμ, Lτ) can be calculated in Table 3. And the masses of the B1 and B3 dark matters can be calculated, too. Also, it is assumed that the rest mass energies of Q1, Q2 and Q3 quarks correspond to the energies of the first knee, second knee and ankle parts of the ultra-high energy cosmic ray spectra, respectively [1,3]. And the color charge effects on the rest mass energies of the quarks are assumed to be negligibly small. Then $E = 10^F$ eV and $F(EC,LC) = 10.34076 - 16.01455|EC| + 15.02553\ EC^2 + 2.14\ |LC| + 0.005\ LC^2$ for Q1,Q2 and Q3 quarks. The obtained rest mass energies are $E(Q1) = 5\ 10^{15}$ eV, $E(Q2) = 7\ 10^{17}$ eV and $E(Q3) = 10^{20}$ eV.

Table 3. Rest masses of the leptons and bastons(dark matters) are calculated and compared with the experimental values [1]. $E=mc^2$.

(EC,LC)	E_{exp} (eV)	E_{calc} (eV)	(EC,LC)	E_{exp} (eV)	E_{calc} (eV)
ν_e(0,-2/3)	?	$2.876\ 10^{-7}$	e(-1,-2/3)	$5.11\ 10^5$	$5.11\ 10^5$
ν_μ(0,-5/3)	?	$5.947\ 10^{-5}$	μ(-1,-5/3)	$1.057\ 10^8$	$1.057\ 10^8$
ν_τ(0,-8/3)	?	$1.000\ 10^{-1}$	τ(-1,-8/3)	$1.777\ 10^9$	$1.777\ 10^9$
Le(-2,-2/3)	$10^{12\text{-}14}$	$2.533\ 10^{13}$	B1(-2/3)	?	26.121
Lμ(-2,-5/3)	?	$5.239\ 10^{15}$	B2(-5/3)	$4.27\ 10^{10}$	$4.27\ 10^{10}$
Lτ(-2,-8/3)	?	$8.811\ 10^{18}$	B3(-8/3)	?	$1.948\ 10^{15}$

In Fig. 3, the e - e^+, and B2- anti B2 plots are shown for the comparison. The 42.7(7) GeV peak was identified in the gamma-ray spectrum from the Fermi Large Area Telescope (LAT) in the directions of 16 massive nearby Galaxy Clusters [4]. The 42.7 GeV peak is proposed as the B2 – anti B2 annihilation peak. Then, the rest mass of the B2 dark matter particle is 42.7(7) GeV/c^2. And the enhanced intensity was observed around 42.7 GeV for the gamma ray spectra of supernova remnant (SNR), W44, as measured with the Fermi-LAT. This might be the B2 – anti B2 annihilation peak [5].

The calculated rest mass energy of the B1 dark matter is 26.121 eV. It will be interesting to look for the 26.121 eV peak at the cosmic x-ray. The calculated rest mass energies of three neutrinos are $2.876\ 10^{-7}$ eV for ν_e, $5.947\ 10^{-5}$ eV for ν_μ and $1.000\ 10^{-1}$ eV for ν_τ in Table 3. It will be interesting to confirm these rest mass energies of three neutrinos in Table 3. The rest masses of the elementary fermions depend on both of EC and LC according to the above mass energy equations. The leptons are separated into three groups. First group is made of the three neutrinos with EC=0 which have the low energy range. Second group is made of the electron, muon and tau lepton with EC=-1 which have the high energy range. The third group is made of the Le, Lμ and Lτ leptons with EC=-2 which have the ultra-high energy range. The B1 dark matter with EC=-2/3 has the rest mass energy between the first group with EC=0 and second group with EC=-1. The B2 dark matter with EC=-5/3 has the rest mass energy between the second group with EC=-1 and third group with EC=-2. The B3 dark matter with EC=-8/3 has the rest mass energy similar to those of the third group with EC=-2.

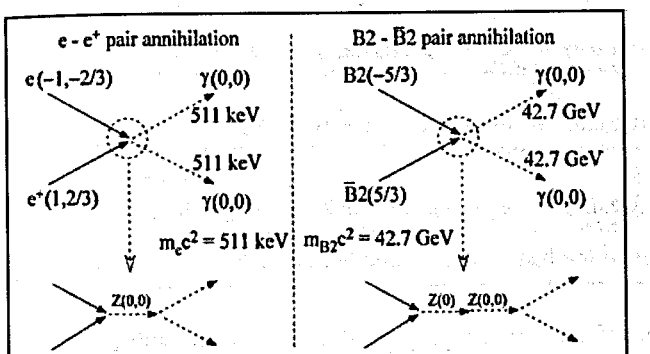

Fig. 3. Particle – anti particle annihilation.

The electron-positron annihilation peaks associated with the outburst of the microquasar V404 Cygni [6] were identified at the energy range of $4\ 10^5 - 2\ 10^6$ eV consistent with the rest mass energy ($5.11\ 10^5$ eV) of the electron. The possible Le – anti Le annihilation peak was identified at the energy range of $10^{12\text{-}14}$ eV in the TeV gamma ray spectrum from RXJ1713.7-3946 with HESS and Fermi-Lat data [7]. The calculated rest mass energy ($2.534\ 10^{13}$ eV) is consistent with the energy of the observed peak in Table 3. The high and ultra-high energy cosmic rays with the energy higher than 10^9 eV are originated from the decay and annihilations of the hadrons including the Q1, Q2 and Q3 quarks with the possible rest masses of $10^{15\text{-}20}$ eV/c^2 and the heavy leptons as shown in Figs. 4 and 5 [8,9].

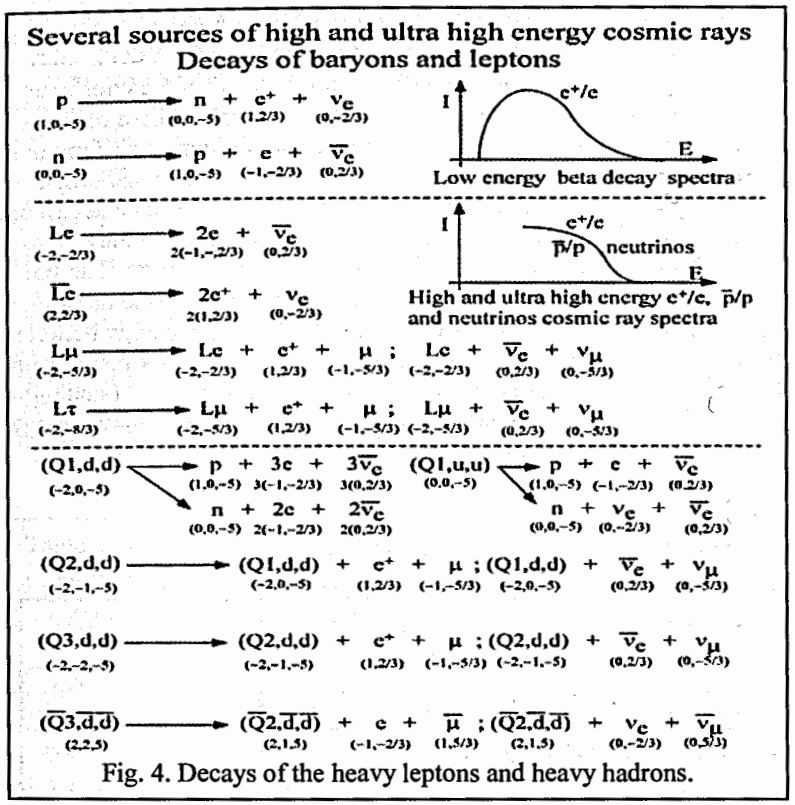

Fig. 4. Decays of the heavy leptons and heavy hadrons.

For the cosmic gamma ray spectra in Fig. 5, the B2 - anti B2 annihilation peak is at 4.27 10^{10} eV and Le – anti Le annihilation peak is at 2.53 10^{13} eV. And the smooth background curve of the cosmic gamma rays are caused by the gamma rays emitted from the Le decay. These shapes of the cosmic gamma ray spectra have been observed and reported in several references [7-10]. For the cosmic electrons, positrons and neutrinos, the cosmic ray spectra have the same origins. These cosmic electron, positron and neutrino spectra are mainly originated from the Le decays [1,11-13]. It can be confirmed from the observed cosmic electron and positron spectra at the TeV energy range. And the cosmic electron, positron and neutrino spectra coming from the Q1 hadron decays are added around 5 10^{15} eV. The positron anomaly, e and e^+ spectra can be explained by the Le and anti Le decays [1,12-14]. The astrophysical neutrino spectra observed at the PeV energy range can be explained by using the Q1 hadron decays [1,11]. It is assumed that the decays of other heavy leptons and heavy hadrons have the relatively small contributions when compared with the Le decays. The ultra-high energy cosmic rays are mostly composed of the protons. The smooth background curve of the

ultra-high energy cosmic ray spectra is caused by the gamma induced protons in Fig. 5 [3]. These protons are accelerated by the inelastic Compton scattering with the gamma rays emitted from the pair annihilations of Q1, Q2 and Q3 hadrons. And the first knee, second knee and ankle parts of the ultra-high energy cosmic ray spectra [1,3] are explained by using the Q1-hadron, Q2-hadron and Q3-hadron decays, respectively. The observed cosmic ray spectra can be found in Ref. [3,15].

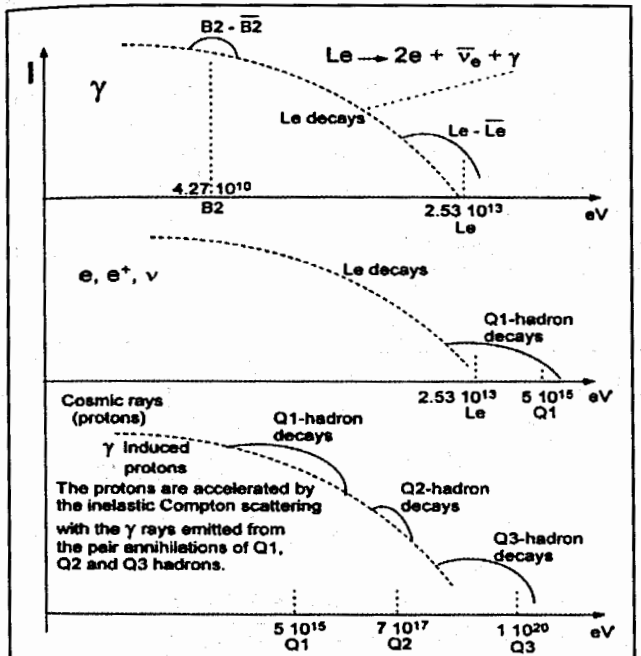

Fig. 5. Origins of the high and ultra-high energy cosmic rays and gamma rays.

4. Possible two Koron discoveries of ee^+ and $\mu^-\mu^+$

In Table 1, quarks and leptons have the similar patterns for the EC and LC charges. So, the, so called, Koron made of the lepton and antilepton is suggested like the Meson made of the quark and antiquark. It will be interesting to look for the Korons. The π^0 meson with u and anti u quarks has the rest mass of 135 MeV/c^2. The rest mass of the u quark is about 2.3 MeV/c^2. So the Koron of π_l^0 with e and e^+ could have the rest mass of the several MeV/c^2 scale. The electron has the rest mass of 0.511 MeV. The X(16.70(35) MeV) peak with the spin of 1^+ was observed from the invariant ee^+ mass distribution from the 18.15 MeV transition in ^{8}Be by Krasznahorkay et al. [16]. This unknown neutral X boson with the rest mass of

16.7 MeV/c^2 is the good candidate of the Koron of π_l^0 with e and e^+. Also, the neutral X boson with the rest mass of 1.6 MeV/c^2 – 20 MeV/c^2 was introduced by Goudeis et al. [17] in order to explain the cosmological lithium abundance problem at the Big Bang Nucleosysthesis (BBN) [16,17]. This X boson will reduce the abundances of ^{7}Be and ^{7}Li through the ^{7}Be(X,α)^{3}He and D(X,p)n [17]. I suggest that this X boson is the same as the X boson observed from the invariant mass distribution from the 18.15 MeV transition in ^{8}Be by Krasznahorkay et al. [16]. Then, the Koron of π_l^0 with e and e^+ can explain the cosmological lithium abundance problem at the Big Bang Nucleosysthesis (BBN) [16,17].

Also, a narrow dimuon, M($\mu^-\mu^+$), mass resonance at 30.4 GeV = 3.04 10^{10} eV was obtained from the archived data of the ALEPH experiment at LEP [18,19]. The data, taken in 1992-95, involve 1.9 million hadronic decays of Z-bosons produced at rest in e--e+ annihilation. This dimuon resonance is considered to be a good candidate of the $\mu^-\mu^+$ Koron. The rest mass of the μ^- lepton is 1.07 10^8 eV/c^2. The dimuon mass resonance decay scheme including the B1 and B2 dark matters is shown in Fig. 6. A Z(0,0) boson decays to a pair of B2 and anti B2 dark matters.

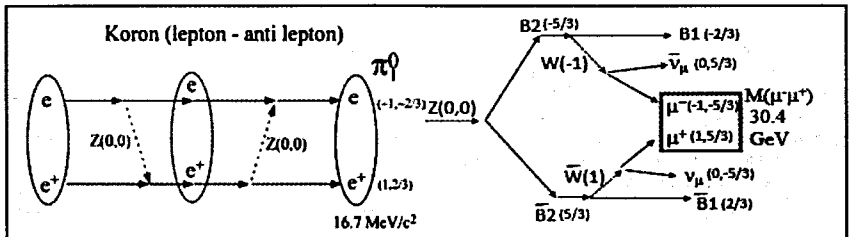

Fig. 6. Two Koron examples of ee^+ and $\mu^-\mu^+$. A neutral Z(0,0) boson decay scheme leads to the dimuon, M($\mu^-\mu^+$), mass resonance.

5. Dark matter and super-nova 1987A

The super-nova 1987A has been seen to have the three rings on the Hubble space telescope pictures. And the evidence of the neutron star is missing in the super-nova 1987A [20-22]. The neutrino masses of 21.4(12) eV/c^2 and 4.0(5) eV/c^2 are extracted from the antineutrino data from the super-nova 1987A [20]. These neutrino masses are too large. So, I tried to solve these two questions by using the B1 dark matter. Then, the new concept of the dark matter core collapse in addition to the normal matter core collapse is introduced in order to build the super-nova structure. The experimental anti-neutrino data are used to draw the conclusions in the present work. The more details on the experimental neutrino measurements can be found from the references [20,21,22].

The super-nova 1987A anti-neutrino data can be drawn as shown in Fig. 7. The neutrino energy of E(ν) is related to the time of t. The equation of $2E^2t = m^2c^4t_0$ is used [20]. The curve A fits other data well except the 6 data. The curve A uses the proposed dark matter mass of B1. It is proposed that the B1 particles come from the SN 1987A to the earth. The B1 and anti *B1* dark matters coming from the SN1987A change the directions by the neutral boson (Z(0)) interactions with p and e in the earth atmosphere. The B1 and anti *B1* dark matters are pair-annihilated within the earth atmosphere and the ν and anti ν pair is created. These neutrinos are observed by using the detectors under the earth surface. The energies, E(ν) of the observed neutrinos are similar to the energies, E(B1) of the B1 dark matters. This supports indirectly that the rest mass energy of the B1 dark matter is 26.12 eV.

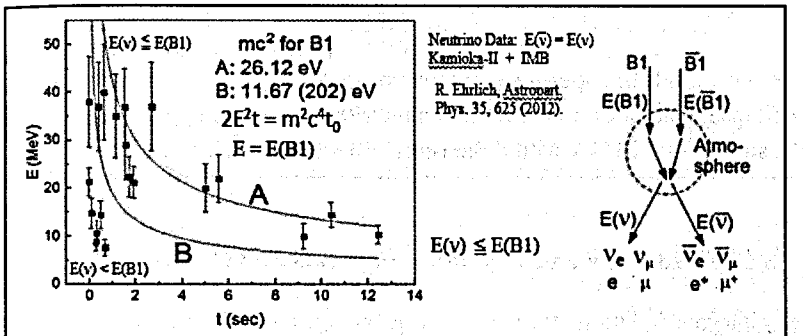

Fig. 7. Neutrino data of the super-nova 1987A. The B1 -anti B1 dark matter pair is annihilated to create the ν – anti ν pair.

In Fig. 8, two kinds of super-nova explosions including the dark matter core collapse in addition to the normal matter collapse are shown. The upper one is for the super-nova 1987A with three rings and without the neutron star. The Dark matter core burst triggers the normal matter core burst without forming the neutron star. The down one is for the normal super-nova with the neutron star. In this case, both of dark matter core and normal matter core are collapsing. Then outside normal matters blast into the space and the inside dark matter and normal matter cores are collapsing to form the neutron star which consists of the neutrons and B1 dark matters.

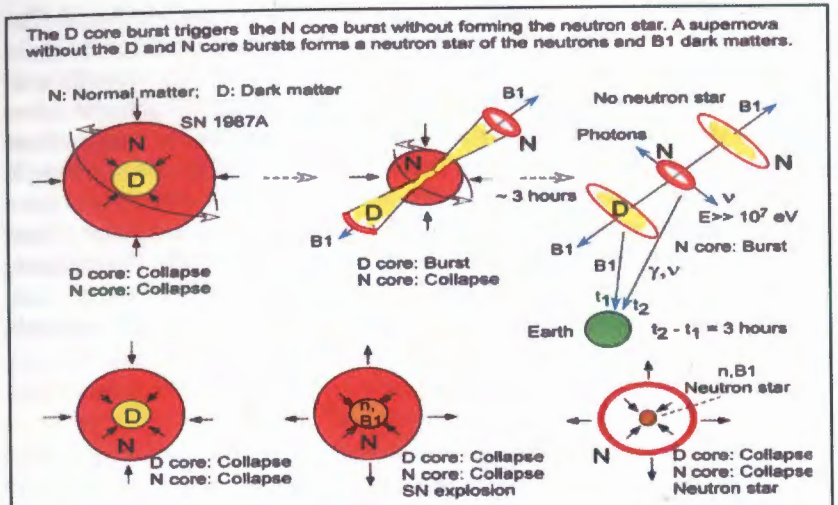

Fig. 8. Two kinds of super-nova explosions including the dark matter core collapse in addition to the normal matter collapse. The upper one is for the super-nova 1987A with three rings and without the neutron star.

6. 3.5 keV 18.7 keV and 74.9 keV x-ray peaks and Q1 baryon atoms

The heavy baryons including the Q1 heavy quark (Q1 baryons) can be made in the active galatic nucleus. This Q1 baryon can have the electric charges (EC) of -1 and -2. For example, the Q(Q1,d,d) and R(Q1,d,u) baryons in Fig. 9 have the charge configurations of (EC,LC) = (-2,0) and(EC,LC) = (-1,0), respectively. Then the protons with the charge configurations of (EC,LC) = (1,0) can rotate around these Q and R baryons to form the Q1 baryon atoms. These Q1 baryon atoms are similar to the hydrogen atoms. The proton energy levels in the Q1 baryon atom are easily calculated in the same way as the electron energy levels in the hydrogen atom are calculated.

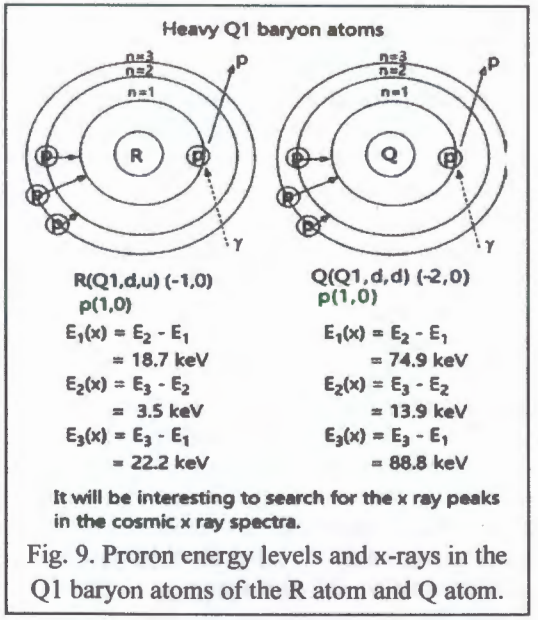

Fig. 9. Proron energy levels and x-rays in the Q1 baryon atoms of the R atom and Q atom.

The calculated x-ray energies are 18.7 keV and 3.5 keV from the R atom and 74.9 keV and 13.9 keV from the Q atom in Fig. 9. The possible 18.7 keV and 74.9 keV x-ray peaks are found at the cosmic x-ray background spectra [1,23,24]. And the 74.9 keV x-ray peak is even seen more clearly on the broadband energy spectrum of the X-ray pulsar 4U 0115+63 from IBIS/ISGRI and JEM-X(INTEGRAL) data in its bright state during the out-burst in May-June 2011 [1,25]. So it is thought that these 18.7 keV and 74.9 keV x-ray peaks are originated from the Q1 baryon atoms in Fig. 9. Also, the 3.5 keV x-ray peak is expected from the Q1 baryon atom of the R atom in Fig. 9. And an emission line at 3.5 keV was detected in the spectrum of the Cosmic X-ray Background using a total of 10 Ms Chandra observations towards the COSMOS Legacy and CDFS survey fields [26]. So it is thought that this observed 3.5 keV x-ray peak is originated from the Q1 baryon atom of the R atom but not from the pair annihilation of the dark matters.

7. Summary

In summary, the three-dimensional quantized space model is introduced as the new extended standard model. Three generations of the leptons and quarks correspond to the lepton charges. Quarks have three charges of EC, LC and CC, and leptons

have two charges of EC and LC. New particles of bastons with only one charge of EC are the dark matters. The dark matter force is introduced with the new Z/W/Y(EC) bosons. The massless gluons are replaced with the new massive Z/W/Y(EC,LC,CC) bosons. And the rest mass energies of the leptons with the charge configuration of (EC.LC) and bastons (dark matters) with the charge configuration of (EC) are calculated by using the simple equations. The standard model has the conservation rules of many quantum numbers such as baryon number, lepton number, B-L symmetry, hyper charge, weak charge, electric charge, color charge, quark flavor quantum number, lepton family number and x-charge. However, the present model has only one conservation rule of EC, LC and CC charges. Several examples of elementary particle decays are shown in Fig. 10. The calculated rest mass energies of three neutrinos are 2.876 10^{-7} eV for ν_e, 5.947 10^{-5} eV for ν_μ and 1.000 10^{-1} eV for ν_τ in Table 3. The assigned neutrino masses need to be confirmed experimentally. And the calculated rest mass energy of the B1 dark matter is 26.121 eV. It will be interesting to look for the 26.121 eV peak at the cosmic x-ray and at LHC. The ultra-high energy cosmic rays and gamma rays are originated from the decay and annihilations of the hadrons including the Q1, Q2 and Q3 quarks with the possible rest masses of $10^{15\text{-}20}$ eV/c^2. The super-nova 1987A structure is explained by using the dark matter core collapse. This supports that the rest mass of the B1 dark matter is 26.121 eV/c^2. The structures of the super-nova with the neutron star and the normal super-nova without the neutron star are introduced and compared by using the new concept of the dark matter core collapse. It is thought that the 18.7 keV, 3.5 keV and 74.9 keV x ray peaks observed from the cosmic x-ray background spectra are originated not from the pair annihilations of the dark matters but from the x-ray emission of the Q1 baryon atoms.

The X(16.70(35) MeV) peak with the spin of 1^+ is proposed as the first Koron of π_l^0 $(e^+e^-)(0,0)$ observed experimentally. The first Koron of π_l^0 (e^+e^-) (0,0) is the good candidate of the neutral boson (X) for the lithium problem. The dimuon resonance is considered to be a good candidate of the $\mu^-\mu^+$ Koron. Dark matters (Bastons) are interacting with the electrons and protons by the gravitational force but not by electromagnetic force. Z and W^- boson in the standard model are Z(0,0) and W(-1,0) in the present work, respectively. Dark matter force, weak force and strong force are explained consistently in Table 2. From the B1–e and B1-μ reactions, the cosmic e and μ particles are transferred to the cosmic ν_e and ν_μ neutrinos, respectively. The observation of the enhanced cosmic ν_e and ν_μ neutrinos is the indirect evidence of the B1 dark matters. Also, the B1 dark matters can be produced from the LHC accelerator. The reaction between this B1 dark matter and the electron can enhance the electron neutrinos. It will be interesting to carry out this experiment at LHC.

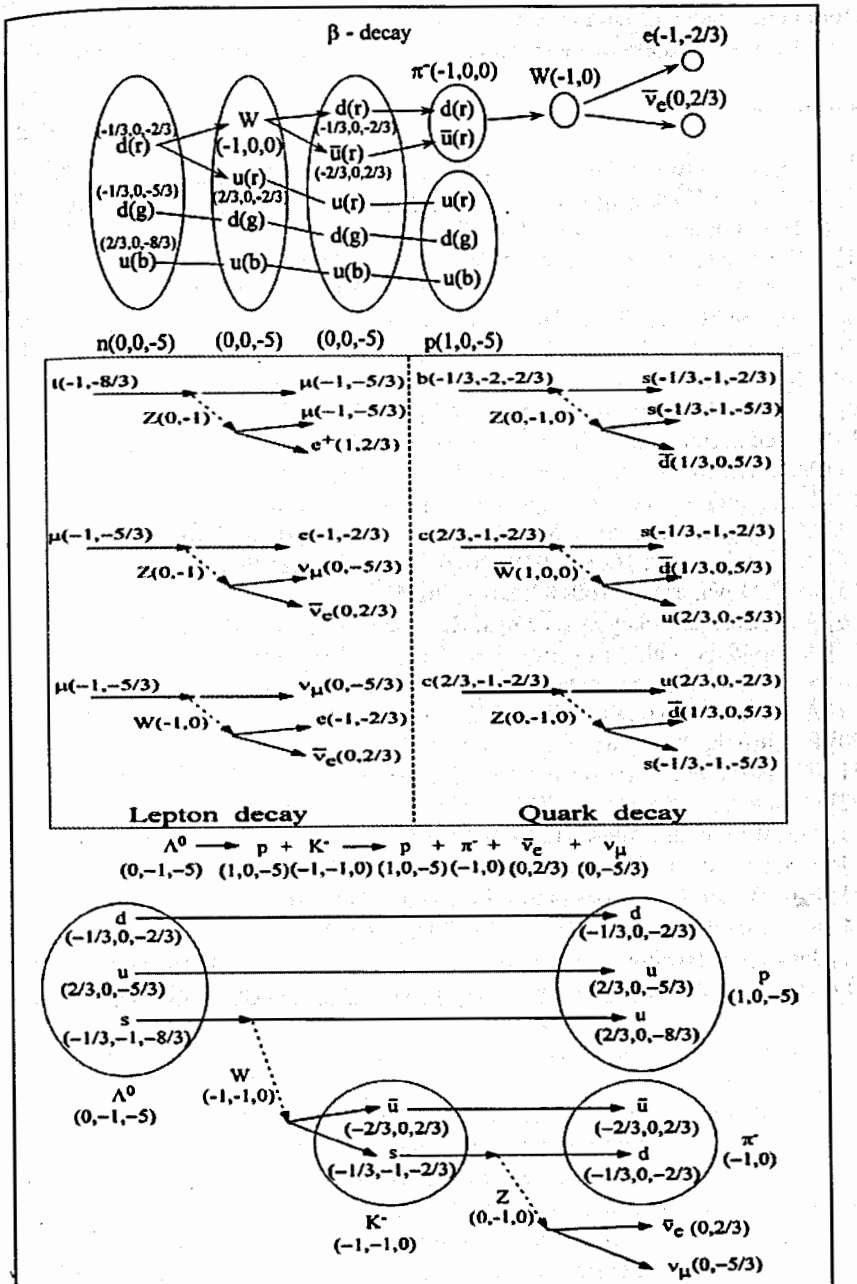

Fig. 10. Several examples of elementary particle decays.

More details can be found in Refs. 1, 2 and 27.
E-mail contact address of Jae-Kwang Hwang is jkhwang.koh@gmail.com

References

[1] Jae-Kwang Hwang, https://www.researchgate.net/publication/313247136
[2] Jae-Kwang Hwang, https://www.researchgate.net/publication/297270485
[3] S. Hussain, arXiv: 1301.6619v1 (2013).
[4] Y.F. Liang et al., Phys. Rev. D 93, 103525 (2016).
[5] M. Ackermann et al., arXiv: 1302.3307v1 (2013).
[6] T. Siegert et al., arXiv: 1603.01169 (2016).
[7] V. Gammaldi, arXiv: 1412.7639 (2014).
[8] P. Meszaros et al., www2.astro.psu.edu/users/nnp/cr.html.
[9] J.N. Bahcall and E. Waxman, Phys. Lett. B556, 1 (2003).
[10] S. Federicici et al., arXiv: 1502.06355v1 (2015).
[11] M.G. Aartsen et al., arXiv: 1412.5106 (2014).
[12] L. Accardo et al., Phys. Rev. Lett. 113, 121101 (2014).-
[13] M. Aguilar et al., Phys. Rev. Lett. 113, 121102 (2014); 110, 141102 (2013).
[14] P. Lipari, arXiv: 1608.02018 (2016) and references there in.
[15] M.T. Dova, arXiv: 160407584v1 (2016).
[16] A.J. Krasznahorkay et al., Phys. Rev. Lett. 116, 042501 (2016).
[17] A. Goudeis et al., Phys. Rev. Lett. 116, 211303 (2016).
[18] K. Lane and L. Pritchett, arXiv: 1701.07376 (2017).
[19] A. Heister, arXiv: 1610.06536 (2016).
[20] R. Ehrlich, Astropart. Phys. 35, 625 (2012).
[21] F. Vissani et al., arXiv: 1008.4726v1 (2010).
[22] G. Schatz, arXiv: 1507.07107v1 (2015).
[23] M. Turler et al., A&A 512, A49 (2010).
[24] Yong Shi et al., The Astrophysical Journal 777, 6 (2013).
[25] P.A. Boldin et al., Astronomy Letters 39, 375 (2013).
[26] N. Cappelluti et al., arXiv: 1701.07932 (2017).
[27] Jaekwang Hwang, Talk at American physical society April meeting 2017, January 28-31, 2017, https://absuploads.aps.org/presentation.cfm?pid=12521

The Recent Results from Super-Kamiokande

Takatomi Yano for Super-Kamiokande Collaboration

Abstract:

The Super-Kamiokande (SK) is the world-largest water Cherenkov detector, running for neutrino observations and proton decay search over 20 years. Because of its high statistics due to the large fiducial volume of 22.5 kt, lower cosmic-ray background environment in a mine at 1000m underground, and well-calibrated detector itself, Super-K has been making the world-leading results in several region of particle physics. Here, recent results from the study of atmospheric and solar neutrino are presented.

1. The Super-Kamiokande Detector

Super-Kamiokande (SK) is the world-largest water Cherenkov detector, located at 1,000 m underground (2,700 m water equivalent) in Ikenoyama mountain, Gifu-prefecture, Japan [1]. The cylindrical detector tank with the dimensions of the 39.3 (33.8) m in diameter and 41.4 (36.2) m in height provides 50 (22.5) kton full (fiducial) volume of ultra-pure water. The detector tank is optically and physically separated into inner detector (ID) and outer detector (OD), which have the 11,129 20-inch-diameter photomultipliers (PMTs) and 1,885 8-inch-PMTs for the Cherenkov light detection respectively. The Cherenkov light patterns provide the information about the original charged particles, on thier energies, directions and particle types. SK detector covers the energy range from a few MeV to tens of GeV. The measurement by SK was started at 1996 and has been continued over twenty years. The most recent and fourth experimental period, called SK-IV, is stated at September 2008 with new data acquisition frontends. SK has also cooperated with the accelerator neutrino experiments as the far detector, for K2K [2] and T2K [3] experiments.

2. Atmospheric neutrinos

Atmospheric neutrinos originated with the interaction of cosmic rays with nuclei in the air. The interaction provides pions and kaons, and neutrinos as the results of their decay. The atmospheric neutrinos have the wide energy range of 100 MeV to 100 TeV, the wide range of travel length of 10 km to 13,000 km, and the various components of ν_e, ν_μ and their anti-particles [4]. Utilizing these properties, various studies on the properties of neutrinos have been conducted. The data from all the phases of SK-I/II/III (0.33 Mt year) and 2520 days live time of SK-IV, until March 2016, are used for following analysis.

The neutrino oscillations of atmospheric neutrinos are led by ν_μ to ν_τ oscillation, which causes the deficit of ν_μ in the upward-going Multi-GeV and partially contained event samples. Though, it is difficult to identify the appearance of ν_τ.

This is because the production of τ leptons requires high energy neutrinos, where the flux is small, and also τ leptons decay into hadronic particles mainly. It is still important to confirm the appearance of ν_τ, to check the oscillation framework. The analysis with neural network was applied to search tau-neutrino decay in SK detector. The neural network was trained by non-τ and τ Monte Carlo (MC) events and likelihood ranging from 0 to 1 was provided as the output for each event. Some more details could be found in our previous papers [5,6]. Figure 1 shows the two-dimensional histogram of τ (left) and non-τ MC (center) events. We can see, the τ-like events are concentrated at the upward direction, at around -1 in cosine of the zenith angle, for the τ MC events. These distributions are utilized as the probability density functions for tau-neutrino events and background (BG) events. The analysis was conducted by fitting real data to a linear combination of two-dimensional histograms, which included a systematic error term:

Data = BG PDF + α τ-PDF + $\Sigma\varepsilon_i$ PDF_i

α is the parameter to be fitted, and it was expected to be 1 under the assumption of the standard three-flavor oscillation framework and the standard cross-section of neutrinos. PDF_i is the PDF of the i^{th} systematic errors, and ε_i is the magnitude of a nuisance parameter in the fit. After the unbinned likelihood fit, we got the result of α= 1.47±0.32 under the hypothesis of normal neutrino mass hierarchy (4.6σ from 0, whereas 3.3σ was expected). Figure 1 (right) shows the zenith angle distribution of tau-like events overlaid by the fitted MC distributions; the shaded part shows the contributions of tau-neutrino events. This is the evidence of the tau-neutrino appearance in atmospheric neutrino, and the result is consistent with the standard three-flavor oscillation framework.

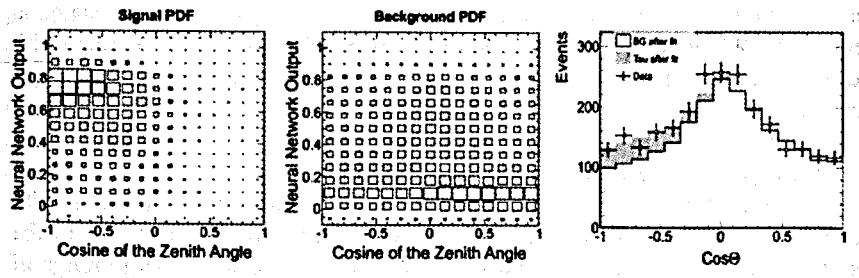

Fig. 1 Probability distribution functions for the τ neutrino (left) and non-τ neutrino events (center). The zenith angle distribution of data and Monte Carlo events (right).

Because of the recent result of large θ_{13} value in several neutrino experiments, the three-flavor oscillation analysis is required for precise understanding of the neutrino properties with atmospheric neutrinos, such as Δm^2_{32}, θ_{23} octant, δ_{CP} and

mass hierarchy. The atmospheric neutrino samples are subdivided into 19 event categories by their topologies (fully-contained, partially-contained and up-going-muon), energies (sub-GeV and multi-GeV), flavors (electron- or muon-like) and the number of Cherenkov rings. Multi-GeV- multi-ring- electron-like- events are further classified into neutrino and anti-neutrino categories, using a difference of number of associated decay electrons, number of rings, transverse momentum, and the fraction of momentum carried out by most energetic rings. It is motivated by the oscillation scenario, that the oscillation from ν_μ to ν_e is enhanced by the Earth matter effect under normal mass hierarch hypothesis, at around 5-10 GeV. Anti-ν_μ to anti-ν_e oscillation will be enhanced at same energies, in case of inverted mass hierarchy. In following likelihood analysis, $\sin^2\theta_{13}$ is fixed by the reactor neutrino experimental results of $\sin^2\theta_{13}$ = 0.0219 (PDG2015 [7]). $\sin^2\theta_{12}$ and Δm^2_{21} is constrained by the result of solar neutrino experiments and that of KamLAND.

Figure 2 shows the obtained oscillation analysis results using only SK data. In the figure, $\Delta\chi^2$ is determined as a function of $|\Delta m^2_{32}|$ or $|\Delta m^2_{13}|$, $\sin^2\theta_{23}$ and δ_{CP}. The best fit parameters for normal and inverted hierarchy hypotheses are shown in Table "**". The result of$\Delta\chi^2 = \chi^2_{NH} - \chi^2_{IH}$ = -4.3 is achieved and prefers the normal hierarchy hypothesis, where$\Delta\chi^2$ =-3.1 of sensitivity is expected from Asimov data set with normal hierarchy. To check the significance, Monte Carlo samples are generated and analyzed as the real data. In case we adopt the inverted hierarchy for MC samples, the probability to obtain$\Delta\chi^2$ = -4.3 or less is 0.031 ($\sin^2\theta_{23}$ = 0.6) and 0.007 ($\sin^2\theta_{23}$ = 0.4). In case we adopt normal hierarchy for MC generation, the probability was 0.446 ($\sin^2\theta_{23}$ = 0.4).

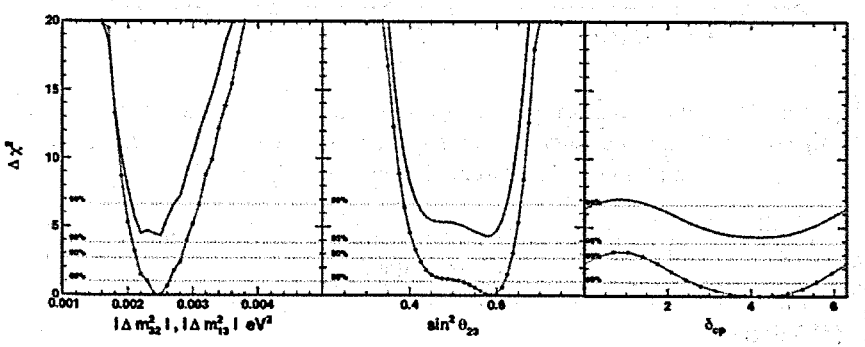

Fig. 2 $\Delta\chi^2$ as a function of $|\Delta m^2_{32}|$ or $|\Delta m^2_{13}|$ (left), $\sin^2\theta_{23}$ (center) and δ_{CP} (right) with SK data only. The blue and orange lines show $\Delta\chi^2$ for a normal and inverted hierarchy hypothesis, respectively

Tab. 1 Best-fit values for the 3-flavor oscillation analysis with SK only data.

Fit (517 dot)	χ^2	$\sin^2\theta_{13}$	δ_{CP}	$\sin^2\theta_{23}$	Δm^2_{23} [eV^2]
SK (NH)	571.74	0.0219 (fixed)	4.189	0.587	$2.5\cdot10^{-3}$
SK (IH)	576.08	0.0219 (fixed)	4.189	0.575	$2.5\cdot10^{-3}$

Figure 3 shows the preliminary results using SK and public T2K data. Table 2 shows the best-fit values for the likelihood fit. The result is $\Delta\chi^2 = \chi^2_{NH} - \chi^2_{IH} = -5.2$ and also prefers normal hierarchy hypothesis. $\Delta\chi^2 = -3.8$ of sensitivity is expected from Asimov data set assuming normal hierarchy. With a toy Monte Carlo study assuming inverted hierarchy, the probability to have$\Delta\chi^2$ less than -5.2 is 0.024 ($\sin^2\theta_{23} = 0.6$) and 0.001 ($\sin^2\theta_{23} = 0.4$).

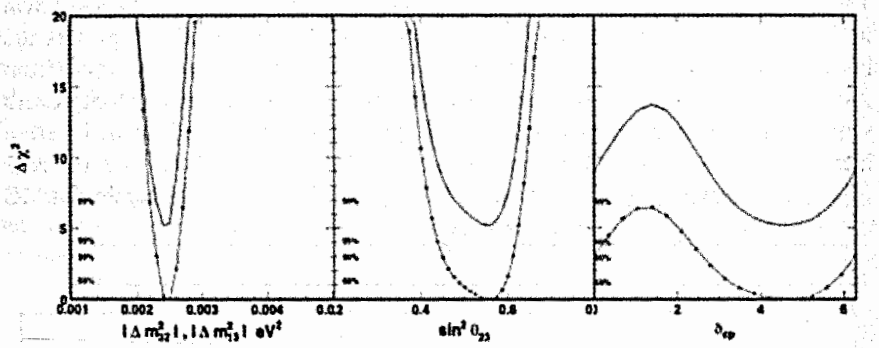

Fig. 3 $\Delta\chi^2$ as a function of $|\Delta m^2_{32}|$ or $|\Delta m^2_{13}|$ (left), $\sin^2\theta_{23}$ (center) and δ_{CP} (right) with SK + T2K external data. The blue and orange lines show $\Delta\chi^2$ for a normal and inverted hierarchy hypothesis, respectively.

Tab. 2 Best-fit values for the 3-flavor oscillation analysis with SK + T2K external data.

Fit (585 dot)	χ^2	$\sin^2\theta_{13}$	δ_{CP}	$\sin^2\theta_{23}$	Δm^2_{23} [eV^2]
SK (NH)	639.61	0.0219 (fixed)	4.887	0.55	$2.4\cdot10^{-3}$
SK (IH)	644.82	0.0219 (fixed)	4.538	0.55	$2.5\cdot10^{-3}$

3. Solar neutrinos

The dominant solar neutrino signals at SK are so called ^{8}B neutrinos generated in pp-chain, a series of nuclear fusion reactions in the Sun. The observed event rate at SK is about 20 events/day with the large fiducial volume of 22.5 kton. With the high statistics data, we have performed searches for time variation of the solar neutrino flux, energy spectrum distortion due to the oscillation effect as well as precise measurement of the oscillation parameter Δm^2_{21}, $\sin^2\theta_{12}$. In following analysis, we use the SK-I, II, III (1496, 791 and 548 days) + 2365 days of SK-IV data, until March 2016. Here, two years equivalent data is newly added, comparing to previous paper with 1664 days data of SK-IV [8]. Because we lowered the trigger threshold at May 2015, some of the new data sets have the analysis threshold of $E_{kin} = 3.5$ MeV at kinetic energy of electrons. It aims at measuring the solar neutrino energy spectrum distortion, and the effort to lower the threshold down to $E_{kin} = 2.5$ MeV is now underway with new data acquisition system.

As the result of SK I-IV combined flux analysis, about 84,000 signals of solar neutrinos is extracted. The flux ratio of the data to the standard solar model (SSM) prediction is Data/SSM = 0.4486±0.0062 (stat. + sys.), where the neutrino oscillation is not taken into account for SSM prediction. In the comparison of each experimental phases of SK, these solar rate measurement results are fully consistent with a constant solar neutrino flux. Figure 4 shows the yearly variation of the solar neutrino flux. The solar activity cycle estimated from the sunspot number is about 11 years. SK has observed the solar neutrinos over these 19 years and above 1.5 cycles has passed. However, no significant correction with the solar activity is seen. For the constant flux hypothesis, χ^2 = 15.52/19 D.O.F, which correspond to 68.9% probability.

Using the most up-to-date SK solar neutrino data and the latest results of other solar neutrino experiments, the allowed regions of the oscillation parameters are obtained. In Fig. 5, we performed the oscillation analysis by constraining $\sin^2\theta_{13}$ as 0.0219±0.0014, referring reactor neutrino experiments. We see 2σ tension between the solar-global and KamLAND reactor data in Δm^2_{21}. A there-flavor oscillation analysis without the constraint on $\sin^2\theta_{13}$ is also performed. The result is also shown in Fig 5. By combining the SK solar measurement results, the results of other solar experiments and KamLAND, the non-zero θ_{13} value is obtained by 2σ level ($\sin^2\theta_{13} = 0.029^{+0.014}_{-0.015}$). The result is also consistent with that of reactor experiments.

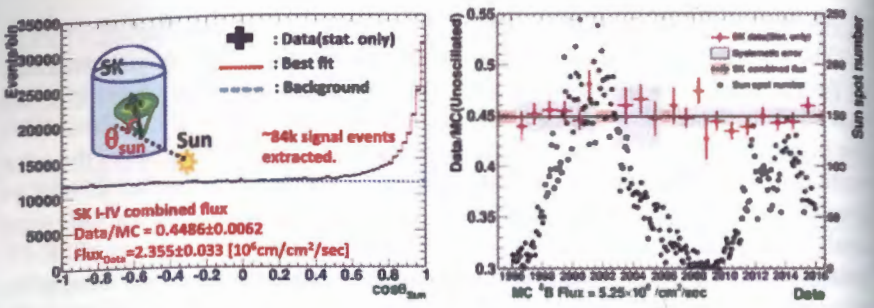

Fig. 4 The distribution of the cosine between the direction of the Sun and the reconstructed direction of electrons (left). The yearly variation of relative ratio between SK data and an un-oscillated MC prediction (right). The black dots show the sunspot numbers for referring solar activity, taken from [9].

4. Other recent results

With its indispensable detector characteristics, SK has been making unique searches for new physics. The first of them would be nucleon decay search, strongly motivated by Grand Unification Theories (GUTs). Some GUTs predict the proton lifetimes shorter than 10^{34} years and SK could prove it. Since the grand unification occurs at around 10^{16} GeV, which cannot be achieved by any accelerator experiments, nucleon decay at SK is a unique way to directly probe them. So far, no evidence of nucleon decay is observed in any decay mode yet. Our past search results for several decay mode, e.g. proton to $e^+\pi^0$ or νK^+, can be found at [10,11].

The searches for new neutrino sources are also our interest and important for the astroparticle physics. Searches for WIMPs (Weakly Interacting Massive Particles) by neutrinos, which are produced by the annihilation of WIMPs occurring inside Sun, are ongoing in SK. The previous work can be found in [12]. There were no significant signals but stringent limits were set. SK gives limits lower than 200 GeV for the spin-dependent cross section, and lower than 6 GeV for the spin-independent cross section. Searches for neutrino signals from the Earth and the Galaxy are currently ongoing.

On September 2015, LIGO identified the first evident signal of a gravitational wave originated a merger of two black holes [13]. Given the fact, a search for coincident neutrino signals in SK was performed for GW150914 and GW151226. Coincident production of neutrinos are possible to imagine, because of the tremendous energies involved in the mergers and unknown nature of the region of black holes, e.g. formation of relativistic jets. The signal searches were performed for the time window of ±500 seconds around these gravitational wave detection times and for a wide energy range from 3.5 MeV to 100 PeV. Four neutrino

candidates are found for GW150914 and no candidates are found GW151226. These candidates were consistent with the expected background events [14].

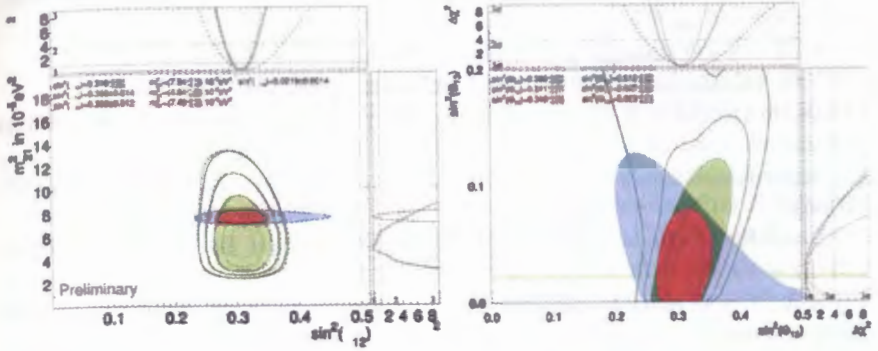

Fig. 5 Allowed regions of oscillation parameters for θ_{13} constrained analysis (left) and 3-flavor oscillation analysis with solar experiments and KamLAND (right). The green area shows the results of solar global analysis (green), light blue for KamLAND reactor and red for solar + KamLAND. The best-fit parameters and their 1σ errors are shown in the figure.

5. Conclusions

Recent results from the study of atmospheric, solar neutrinos and other topics for nucleon decay and astrophysical neutrino searches are presented.. Using the large data samples of atmospheric neutrinos at SK, three-flavor oscillation analyses are performed. The result of neutrino mass hierarchy test was obtained as $\Delta\chi^2 = \chi^2_{NH} - \chi^2_{IH} = -4.3$ with SK only data, where -3.1 is expected from the same analysis of Asimov data set assuming the best fit parameters. With the SK+T2K data sets, the result was $\Delta\chi^2 = \chi^2_{NH} - \chi^2_{IH} = -5.2$ with SK only data, where -3.8 is expected. These results strongly support the normal hierarchy hypothesis. The analysis of tau neutrino appearance in atmospheric neutrino oscillation is updated and gives a non-zero significance of 4.6σ. The measurement of solar neutrino is also updated. The observed neutrino flux ratio comparing to un-oscillated SSM expectation was Data/MC = 0.4486±0.0062, and measurements in each experimental period of SK is fully consistent with constant solar neutrino flux. No significant correlation with the solar activity is seen. The solar neutrino oscillation analysis is also updated. The global analysis with the results of other solar experiments gives lower Δm^2_{21} value than that of KamLAND by more than 2σ. A three-flavor oscillation analysis with solar neutrinos, without constrain of $\sin^2\theta_{13}$ by the reactor experiments, also give the consistent results for the oscillation

parameters and non-zero θ_{13} value by 2σ level.

References

[1] Super-Kamiokande collaboration (Y. Fukuda et al.), Nucl. Instrum. Meth. A501: 418-462 (2003).
[2] K2K collaboration (S.H. Ahn et al.), Phys. Lett. B 411:178-184 (2001).
[3] T2K collaboration (Y. Itow et al.), arXiv:hep-ex/0106019 (2001).
[4] Super-Kamiokande collaboration (E. Richard et al.), Phys. Rev. D 94 052001 (2016).
[5] Super-Kamiokande collaboration (K. Abe et al.), Phys. Rev. Lett., 97 171801 (2006).
[6] Super-Kamiokande collaboration (K. Abe et al.), Phys. Rev. Lett., 110 181802 (2013).
[7] K A Olive et al. (Particle Data Group), Chin. Phys. C, 38 090001 (2014) and 2015 update.
[8] Super-Kamiokande collaboration (K. Abe et al.), Phys. Rev. D 94 052010 (2016).
[9] http://www.sidc.be/silo/datafile. Source: WDC-SILSO, Royal Observatory of Belgium, Brussels
[10] Super-Kamiokande collaboration (H. Nishino et al.), Phys. Rev. D 85 112001 (2012).
[11] Super-Kamiokande collaboration (K. Abe et al.), Phys. Rev. D 90 072005 (2014).
[12] Super-Kamiokande collaboration (K. Choi et al.), Phys. Rev. Lett., 114 141301 (2015).
[13] LIGO and Virgo collaborations (B. P. Abbott et al.), Phys. Rev. Lett., 116 061102 (2016).
[14] Super-Kamiokande collaboration (K. Abe et al.), Astrophys. J. Lett. Vol. 830 1 (2016).

Double-Beta Decay with Single-Electron Emission

A. Babič,[1,2] D. Štefánik,[3] M. I. Krivoruchenko,[2,4,5] and F. Šimkovic[1,2,3]

[1] *Czech Technical University in Prague, 128 00 Prague, Czech Republic*
[2] *Joint Institute for Nuclear Research, 141980 Dubna, Russia*
[3] *Comenius University in Bratislava, 842 48 Bratislava, Slovakia*
[4] *Institute for Theoretical and Experimental Physics, 117218 Moscow, Russia*
[5] *Moscow Institute of Physics and Technology, 141700 Moscow, Russia*

Abstract: We study a new mode of the neutrinoless and two-neutrino double-beta decay in which a single electron is emitted from the atom. The other electron is directly produced in one of the available $s_{1/2}$ or $p_{1/2}$ subshells of the daughter ion. The neutrinoless electron-production mode $0\nu\mathrm{EP}\beta^-$, which would manifest through a monoenergetic peak at the endpoint of the single-electron energy spectrum, is shown to be inaccessible to the future experiments. Conversely, its two-neutrino counterpart $2\nu\mathrm{EP}\beta^-$ might have already influenced the single-electron spectra measured, e.g., for the isotope ^{100}Mo in the experiment NEMO 3. We discuss the prospects for detecting these new modes also for ^{82}Se in its forthcoming successor SuperNEMO.

Keywords: double-beta decay, atomic shell, single-electron spectrum

I. Introduction

The discovery of neutrino oscillations marked the beginning of a new era in neutrino physics, main feature of which is the question of the origin and absolute scale of neutrino masses. Observation of the neutrinoless double-beta decay would imply a Majorana nature of massive neutrinos ν_i $(i = 1, 2, 3)$, a consequence of which would be the identity of the flavor neutrinos ν_α $(\alpha = e, \mu, \tau)$ and their respective antineutrinos $\bar{\nu}_\alpha$ [1]. Moreover, it would bring us compelling evidence that the total lepton number L is not strictly conserved in the nature. The search for this elusive process provides us with means to set upper limits on the absolute scale of neutrino masses, as well as with a unique access to the mechanism of CP violation in the lepton sector which is necessary in order to explain the observed baryon asymmetry of the Universe [2].

The most widespread form of the double-beta decay $2\nu\beta^-\beta^-$ involves a transmutation of an even-even parent nucleus ${}^{A}_{Z}\mathrm{X}$ into an even-even daughter nucleus ${}^{A}_{Z+2}\mathrm{Y}$, accompanied by an emission of two electrons e^- and a pair of electron antineutrinos $\bar{\nu}_e$ from the atom, while in its hypothetical neutrinoless version $0\nu\beta^-\beta^-$ the antineutrinos are absent:

$$ {}^{A}_{Z}\mathrm{X} \longrightarrow {}^{A}_{Z+2}\mathrm{Y} + e^- + e^- + (\bar{\nu}_e + \bar{\nu}_e). $$

The neutrinoless mode $0\nu\beta^-\beta^-$ increases L by 2 units and could be discovered in calorimetric measurements of the sum of electron energies by revealing a monoenergetic peak at the two-electron spectrum endpoint corresponding to the total released kinetic energy Q. The two-neutrino mode $2\nu\beta^-\beta^-$ has been so far observed for 11 out of 35 even-even isotopes for which the ordinary β^- decay into the odd-odd intermediate nucleus is either energetically forbidden or substantially suppressed by spin selection rules [3]. In this work, we focus on the $0^+ \longrightarrow 0^+$ ground-state transition of the isotope ^{100}Mo which had been extensively studied throughout the operation of the tracking-and-calorimetry double-beta-decay experiment NEMO 3 located at the Modane Underground Laboratory (LSM), France [4].

In 1992, Jung *et al.* have observed for a first time the bound-state β^- decay in which the electron is directly produced in atomic K or L shell and the monochromatic electron antineutrino carries away essentially the entire energy of the decay [5]. The group has studied bare $^{163}_{66}Dy^{66+}$ ions collected in a heavy-ion storage ring at GSI, Darmstadt, and deduced a half-life of 47 d for the otherwise stable isotope. It has been since stressed that such rare form of the β^- decay might play a crucial role in stellar plasma where highly-ionized atoms participate in the nucleosynthesis. In this work, we propose to study the bound-state double-beta decay $0\nu\mathrm{EP}\beta^-$ ($2\nu\mathrm{EP}\beta^-$):

$$ {}^{A}_{Z}\mathrm{X} \longrightarrow {}^{A}_{Z+2}\mathrm{Y} + e^-_b + e^- + (\bar{\nu}_e + \bar{\nu}_e), $$

where a single free electron e^- is emitted from the nucleus, while the electron production (EP) of a bound electron e^-_b is assumed to fill one of the available $s_{1/2}$ or $p_{1/2}$ orbitals above the valence shell of the daughter ion ${}^{A}_{Z+2}\mathrm{Y}^{2+}$. Inclusion of the bound states with higher angular momenta is not necessary since their wave functions experience only a negligible overlap with the nucleus. These new single-electron modes exhibit a distinctive kinematics and could be in principle recognized by their characteristic signal induced in the double-beta-decay detectors. For instance, $0\nu\mathrm{EP}\beta^-$ (being effectively a two-body decay) should be searched for in the form of a monoenergetic peak at the endpoint of the energy distribution of individual electrons. The single-electron spectra have been measured in the NEMO 3 experiment and will be surveyed with enhanced accuracy in its forthcoming successor SuperNEMO [6].

II. Calculation of Phase-Space Factors

The double-beta decay can occur in the 2nd order of the effective β-decay Hamiltonian [7]:

$$ \mathcal{H}_\beta(x) = \frac{G_\beta}{\sqrt{2}} \bar{e}(x)\gamma^\mu(1-\gamma^5)\nu_e(x) j_\mu(x) + \mathrm{H.c.}, $$

where $G_\beta = G_\mathrm{F}\cos\theta_\mathrm{C}$ contains the Fermi constant G_F and Cabibbo angle $\theta_\mathrm{C} \cong 13°$ [8], $e(x)$ and $\nu_e(x)$ denote the electron and electron-neutrino fields, respectively, and $j_\mu(x) = \bar{p}(x)\gamma_\mu(g_V - g_A\gamma^5)n(x)$ is the hadronic charged current involving the proton $p(x)$ and neutron $n(x)$ fields with the vector $g_V = 1$ and (unquenched) axial-vector $g_A = 1.269$ weak coupling constants. Due to neutrino mixing, the left-handed components of the flavor-neutrino fields $\nu_\alpha(x)$ are in fact linear combinations of the underlying massive-neutrino fields $\nu_i(x)$ given by the unitary PMNS matrix: $\nu_{\alpha L}(x) = \sum_i U_{\alpha i}\nu_{iL}(x)$.

Assuming the Majorana nature of massive neutrinos and employing the standard approximations, the formula for the inverse $0\nu\beta^-\beta^-$ half-life can be brought into the following form [1]:

$$ \left(T^{0\nu\beta\beta}_{1/2}\right)^{-1} = g_A^4 G^{0\nu\beta\beta}(Z,Q)\left|M^{0\nu\beta\beta}\right|^2 \left|\frac{m_{\beta\beta}}{m_e}\right|^2. $$

Here, the phase-space factor $G^{0\nu\beta\beta}(Z,Q)$ depends solely on the kinematics of the involved particles, the nuclear matrix element $M^{0\nu\beta\beta}$ can be in principle determined from the theory of nuclear structure, and the effective Majorana neutrino mass $m_{\beta\beta} = \sum_i U_{ei}^2 m_i$ is a function of (yet unknown) parameters of the neutrino physics; to this day, arguably the most stringent limits have been obtained in the ^{136}Xe double-beta-decay experiments KamLAND-Zen and EXO-200, with the former providing a constraint as low as [9]: $|m_{\beta\beta}| < 165$ meV. On the contrary, the formula for the inverse $2\nu\beta^-\beta^-$ half-life can be derived within the Standard Model [10]:

$$ \left(T^{2\nu\beta\beta}_{1/2}\right)^{-1} = g_A^4 G^{2\nu\beta\beta}(Z,Q)\left|m_e M^{2\nu\beta\beta}\right|^2. $$

For the single-electron modes $0\nu\mathrm{EP}\beta^-$ and $2\nu\mathrm{EP}\beta^-$, their respective inverse half-lives $\left(T^{0\nu\mathrm{EP}\beta}_{1/2}\right)^{-1}$ and $\left(T^{2\nu\mathrm{EP}\beta}_{1/2}\right)^{-1}$ exhibit a structure fully analogous to the aforementioned, the only distinction being in the corresponding phase-space factors $G^{0\nu\mathrm{EP}\beta}(Z,Q)$ and $G^{2\nu\mathrm{EP}\beta}(Z,Q)$. Since these quantities depend crucially on the atomic structure, we employed a fully relativistic description of the final-state electrons in terms of the solutions to the Dirac equation with centrally-symmetric potential [11]:

$$ \psi_{\kappa\mu}(\vec{r}) = \begin{pmatrix} f_\kappa(r)\Omega_{\kappa\mu}(\hat{r}) \\ i g_\kappa(r)\Omega_{-\kappa\mu}(\hat{r}) \end{pmatrix}, $$

where the radial wave functions $f_\kappa(r)$ and $g_\kappa(r)$ depend on the energy of the electron, while the angular functions $\Omega_{\kappa\mu}(\hat{r})$, also known as the spinor spherical harmonics, are common for both the discrete and continuous spectrum. The quantum number $\kappa = (l-j)(2j+1) = \pm 1, \pm 2, \ldots$ collectively labels all possible couplings of the orbital $l = 0,1,\ldots$ and spin $s = \pm 1/2$ angular momenta, while $\mu = -j, \ldots, +j$ denotes the projection of the total angular momentum $j = |l+s|$ onto the z-axis.

For the $0\nu\mathrm{EP}\beta^-$ and $2\nu\mathrm{EP}\beta^-$ phase-space factors we have derived the following formulae:

$$G^{0\nu\mathrm{EP}\beta} = \frac{G_\beta^4 m_e^2}{32\pi^4 R^2 \ln 2} \sum_{n=n_{\min}}^{\infty} B_n(Z,A) F(Z+2,E) Ep,$$

$$G^{2\nu\mathrm{EP}\beta} = \frac{G_\beta^4}{8\pi^6 m_e^2 \ln 2} \sum_{n=n_{\min}}^{\infty} B_n(Z,A) \int_{m_e}^{m_e+Q} \mathrm{d}E F(Z+2,E) Ep \int_0^{m_e+Q-E} \mathrm{d}\omega_1 \omega_1^2 \omega_2^2.$$

In the first equation, the nuclear radius R is by convention included explicitly in order to make the nuclear matrix element $M^{0\nu\beta\beta}$ dimensionless. The factor of $\ln 2$ comes from the relation between the decay rate $\Gamma = \ln 2/T_{1/2}$ and half-life $T_{1/2}$.

The quantity $B_n(Z,A)$ is a bound-state analogue of the Fermi function familiar from the theory of beta decay:

$$B_n(Z,A) = f_{n,-1}^2(R) + g_{n,+1}^2(R),$$

where the two terms originate from the inclusion of $\mathrm{s}_{1/2}$ and $\mathrm{p}_{1/2}$ bound states, respectively. In order to properly account for the relativistic many-electron atomic structure and the shielding effect of nuclear charge, the radial wave functions $f_{n,-1}(R)$ and $g_{n,+1}(R)$ of the bound electron e_b^- at the nuclear radius $R = 1.2\ \mathrm{fm}\ A^{1/3}$ were evaluated by means of the multiconfiguration Dirac–Hartree–Fock package GRASP2K [12, 13]. The computation was performed assuming the electron configuration of the parent atom ${}^A_Z\mathrm{X}$, with the daughter isotope ${}^A_{Z+2}\mathrm{Y}$ being the source of nuclear Coulomb attraction, for all available electron shells above the valence shell ($n_{\min} = 5$ for ${}^{100}_{42}\mathrm{Mo}$) up to $n = 9$. Since in the absence of atomic shielding the squared electron wave functions near the origin decrease as n^{-3} [14], the rest of electron shells were to a good accuracy approximated by a fit of the calculated values using the power function cn^{-p} and summed analytically via the Riemann zeta function $\zeta(p)$. Since the convergence could not be achieved in case of the $6\mathrm{s}_{1/2}$ orbital, the value of $f_{6,-1}^2(R)$ has been replaced by the one predicted by the fit.

The Fermi function $F(Z,E)$, which involves the continuous-spectrum radial wave functions $f_{-1}(E,R)$ and $g_{+1}(E,R)$ evaluated on the nuclear surface R, can be approximated by the expression for the relativistic $\mathrm{s}_{1/2}$ wave [15]:

$$F(Z,E) = f_{-1}^2(E,R) + g_{+1}^2(E,R) \approx 4\left[\frac{|\Gamma(\gamma+iy)|}{\Gamma(2\gamma+1)}\right]^2 (2pR)^{2\gamma-2} e^{\pi y},$$

where $\gamma = \sqrt{1-(\alpha Z)^2}$, $y = \alpha ZE/p$, and $p = |\vec{p}|$ is the momentum magnitude of the free electron e^- with energy $E = \sqrt{\vec{p}^2 + m_e^2}$. In the results, the Fermi function $F(Z+2,E)$ assumes the full charge of the daughter nucleus ${}^A_{Z+2}\mathrm{Y}$, since in the continuum the shielding effect has been shown to be rather insignificant [16].

In $G^{0\nu\mathrm{EP}\beta}$, the free-electron energy is fixed by the energy conservation: $E = m_e + Q$, where we have neglected the nuclear recoil as well as the binding energy of the bound electron e_b^-. In $G^{2\nu\mathrm{EP}\beta}$, similar approximations erase the dependence on n from the integral boundaries and, in turn, an infinite sum of integrals simplifies into a product of $\sum_{n=n_{\min}}^{\infty} B_n(Z,A)$ and just one double integral; in the integral over the first-neutrino energy ω_1, the second-neutrino energy is once again constrained by the energy conservation: $\omega_2 = m_e + Q - E - \omega_1$.

III. Half-Lives and Single-Electron Spectra

In Table I, we present the values of the $0\nu\beta^-\beta^-$ and $0\nu\mathrm{EP}\beta^-$ phase-space factors $G^{0\nu\beta\beta}$ and $G^{0\nu\mathrm{EP}\beta}$ obtained for the $0^+ \longrightarrow 0^+$ ground-state transition of the isotope ${}^{100}\mathrm{Mo}$ with total released kinetic energy $Q = 3.034$ MeV [17], assuming the unquenched value of the axial-vector weak coupling constant $g_A = 1.269$. We also evaluate the ratio between the corresponding decay rates: $\Gamma^{0\nu\mathrm{EP}\beta}/\Gamma^{0\nu\beta\beta} = G^{0\nu\mathrm{EP}\beta}/G^{0\nu\beta\beta}$, which is independent of the nuclear matrix element $M^{0\nu\beta\beta}$ and effective Majorana neutrino mass $m_{\beta\beta}$, and hence free of the peculiarities of the nuclear and neutrino physics. Finally, we estimate the $0\nu\beta^-\beta^-$ and $0\nu\mathrm{EP}\beta^-$ half-lives $T_{1/2}^{0\nu\beta\beta}$ and $T_{1/2}^{0\nu\mathrm{EP}\beta}$ based on the value of the nuclear matrix element $|M^{0\nu\beta\beta}| = 5.850$ calculated in [18] via the spherical pn-QRPA approach including the realistic CD-Bonn nucleon-nucleon potential with short-range correlations and partial isospin-symmetry restoration, and assuming the value of the effective Majorana neutrino mass $|m_{\beta\beta}| = 50$ meV which is compatible with the inverted hierarchy of neutrino masses. The value obtained for the decay-rate ratio $\Gamma^{0\nu\mathrm{EP}\beta}/\Gamma^{0\nu\beta\beta}$ suggests a suppression of the single-electron mode $0\nu\mathrm{EP}\beta^-$ by 6 orders of magnitude, which is mainly attributed to the presence of other electrons in the inner atomic shells: the lowest-lying orbitals (which would otherwise provide the largest contributions to the decay rate $\Gamma^{0\nu\mathrm{EP}\beta}$) are already occupied, while the shielding effect of nuclear charge substantially reduces the bound-state wave functions on the surface of the nucleus. The estimated half-life $T_{1/2}^{0\nu\mathrm{EP}\beta}$ further confirms that the mode $0\nu\mathrm{EP}\beta^-$ is very unlikely to be observed in the present and near-future experiments.

Table I. $0\nu\beta^-\beta^-$ and $0\nu\mathrm{EP}\beta^-$ phase-space factors $G^{0\nu\beta\beta}$ and $G^{0\nu\mathrm{EP}\beta}$, decay-rate ratio $\Gamma^{0\nu\mathrm{EP}\beta}/\Gamma^{0\nu\beta\beta} = G^{0\nu\mathrm{EP}\beta}/G^{0\nu\beta\beta}$ and half-lives $T_{1/2}^{0\nu\beta\beta}$ and $T_{1/2}^{0\nu\mathrm{EP}\beta}$ for the isotope ^{100}Mo, assuming the nuclear matrix element $|M^{0\nu\beta\beta}| = 5.850$ [18] and the effective Majorana neutrino mass $|m_{\beta\beta}| = 50$ meV.

$G^{0\nu\beta\beta}$ [y^{-1}]	$G^{0\nu\mathrm{EP}\beta}$ [y^{-1}]	$\Gamma^{0\nu\mathrm{EP}\beta}/\Gamma^{0\nu\beta\beta}$	$T_{1/2}^{0\nu\beta\beta}$ [y]	$T_{1/2}^{0\nu\mathrm{EP}\beta}$ [y]
1.887×10^{-14}	7.400×10^{-20}	3.92×10^{-6}	6.24×10^{25}	1.59×10^{31}

In Table II, we show analogous results for the $2\nu\beta^-\beta^-$ and $2\nu\mathrm{EP}\beta^-$ phase-space factors $G^{2\nu\beta\beta}$ and $G^{2\nu\mathrm{EP}\beta}$, as well as the decay-rate ratio $\Gamma^{2\nu\mathrm{EP}\beta}/\Gamma^{2\nu\beta\beta} = G^{2\nu\mathrm{EP}\beta}/G^{2\nu\beta\beta}$. The $2\nu\beta^-\beta^-$ half-life $T_{1/2}^{2\nu\beta\beta}$ for the $0^+ \longrightarrow 0^+$ ground-state transition of ^{100}Mo has been measured experimentally [3], from which the value of $g_A^2|M^{2\nu\beta\beta}|$ can be deduced regardless of the details of the nuclear-structure theory, and used to predict the $2\nu\mathrm{EP}\beta^-$ half-life $T_{1/2}^{2\nu\mathrm{EP}\beta}$ without any further assumptions; for the unquenched value $g_A = 1.269$ it follows: $|m_e M^{2\nu\beta\beta}| = 0.1194$. We observe that the decay-rate ratio $\Gamma^{2\nu\mathrm{EP}\beta}/\Gamma^{2\nu\beta\beta}$ indicates a relative suppression of the mode $2\nu\mathrm{EP}\beta^-$ to be 1 order of magnitude lower when compared to the neutrinoless case. Moreover, the absolute half-life $T_{1/2}^{2\nu\mathrm{EP}\beta}$ even turns out to fall within the sensitivity of some of the running experiments, which points to somewhat more optimistic prospects for finding the traces of such rare decay in the available double-beta-decay detectors.

Table II. $2\nu\beta^-\beta^-$ and $2\nu\mathrm{EP}\beta^-$ phase-space factors $G^{2\nu\beta\beta}$ and $G^{2\nu\mathrm{EP}\beta}$, decay-rate ratio $\Gamma^{2\nu\mathrm{EP}\beta}/\Gamma^{2\nu\beta\beta} = G^{2\nu\mathrm{EP}\beta}/G^{2\nu\beta\beta}$ and half-lives $T_{1/2}^{2\nu\beta\beta}$ [3] (which implies the nuclear matrix element: $|m_e M^{2\nu\beta\beta}| = 0.1194$) and $T_{1/2}^{2\nu\mathrm{EP}\beta}$ for the isotope ^{100}Mo.

$G^{2\nu\beta\beta}$ [y^{-1}]	$G^{2\nu\mathrm{EP}\beta}$ [y^{-1}]	$\Gamma^{2\nu\mathrm{EP}\beta}/\Gamma^{2\nu\beta\beta}$	$T_{1/2}^{2\nu\beta\beta}$ [y]	$T_{1/2}^{2\nu\mathrm{EP}\beta}$ [y]
3.809×10^{-18}	1.367×10^{-22}	3.59×10^{-5}	7.10×10^{18}	1.98×10^{23}

In Fig. 1, we compare the calculated $0\nu\beta^-\beta^-$ and $0\nu\mathrm{EP}\beta^-$ single-electron spectra. These are represented by differential decay rates $1/\Gamma^{0\nu\beta\beta}\,\mathrm{d}\Gamma/\mathrm{d}E$ (with the former normalized to unity) as functions of the electron kinetic energy $E - m_e$. In particular, we consider the $0^+ \longrightarrow 0^+$ ground-state transition of the isotope ^{100}Mo ($Q = 3.034$ MeV), which had been extensively used in the NEMO 3 experiment [4]. From the obtained phase-space factor $G^{0\nu\mathrm{EP}\beta}$ it follows that the single-electron mode $0\nu\mathrm{EP}\beta^-$ constitutes a sharp peak at the endpoint of the $0\nu\beta^-\beta^-$ single-electron spectrum, i.e., the free electron effectively carries away the entire released kinetic energy Q. For illustration purposes, we present the $0\nu\mathrm{EP}\beta^-$ peak as a Gaussian with $\sigma = 50$ keV (which coincides with the desired energy resolution of SuperNEMO calorimeters [6]) and exaggerate its height by a factor of 10^4. From such disproportion it is clear that the $0\nu\mathrm{EP}\beta^-$ peak will hardly be observed in the forthcoming measurements; nevertheless, the future double-

beta-decay experiments with tracking capability (most notably SuperNEMO) should be able to set limits on the single-electron mode $0\nu\mathrm{EP}\beta^-$ for other isotopes.

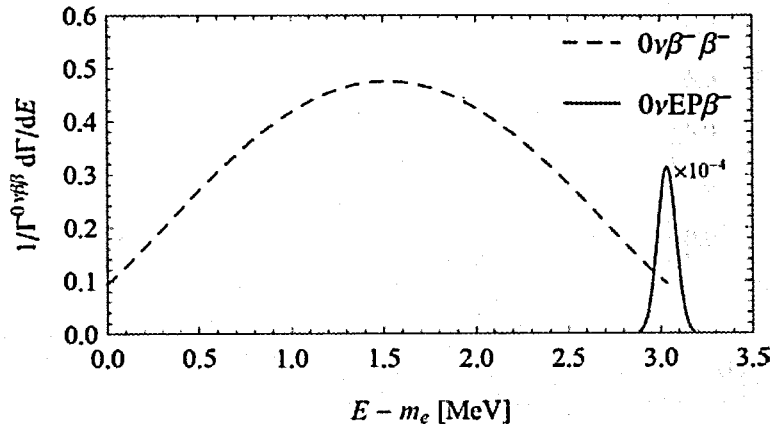

Figure 1. Single-electron $0\nu\beta^-\beta^-$ and $0\nu\mathrm{EP}\beta^-$ spectra $1/\Gamma^{0\nu\beta\beta}\,\mathrm{d}\Gamma/\mathrm{d}E$ (the former normalized to unity) as functions of electron kinetic energy $E - m_e$ for the isotope ^{100}Mo ($Q = 3.034$ MeV). The $0\nu\mathrm{EP}\beta^-$ peak is represented by a Gaussian with $\sigma = 50$ keV and exaggerated by a factor of 10^4.

In Fig. 2, we show the computed single-electron spectra for the $2\nu\beta^-\beta^-$ and $2\nu\mathrm{EP}\beta^-$ modes, defined as the differential decay rates $1/\Gamma\,\mathrm{d}\Gamma/\mathrm{d}E$ normalized to unity, for the $0^+ \longrightarrow 0^+$ ground-state transition of ^{100}Mo ($Q = 3.034$ MeV). We immediately observe that the single-electron mode $2\nu\mathrm{EP}\beta^-$ exhibits a different shape of the spectrum, which should in turn manifest through a slight deformation of the measured $2\nu\beta^-\beta^-$ single-electron spectra. With more than 700,000 positive events coming from approximately 7 kg of enriched ^{100}Mo during 3.49 y of exposure (the low-radon phase) and very high signal-to-background ratio, we suggest that a thorough reassessment of the NEMO 3 data could provide us with valuable insight into the connection between the atomic physics and mechanisms of the double-beta decay [19].

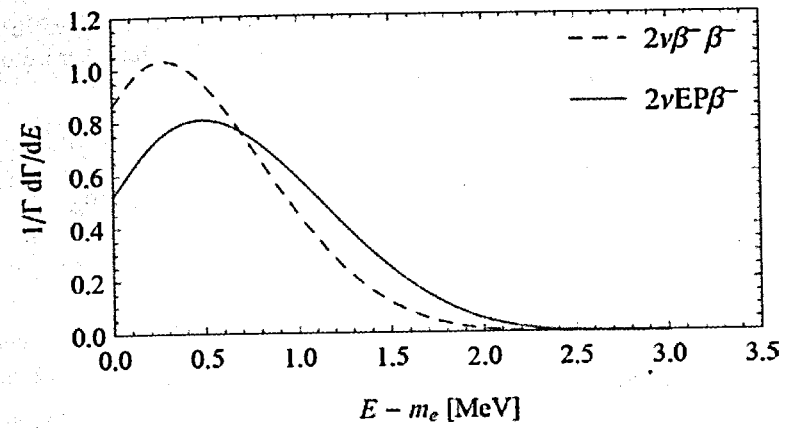

Figure 2. Single-electron $2\nu\beta^-\beta^-$ and $2\nu EP\beta^-$ spectra $1/\Gamma\, d\Gamma/dE$ (normalized to unity) as functions of electron kinetic energy $E - m_e$ for the isotope ^{100}Mo ($Q = 3.034$ MeV).

IV. Conclusion

We have examined new modes of $0\nu\beta^-\beta^-$ and $2\nu\beta^-\beta^-$ in which only one electron is emitted from the atom, the second one being directly produced in the atomic shell of the daughter ion. Such processes would constitute the double-beta-decay counterparts of the bound-state beta decay observed some 25 years ago [5]. We have calculated the phase-space factors, estimated the half-lives and derived the single-electron spectra for the $0^+ \longrightarrow 0^+$ ground-state transition of the isotope ^{100}Mo, which was the primary source used in the NEMO 3 experiment [4, 19]. We conclude that while the $0\nu EP\beta^-$ mode is strongly suppressed and unlikely to be observed in the future experiments, the $2\nu EP\beta^-$ mode could readily contribute to a slight deformation of the measured NEMO 3 data. The forthcoming experiment SuperNEMO will possess all means to set more stringent limits on both single-electron modes $0\nu EP\beta^-$ and $2\nu EP\beta^-$ for the isotope ^{82}Se [6].

Acknowledgments

This work was supported by the VEGA Grant Agency of the Slovak Republic under Contract No. 1/0922/16, the Slovak Research and Development Agency under Contract No. APVV-14-0524, the Ministry of Education, Youth and Sports of the Czech Republic under Contracts No. LM2015072 and LG14003, the Grant Agency of the Czech Technical University in Prague under Contract No. SGS16/261/OHK4/3T/35, the Grant of the Plenipotentiary Representative of the Czech Republic in JINR under Contract No. 189 from 29/03/2016, the RFBR Grant under Contract No. 16-02-01104, and Grant of the Heisenberg–Landau Program under Contract No. HLP-2015-18. M.I.K acknowledges the support of the Alexander von Humboldt Foundation. The authors express their sincere gratitude towards Rastislav Dvornický for enlightening discussions regarding the atomic-structure calculations.

References

[1] J. D. Vergados, H. Ejiri, and F. Šimkovic, Rept. Prog. Phys. **75**, 106301 (2012).
[2] Babič and F. Šimkovic, AIP Conf. Proc. **1572**, 7 (2013).
[3] S. Barabash, Nucl. Phys. A **935**, 52 (2015).
[4] R. Arnold *et al.* (NEMO 3 Collaboration), Phys. Rev. D **92**, 072011 (2015).
[5] M. Jung *et al.*, Phys. Rev. Lett. **69**, 2164 (1992).
[6] R. Arnold *et al.* (SuperNEMO Collaboration), Eur. Phys. J. C **70**, 927 (2010).
[7] S. M. Bilenky and S. T. Petcov, Rev. Mod. Phys. **59**, 671 (1987).
[8] K. A. Olive *et al.* (Particle Data Group), Chin. Phys. C **38**, 090001 (2014).
[9] Gando *et al.* (KamLAND-Zen Collaboration), Phys. Rev. Lett. **117**, 082503 (2016).
[10] J. Kotila and F. Iachello, Phys. Rev. C **85**, 034316 (2012).
[11] M. E. Rose, *Relativistic Electron Theory* (Wiley, 1961).
[12] GRASP2K Relativistic Atomic Structure Package, version 1.1, P. Jönsson, G. Gaigalas, J. Bieroń, C. Froese Fischer, and I. P. Grant, Comput. Phys. Commun. **184**, 2197 (2013).
[13] GRASP2K development version, P. Jönsson *et al.* (The Computational Atomic Structure Group), downloaded from: http://ddwap.mah.se/tsjoek/compas/ (2015).
[14] V. B. Berestetskii, E. M. Lifshitz, and L. P. Pitaevskii, *Quantum Electrodynamics* (Butterworth–Heinemann, 1982).
[15] M. Doi, T. Kotani, and E. Takasugi, Prog. Theor. Phys. Suppl. **83**, 1 (1985).
[16] D. Štefánik, R. Dvornický, F. Šimkovic, and P. Vogel, Phys. Rev. C **92**, 055502 (2015).
[17] V. I. Tretyak and Y. G. Zdesenko, Atom. Data Nucl. Data Tabl. **80**, 83 (2002).
[18] F. Šimkovic, V. Rodin, A. Faessler, and P. Vogel, Phys. Rev. C **87**, 045501 (2013).
[19] S. Barabash and F. Piquemal, Nucl. Phys. News **23**, 12 (2013).

HERA Results on Proton Structure and Hard QCD

Nataša Raičević on behalf of the H1 and ZEUS Collaborations

University of Montenegro, Faculty of Science, 81000 Podgorica, Montenegro

Abstract. We give a report of the relevant results obtained from HERA experiments H1 and ZEUS in the past two years. A short summary of the recently published HERA results on proton structure is given. New results on combined electroweak and QCD fits of inclusive neutral and charged current data with polarised lepton beams from the H1 and ZEUS experiments are discussed. We also show new preliminary results on (multi)jet production studied in neutral current deep-inelastic scattering with low photon virtuality using data taken by the H1 detector. A measurement of the jet cross sections normalized to the neutral current deep-inelastic scattering inclusive cross sections will be presented and compared to next-to-leading order and novel next-to-next-to-leading order predictions in perturbative QCD. We also show new preliminary results from ZEUS on (multi)jet and on prompt photon production studied in neutral current deep-inelastic scattering with low photon virtuality.

E-mail: natasar@ac.me

INTRODUCTION

At the HERA collider a center of mass energy of 318 GeV was achieved by colliding electrons or positrons with energy of 27.5 GeV and protons with energy of 920 GeV. Until the year 2000 (HERA-I period) the experiments H1 and ZEUS at HERA collected an integrated luminosity of about 120 pb^{-1} each. Afterwards HERA underwent a major upgrade aiming for higher luminosity and until 2007 (HERA-II period) HERA provided in total about 500 pb^{-1} of $e^{\pm}p$ collisions to each of the experiments.

In the last three months of HERA operation, special runs with lower proton beam energies of 460 GeV and 575 GeV were performed, each experiment collecting approximately 13 pb^{-1} and 7 pb^{-1} of data respectively. The main purpose of this data was the measurement of the longitudinal proton structure function which is related to the longitudinally polarised virtual boson exchange process.

HERA RESULTS ON PROTON STRUCTURE

Deep Inelastic Scattering (DIS) of leptons on protons is considered as the best tool to examine proton structure via the measurement of Parton Density Functions (PDFs) and their dependence on virtuality of exchanged boson, Q^2, and Bjorken variable, x, which is fraction of proton momentum carried by the stuck quark. Proton structure described by precise PDFs is necessary for making accurate predictions for any process involving protons. DGLAP QCD evolution provides a Q^2 dependence of the PDFs and x PDF dependence must come from data.

To get high precision measurements of PDFs, H1 and ZEUS results are combined into one coherent data set [1]. All together, 41 Neutral Current (NC) and Charged Current (CC) data sets from H1 and ZEUS covering large kinematic plane in Q^2 and x, $0.045 \leq Q^2 \leq 50000$ GeV^2, $6 \cdot 10^{-7} \leq x \leq 0.65$, are combined. The data sets were collected over 15 years giving a total luminosity of 1 fb^{-1} of $e^{\pm}p$ interactions at center of mass energies of: 318, 300, 251 and 225 GeV. Close to 3000 cross sections are combined to about 1300 points with 169 correlated systematic errors and
χ^2/d.o.f. = 1685/1620.

Figure 1 shows individual and combined reduced cross sections for NC e^+p DIS scattering as a function of Q^2 for selected values of Bjorken variable *x*. The improvement due to combination is clearly visible with significant reduction of statistical and systematic errors. The total uncertainty is less than 1.5 % for $Q^2 \leq 500$ GeV^2.

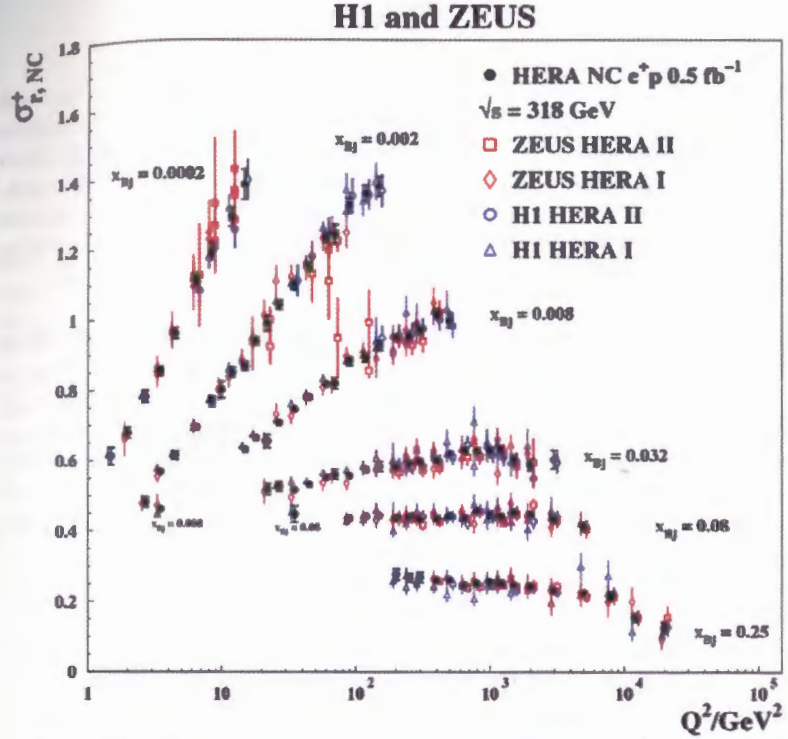

FIGURE 1. Q^2dependence of a selection of combined HERA data for the inclusive NC e^+p reduced cross sections for different values of Bjorken x compared to the individual H1 and ZEUS data. The individual measurements are shifted horizontally for better visibility. Error bars represent the total uncertainties.

The NC reduced cross section is related to the proton structure functions F_2, F_L and xF_3,

$$\sigma_{NC}(e^{\pm}p) = F_2 - \frac{y^2}{1+(1-y)^2} F_L \mp \frac{1-(1-y)^2}{1+(1-y)^2} xF_3,$$

with y being the interaction inelasticity. The structure function F_2 measures the contribution from valence and sea quarks, F_L is directly related to gluon in perturbative QCD and xF_3 measures contribution from valence quarks at high Q^2.

The combined data precisely measure electroweak effects as shown in Figure 2 which displays the cross-sections $d\sigma/dQ^2$ for NC and CC e^-p and e^+p scattering

together with predictions from HERAPDF2.0 NLO, the most recent PDF fit from HERA discussed bellow. At low Q^2, the CC cross section is about two orders of magnitude smaller than the NC cross section due to the γ-exchange contribution, while at high Q^2 they are about the same demonstrating electroweak unification at Q^2 around M_Z^2, M_W^2. Also, e^+p NC and e^-p NC are the same at low Q^2, in the γ-exchange domain, and differ at high Q^2 mainly due to γZ interference. The differences in e^+p and e^-p CC cross sections are related to u, d content of the proton and to the helicity factors $(1-y)^2$,

$$\sigma_{cc}^{e^+p} \sim (x\bar{u} + x\bar{c}) + (1-y)^2 (xd + xs)$$
$$\sigma_{cc}^{e^-p} \sim (xu + xc) + (1-y)^2 (x\bar{d} + x\bar{s}),$$

where xu, xd, xs and xc are u, d,strange and charm quark distributions. All the data are well described by the Standard Model expectations.

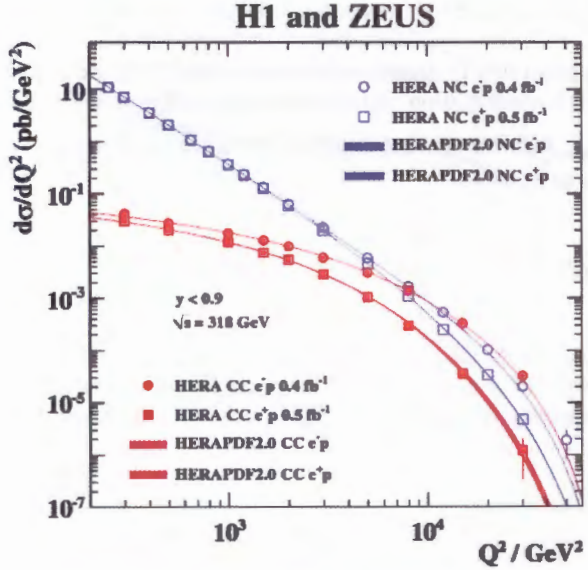

FIGURE 2. Q^2 dependence of the combined HERA NC and CC e^-p and e^+pcross sections, together with predictions from HERAPDF2.0 NLO. The bands represent the total uncertainty on the predictions.

Figure 3 shows the inclusive NC e^+p and e^-p HERA data together with fixed-target data and the predictions of HERAPDF2.0 NLO. There is F_2 scaling at moderate x and precise measurement of scaling violations at low and high Q^2. The cross section rises with Q^2 at low x but drops at high x - at low x due to gluon splitting and at high x due to gluon emission. Also, the electroweak effects are clearly pronounced at high Q^2 due to xF_3 contribution.

The shown data are used in a QCD analysis within the DGLAP formalism for extraction of PDFs. The most recent fit from the combined HERA data is termed as HERAPDF2.0 in which the PDFs are parameterized at a starting scale of $Q_0^2 = 1.9$ GeV^2 and are based on data with Q^2 above $Q^2_{min} = 3.5$ GeV^2.

Figure 4 shows HERAPDF2.0 NLO distributions at $Q^2 = 10$ GeV^2 for the valence distributions for up and down quarks as well as the gluon and sea-quark distributions.The gluon and sea quark (xg and xS) are the dominant parton distributions at low x and are determined with high accuracy due to the high precision of the cross section measurements. As can be seen from the figure, the PDF parameterization uncertainty, resulting from the parameterization choice, dominates the high x region and the valence distributions, while the low x region is dominated by the model uncertainties which are obtained by varying: the charm mass, the bottom mass, the strange fraction, the minimum Q^2 used in the fit and the starting scale Q_0^2. Experimental uncertainties of the fit were determined using the Hessian method with the criterion $\Delta\chi^2 = 1$ (68 % CL).

The resulting parton distribution functions were also obtained at LO and NNLO. Also an extensive investigation included fits with different heavy flavor schemes, different Q^2_{min}, with an alternative gluon parameterization and with a scan of $\alpha_s(M_Z)$ in steps of 0.001.

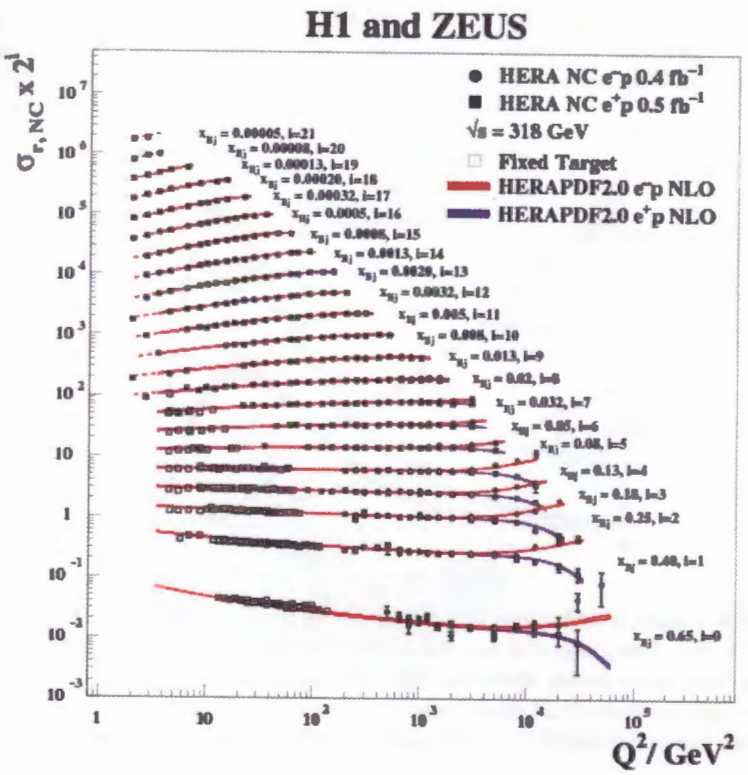

FIGURE 3. Q^2 dependence of combined HERA data for the inclusive NC $e^{\pm}$preduced cross sections for different values of Bjorken x. Fixed-target data and the predictions of HERAPDF2.0 NLO are also shown.

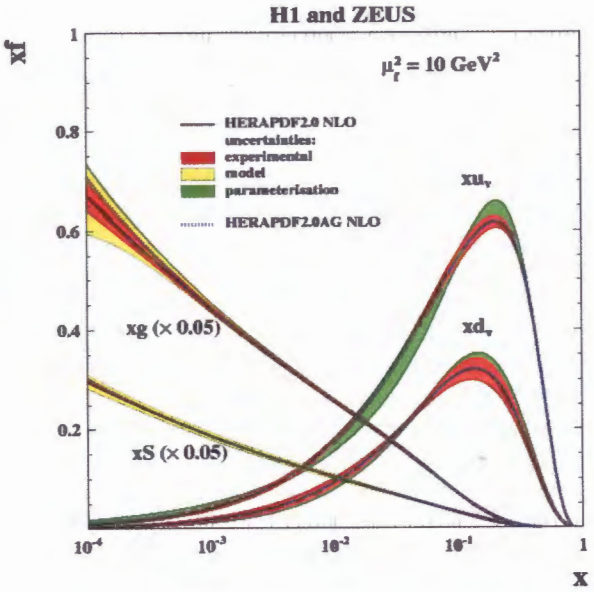

FIGURE 4. Parton distributions as determined by the HERAPDF2.0 QCD fit at $Q^2 = 10$ GeV^2. The gluon and sea-quark densities are scaled down by a factor 0.05. The inner error bands show the experimental uncertainty, the middle error bands include the theoretical model uncertainties of the fit assumptions, and the outer error bands represent the total uncertainty including the parameterization uncertainty.

H1 AND ZEUS COMBINED ELECTROWEAK AND QCD FITS

Using the $e^{\pm}p$ NC and CC cross sections, combined electroweak (EW) and QCD analyses were performed by both collaborations to determine the vector and axial-vector couplings v_q and a_q to the light quarks u and d to the Z^0 boson, accounting for their correlation with PDFs. For this analysis H1 collaboration have used only H1 data [2] and ZEUS used uncombined H1 and ZEUS data of NC and CC cross sections [3]. Preliminary results from H1 and published results from ZEUS for the couplings a_u, v_u and a_d, v_d are shown in figure 5. The figure also shows published results from H1 obtained using only HERA I data [4]. Also shown are Standard Model expectations.

Figure 5 shows that the results from H1 and ZEUS are compatible and also consistent with the SM expectation. There is remarkable sensitivity of HERA data

to u-type quark couplings and there is a considerable improvement over published results of H1 from HERA-I data. Significantly improved sensitivity comes from using polarized HERA-II data and polarization in HERA-II is important in particular for vector couplings.

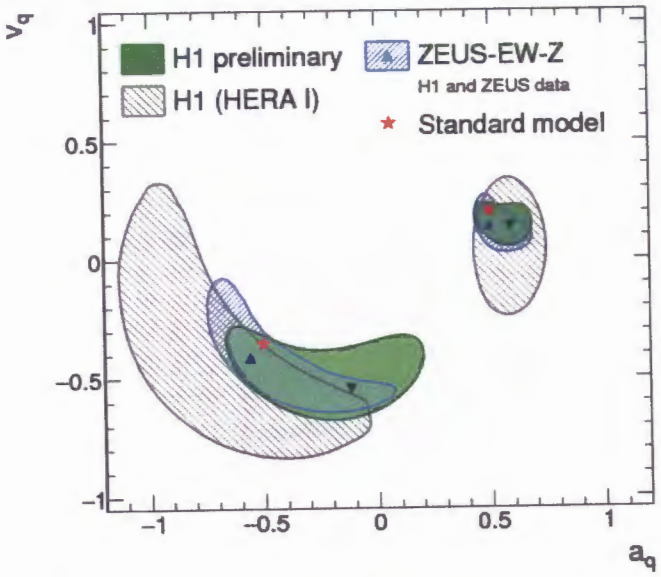

FIGURE 5. The 68% C.L. contours for (ad, vd) - left part of the figure and (au, vu) – right part of the figure, obtained from ZEUS and H1 combined EW+QCD fits. Also shown are published results from HERA-I and the SM values.

Figure 6 shows the results from ZEUS compared to other measurements from LEP, TEVATRON and from H1 based on HERA-I data. The PDG14 values are also shown. HERA results are consistent with other experiments and resolving the LEP sign-ambiguity. HERA results on u-type coupling are highly accurate and present the most precise determination of the axial-vector and vector couplings of the Z boson to u-type quarks.

Both collaborations also extracted the values of M_W and of Weinberg angle, $\sin^2\theta_W$ with combined EW+QCD parameter fits. The value extracted by the ZEUS fit for M_W is

$$M_W = 80.68 \pm 0.28\,(\text{experimental/fit})\,^{+0.12}_{-0.01}(\text{model})\,^{+0.23}_{-0.01}(\text{parameterisation})\ \text{GeV}\ .$$

The on-shell value of $\sin^2\theta_W$ obtained by ZEUS fit was determined as

$$\sin^2\theta_W = 0.2252 \pm 0.0011$$

$$(\text{experimental/fit})^{+0.0003}_{-0.0001}\,(\text{model})^{+0.0007}_{-0.0001}\,(\text{parameterisation}).$$

The values of $\sin^2\theta_W$ and M_W are in agreement with Standard Model expectations.

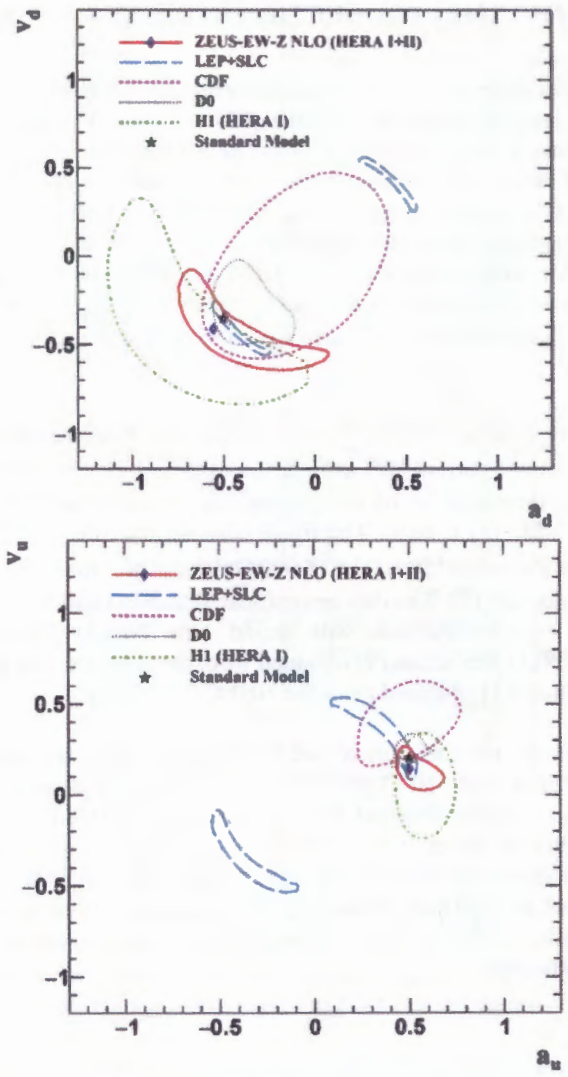

FIGURE 6. The 68% C.L. contours for (a_d, v_d) and (a_u, v_u) obtained from ZEUS combined EW+QCD fit compared with published results from LEP, TEVATRON and from H1 based on HERA-I data. The PDG14 values are also shown.

MULTIJET PRODUCTION IN DIS AT LOW Q^2

The H1 collaboration has a new measurement of jet cross sections in neutral current deep inelastic scattering normalized to the neutral current deep-inelastic scattering inclusive cross sections [5, 6]. The normalized jet cross sections are defined as the ratio of the double differential absolute jet cross sections to the inclusive NC DIS cross section in the respective Q^2 bin. Such normalization provides full cancellation of normalization uncertainties and partial cancellation of other experimental uncertainties. Inclusive jet, dijet and trijet cross sections, absolute and normalized to NC are measured in bins of Q^2 and jet transverse momentum in the Breit frame, P_T^{jet}, with $5.5 < Q^2 < 80$ GeV^2 and $P_T^{jet} > 4.5$ GeV (for inclusive jets).

Figure 7 shows double-differential cross sections for normalized inclusive jet production in neutral current DIS as function of $Q^2$and P_T^{jet}. For the NC DIS cross sections in the denominator of the normalized jet cross sections the program QCDNUM in NLO [7] is used. The figure also shows, new cross sections for $5 < P_T^{jet} < 7$ GeV in the range $150 < Q^2 < 15\,000$ GeV^2 and previously published results in the high Q^2 domain [8]. The data are compared to NLO and NNLO predictions. This is first ever comparison with brand new NNLO QCD calculations, approximate NNLO prediction [9] obtained from the program JetVip [10] and full NNLO prediction [11] obtained from the NNLOJET [11,12].

Figure 8 shows the ratio of normalized inclusive jet cross sections, NNLO and aNNLO predictions to the NLO predictions. The inclusive jet data are reasonably well described by NLO (obtained from the program NLOJET++[13]), but NLO scale uncertainty is rather large. There is an improved description of data (particularly in shape) by NNLO with significantly reduced scale uncertainty for higher values of jet p_T.There is also an improvement of the inclusive jet data description with a NNLO on absolute level at higher values of transverse momentum of the jets.

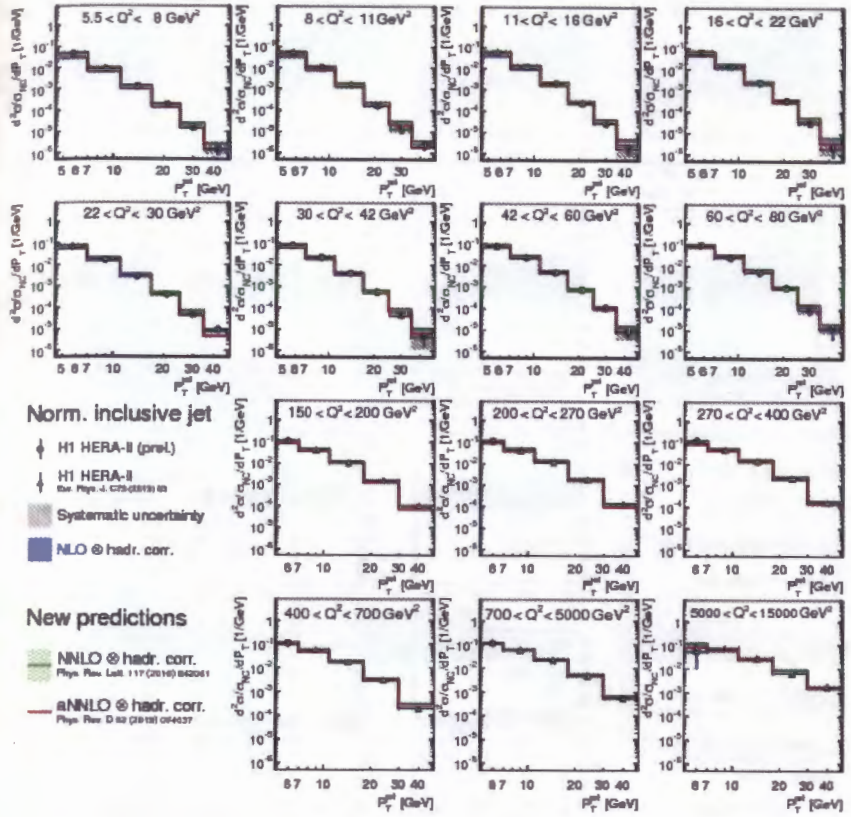

FIGURE 7. Double-differential cross sections for normalized inclusive jet production in neutralcurrent DIS as function of $Q^2$and P_T^{jet}. The vertical error bars indicate the statistical uncertainties.The shaded areas around the data points show the systematic uncertainties. The data are compared to NLO predictions, approximate NNLO and full NNLO predictions.

Normalized dijet and trijet cross sections, where events with at least two or three jets are counted, are obtained as a function of $Q^2$and the average transverse momentum of the two or three leading jets, $\langle P_T \rangle_2$and $\langle P_T \rangle_3$, respectively, in the ranges $5 < \langle P_T \rangle_2 < 50$ GeV and $5.5 < \langle P_T \rangle_3 < 40$ GeV.

Ratio of normalized dijet cross sections and NNLO predictions to NLO predictions shows similar trend as can be seen in figure 9. NNLO predictions for trijets are not available yet.

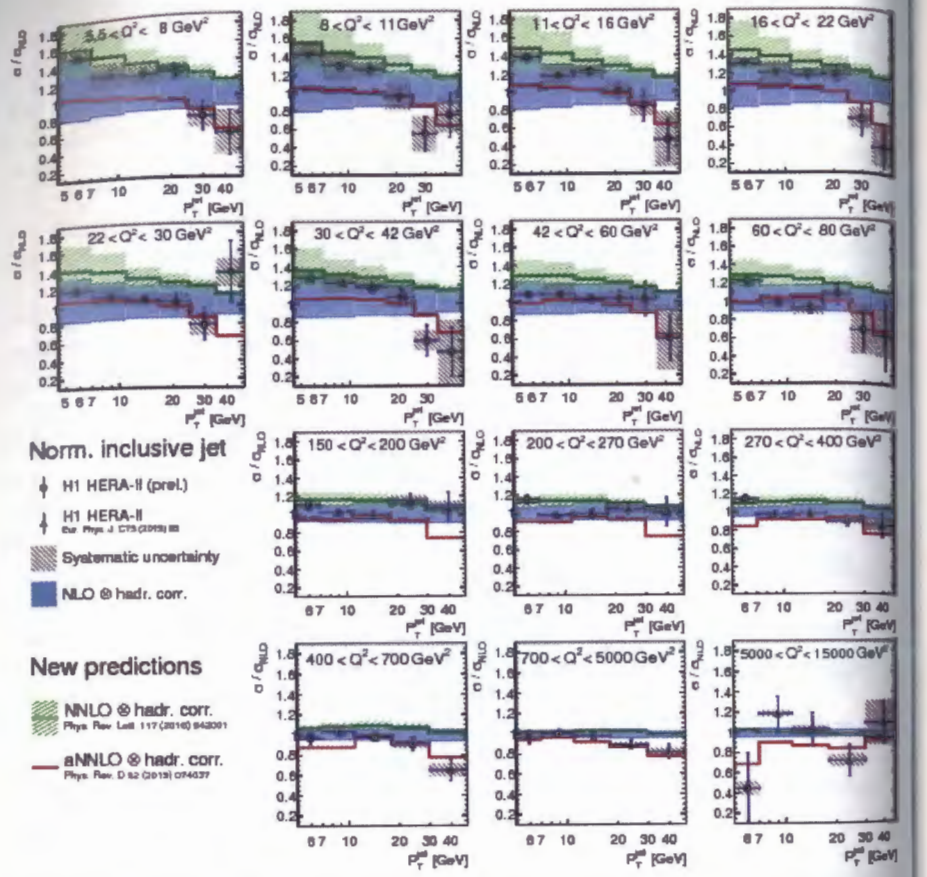

FIGURE 8. Ratio of normalized inclusive jet cross sections, NNLO and aNNLO predictions to the NLO predictions as function of $Q^2$and P_T^{jet}. Other details as in figure 7.

The new normalized multijet data are used for extraction of the strong coupling constant at the Z-boson mass, $\alpha_s(M_Z)$, and also are sensitive to the running of $\alpha_s(\mu_r)$. The behavior of the strong coupling constant is studied in a fit of NLO predictions to data and shown in figure 10. The data for normalized inclusive jet, dijet and trijet production are separated into six groups with similar values of μ_r and the value of $\alpha_s(M_Z)$ is obtained from minimizing χ^2.

The value of $\alpha_s(\mu_r)$ is calculated from $\alpha_s(M_Z)$ by applying the solution for the evolution equation of $\alpha_s(\mu_r)$. The scale uncertainty is obtained by repeating the fits with the different choices for scale factors. The running of the strong coupling

constant is probed by the new data in the range of approximately $5 < \mu_r < 35$ GeV. The uncertainties on the NLO predictions dominate significantly over the experimental uncertainties. Also, data points from the high-Q^2domain may be considered in the fit. A fit to all the data yields an experimental precision on $\alpha_s(M_Z)$ of about 4 permille. Relevant theoretical uncertainties are much higher than the experimental uncertainties mainly due to the scale uncertainties.

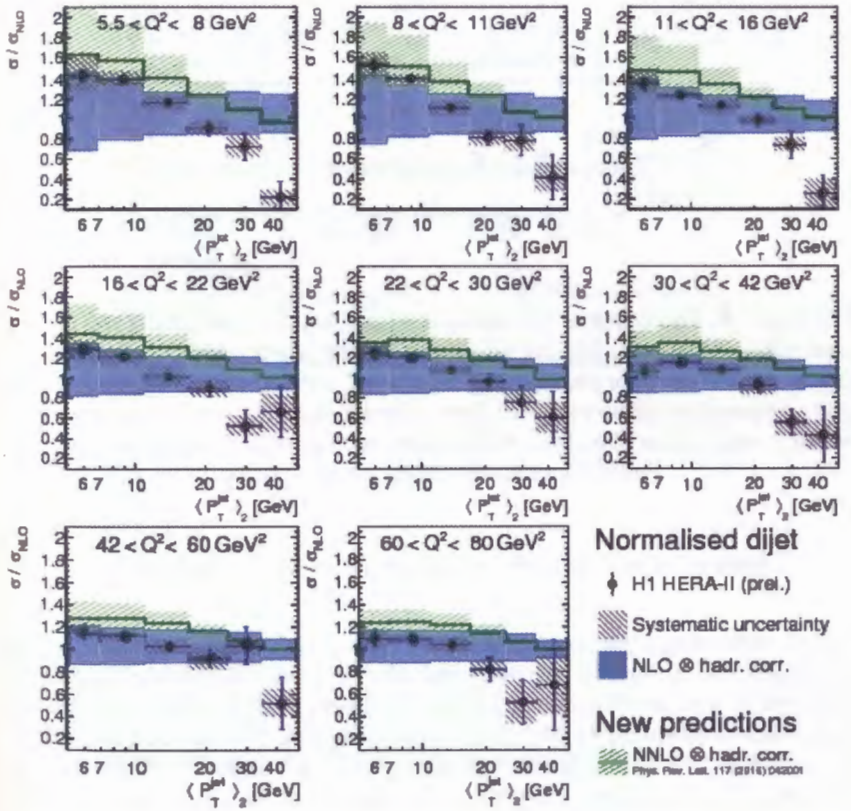

FIGURE 9. Ratio of normalized dijet cross sections and NNLO predictions to NLO predictions as a function of Q^2 and the average transverse momentum of the two leading jets. Other details as in figure 7.

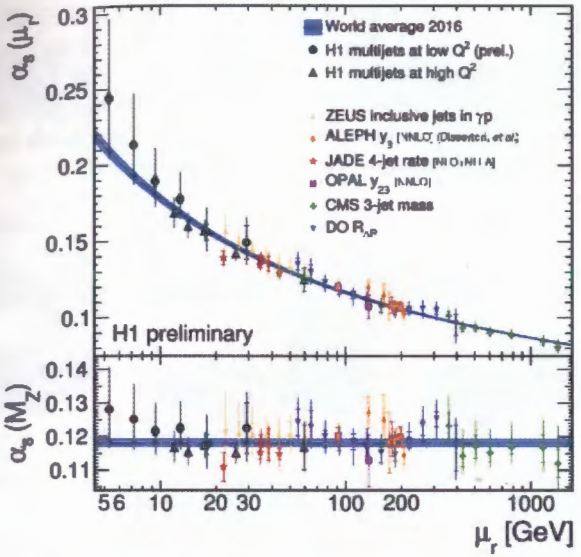

FIGURE 10. The values of the strong coupling $\alpha_s(\mu_r)$ (upper panel) and of the equivalent values of $\alpha_s(M_Z)$ for all measurements (lower panel) obtained from the normalized inclusive jet, dijet and trijet cross sections using NLO predictions and compared to values extracted from other jet data. The solid line shows the world average value of $\alpha_s(M_Z)$ and its value evolved to μ_r using the solution of the QCD renormalization group equation.

ISOLATED PHOTON ACCOMPAINED BY JET IN DIS

Isolated high-energy photons emitted in high-energy collisions can provide information on the proton structure and give a probe of underlying partonic process since they are detected unaffected by parton hadronisation. High energy photons can be produced in DIS either by the incoming or outgoing quark ("QQ" photons) or by the incoming or outgoing lepton ("LL" leptons). QQ photons are classified as "prompt" and LL photons are treated as background to the QCD process. ZEUS obtained new results [14] from analysis of DIS events with the production of an isolated photon and at least one additional jet, ep → e`γ + jet.

Differential cross sections are obtained as functions of the fraction of the incoming photon energy that is given to the photon and the jet, x_γ, fraction of proton energy taken by the parton that interacts with the photon x_p, azimuthal angle between the prompt photon and the jet $\Delta\Phi$, pseudorapidity difference between the prompt photon and the jet $\Delta\eta$, azimuthal angle between the prompt photon and the

scattered electron $\Delta\Phi_{e,\gamma}$ and pseudorapidity difference between the prompt photon and the scattered electron $\Delta\eta_{e,\gamma}$.

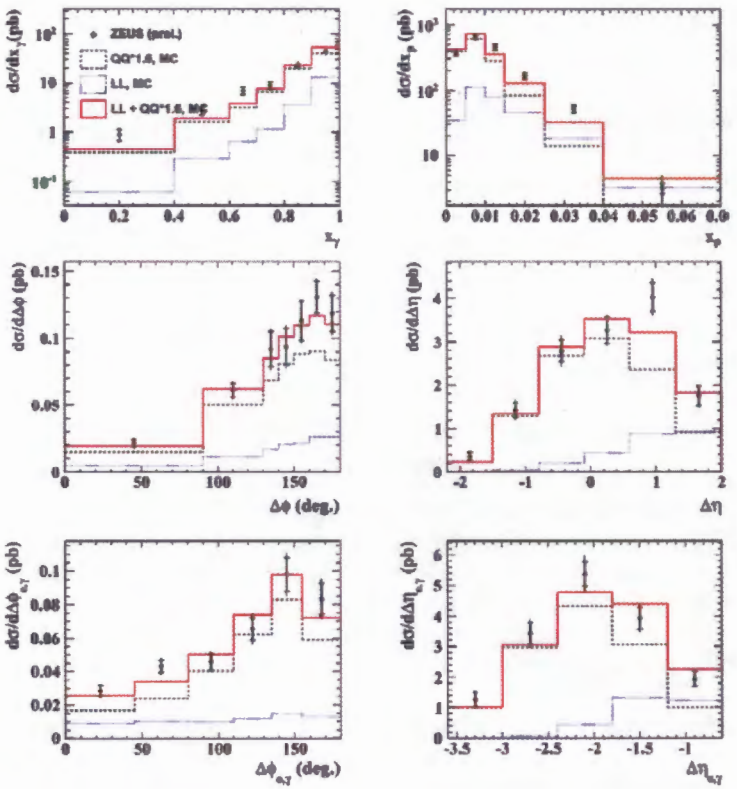

FIGURE 11. Differential cross sections in (a) x_γ, (b) x_p, (c) $\Delta\Phi$, (d) $\Delta\eta$, (e) $\Delta\Phi_{e,\gamma}$, and (f) $\Delta\eta_{e,\gamma}$ compared to the reweighted Monte Carlo predictions from the sum of QQ photons from Pythia normalized by a factor 1.6 plus Djangoh LL photons. The dashed (dotted) lines show the QQ (LL) contributions.

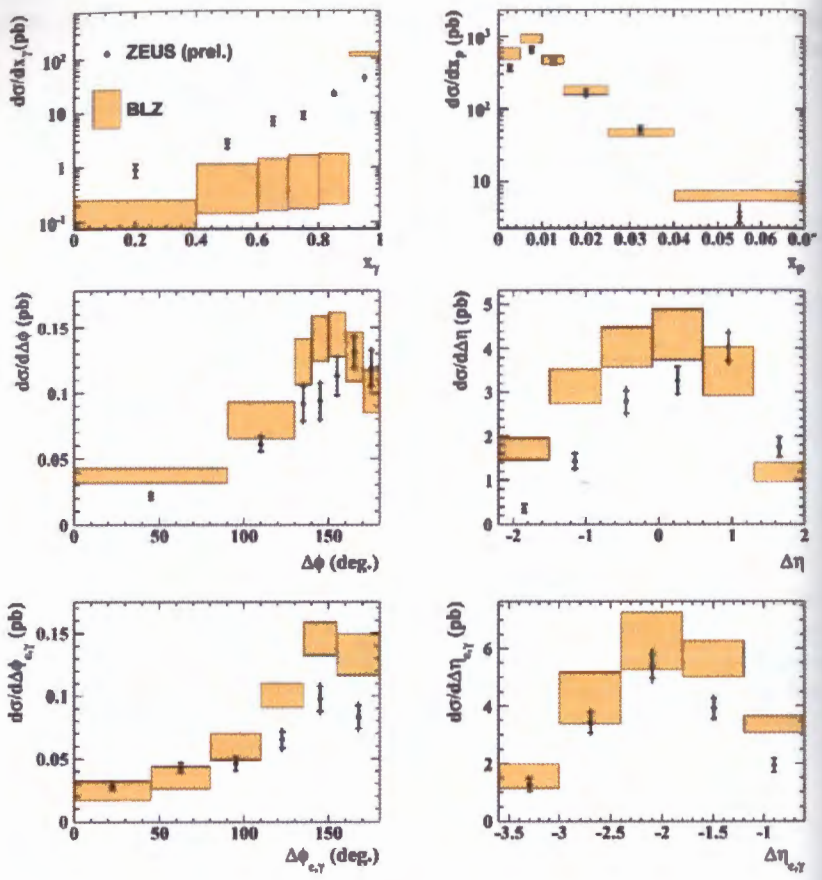

FIGURE 12. Differential cross sections in (a) x_γ, (b) x_p, (c) $\Delta\Phi$, (d) $\Delta\eta$, (e) $\Delta\Phi_{e,\gamma}$, and (f) $\Delta\eta_{e,\gamma}$ compared to the BLZ model based on the k_T factorization.

Figure 11 shows that the resulting cross sections agree well with the theory calculations based on the predictions for the sum of the expected LL contribution from Djangoh [15] and a factor of 1.6 times the expected QQ contribution from Pythia [16] without further weighting.

Figure 12 shows the resulting cross sections compared to the theory calculations based on the k_T factorisation method used by BLZ (Baranov, Lipatov, Zotov) model [17]. This approach takes into account both QQ and LL photons, neglecting the small interference contribution (LQ). In the k_T factorisation theory some part of final state jets can originate not only from hard subprocess, but also from the

parton evolution cascade in initial state. As can be seen, x_γ and $\Delta\eta$ distributions are not described by k_T-factorization.

SUMMARY

HERA experiments, H1 and ZEUS, have finalized measurements of inclusive NC and CC DIS cross sections and QCD fits. H1 and ZEUS have combined all inclusive measurements into one coherent data set for e^+p and e^-p collisions at $\sqrt{s}$ = 318, 300, 251 and 225 GeV. The combined inclusive HERA data are used as a sole input to the QCD analysis resulting in the set of parton distribution functions HERAPDF2.0.

Both collaborations have performed new combined EW and QCD fits providing high precision measurements of electroweak parameters. The data show high sensitivity to light quark couplings and the SM parameters. The fits provide important complementary tests of the SM.

Concerning the hard QCD domain, inclusive jets, dijets, trijets cross sections as well as those normalized to inclusive NC cross section are now available for the whole Q^2 range, based on H1 data. The data provide first ever comparisons with brand new NNLO QCD calculations presented for some of these normalized jet cross sections; the scale uncertainty is visibly reduced and the shape is better described compared to NLO. The experimental precision of α_s determination based on these data is now ~0.4% and is significantly better than theory uncertainty.
The production of isolated photons accompanied by jets has been measured in deep inelastic scattering with the ZEUS detector. The results are in agreement with Pythia after a rescaling has been applied and can be used to make further improvements in the QCD calculations.

REFERENCES

1. H1 and ZEUS Collaborations, Eur. Phys. J. C75, 580 (2015).
2. H1 Collaboration, H1prelim-16-041, (2016).
3. ZEUS Collaboration, Phys.Rev. D 93, 092002(2016).
4. H1 Collaboration, Phys.Lett.B 632, 35 (2006).
5. H1 Collaboration, H1prelim-16-061, (2016).
6. H1 Collaboration, H1prelim-16-062, (2016).
7. M. Botje, Comput. Phys. Commun. 182, 490 (2011).
8. H1 Collaboration, Eur. Phys. J. C75, 65 (2015).
9. T. Biekötter, M. Klasen and G. Kramer, Phys. Rev. D92 7, 074037 (2015).

10. B. Pötter, Comput. Phys. Commun. 133, 105 (2000).
11. J. Currie, T. Gehrmann and J. Niehues, Phys. Rev. Lett. 117, 042001 (2016).
12. A. Gehrmann-De Ridder, T. Gehrmann, E.W.N. Glover, A. Huss and T.A. Morgan, JHEP 1607, 133 (2016).
13. Z. Nagy and Z. Trocsanyi, Phys. Rev. Lett. 87, 082001 (2001).
14. ZEUS Collaboration, ZEUS-prel-16-001, (2016).
15. K. Charchula, G. A. Schuler, and H. Spiesberger, Comput. Phys. Commun. **81**, 381 (1994).
16. T. Sjöstrand et al., JHEP 0605, 26 (2006).
17. S. Baranov, A. Lipatov and N. Zotov, Phys. Rev. D 81, 094034 (2010).

Searches for lepton number violation and resonances in the $K^{\pm} \to \pi\mu\mu$ decays at the NA48/2 experiment

D.Madigozhin [1]

Joint Institute for Nuclear Research, Dubna, Russia,

e-mail: madigo@mail.cern.ch

[1] for the NA48/2 Collaboration: G. Anzivino, R. Arcidiacono, W. Baldini, S. Balev, J.R. Batley, M. Behler, S. Bifani, C. Biino, A. Bizzeti, B. Bloch-Devaux, G. Bocquet, N. Cabibbo, M. Calvetti, N. Cartiglia, A. Ceccucci, P. Cenci, C. Cerri, C. Cheshkov, J.B. Chèze, M. Clemencic, G. Collazuol, F. Costantini, A. Cotta Ramusino, D. Coward, D. Cundy, A. Dabrowski, P. Dalpiaz, C. Damiani, M. De Beer, J. Derré, H. Dibon, L. DiLella, N. Doble, K. Eppard, V. Falaleev, R. Fantechi, M. Fidecaro, L. Fiorini, M. Fiorini, T. Fonseca Martin, P.L. Frabetti, L. Gatignon, E. Gersabeck, A. Gianoli, S. Giudici, A. Gonidec, E. Goudzovski, S. Goy Lopez, M. Holder, P. Hristov, E. Iacopini, E. Imbergamo, M. Jeitler, G. Kalmus, V. Kekelidze, K. Kleinknecht, V. Kozhuharov, W. Kubischta, G. Lamanna, C. Lazzeroni, M. Lenti, L. Litov, D. Madigozhin, A. Maier, I. Mannelli, F. Marchetto, G. Marel, M. Markytan, P. Marouelli, M. Martini, L. Masetti, K. Massri, E. Mazzucato, A. Michetti, I. Mikulec, N. Molokanova, E. Monnier, U. Moosbrugger, C. Morales Morales, D.J. Munday, A. Nappi, G. Neuhofer, A. Norton, M. Patel, M. Pepe, A. Peters, F. Petrucci, M.C. Petrucci, B. Peyaud, M. Piccini, G. Pierazzini, I. Polenkevich, Yu. Potrebenikov, M. Raggi, B. Renk, P. Rubin, G. Ruggiero, M. Savrié, M. Scarpa, M. Shieh, M.W. Slater, M. Sozzi, S. Stoynev, E. Swallow, M. Szleper, M. Valdata-Nappi, B. Vallage, M. Velasco, M. Veltri, S. Venditti, M. Wache, H. Wahl, A. Walker, R. Wanke, L. Widhalm, A. Winhart, R. Winston, M.D. Wood, S.A. Wotton, A. Zinchenko, M. Ziolkowski.

Abstract

The NA48/2 experiment at CERN collected a large sample of charged kaon decays into final states with multiple charged particles in 2003-2004. A new upper limit on the rate of the lepton number violating decay $K^{\pm}\to p^{\mp}m^{\pm}m^{\pm}$ obtained from this sample is set: 8.6×10^{-11} at 90% CL, which improves by more than an order of magnitude upon the previous measurements. Results of the search for two-body resonances like heavy neutral leptons and inflatons in $K^{\pm}\to pmm$ decays are also presented.

1 Introduction

The important consequence of the neutrino oscillations discovery is the existence of neutrino masses and right-handed neutrino states [1]. In the Neutrino Minimal Standard Model (nMSM) [2] three right-handed sterile neutrinos are proposed in order to explain simultaneously neutrino oscillations and the baryon asymmetry of the observed Universe. The first of these right-handed neutrinos has a mass of O(1 KeV) and is a dark matter candidate. The other two neutrinos have masses in the range of (0.1-10) GeV/c^2 and may induce the barion asymmetry by means of additional CP violating phases.

The (nMSM) model can be extended by adding of the scalar field called inflaton which helps to explain the inflation and provides a common source of the electroweak symmetry breaking and the right-handed neutrino masses [3].

These models predict new particles – heavy Majorana neutrinos and inflatons, that can be detected in $K^{\pm}\to pmm$ decays. In particular the decay mode $K^{\pm}\to p^{\mp}m^{\pm}m^{\pm}$ is a Lepton Number Violating (LNV) one. It is forbidden in SM, but it can proceed via the on-shell Majorana neutrino. Inflatons c can be produced in the $K^{\pm}\to p^{\pm}c$ decay, and then they may be detected via $c\to m^{+}m^{-}$ process as a peak in the mm invariant mass spectrum.

The main goal of NA48/2 experiment was the search for CP-violating asymmetry in $K^{\pm}\to 3p$ decays [4]. Additionally, it has provided in 2003-2004 a large data sample for charged kaon rare decay studies, including the search for LNV kaon decays and a possible two-body sharp resonanses in the mass spectra of mm and pm final states. Results of this search are briefly reported in the present work and are published in details in [5].

2 The NA48/2 beam and detector

The NA48/2 detector and beam at CERN SPS are described in details in [4, 6]. Two simultaneous and collinear K^{+} and K^{-} beams were produced by 400 GeV/c protons on a beryllium target. Particles of opposite charge with a central momentum of 60 GeV/c and a momentum band of ±3.8%(RMS) were selected by the system of magnets and collimators. Both beams of about 1 cm width were

following almost the same path in the decay volume contained in a 114 m long vacuum tank. The downstream end of the tank was sealed by a convex Kevlar window separating vacuum from helium at atmospheric pressure. The beams were dominated by $p^{\pm}$, the kaon component was about 6%.

Charged products of $K^{\pm}$ decays were measured by the magnetic spectrometer installed in helium. It was consisting of four drift chambers (DCH1–DCH4) and a dipole magnet providing a horisontal momentum kick of about 120 MeV/c, that was located between DCH2 and DCH3. The spatial resolution of each chamber was nearly 90 mm and the spectrometer momentum resolution was $s_p/p = (1.02 \oplus 0.044\ p)\%$ (p in Gev/c).

The spectrometer was followed by a scintillator hodoscope HOD with a time resolution of 150 ps, whose fast signals were used to trigger the readout of events with a charged track. It consisted of a horizontal and a vertical planes of strip-shaped counters.

A Liquid Krypton calorimeter (LKr), located behind the hodoscope, was used to measure the energy of electrons and photons. It is an almost homogeneous ionization chamber with an active volume of 7 m^3 of liquid krypton $27X_0$ deep, segmented transversally into projective cells, 2x2 cm^2 each. Transverse position of isolated shower was measured with a spatial resolution $s_X=s_Y=(0.42/\sqrt{E} \oplus 0.06)$ cm. Energy resolution for photons and electrons was $s_E/E = (3.2/\sqrt{E} \oplus 9.0/E \oplus 0.42)\%$ (E in GeV), and a single shower time resolution was $s_t = (2.5/\sqrt{E})$ ns.

The muon system MUV, consisted of three scintillator planes (MUV1,MUV2,MUV3) and 80 cm thick iron walls, was used for the muons identification. An aluminium beam pipe of 16 cm outer diameter and 1.1 mm thickness was traversing the centres of all the detector elements, providing the path in vacuum for undecayed beam particles and for muons from beam $p^{\pm}$ decays.

3 Events selection

Event selection is based on the three-track vertex reconstruction, as for the experimental longitudinal position resolution of about 50 cm, both $K^{\pm}\to p^{\mp}m^{\pm}m^{\pm}$ (LNV) and $K^{\pm}\to p^{\pm}m^{+}m^{-}$ (LNC) decays mediated by a short-lived resonant particle are indistinguishable from a three-track decay. $K^{\pm}\to p^{\pm}p^{+}p^{-}$ (K_{3p}) decays were used as a normalization channel. The corresponding samples were collected concurrently using the same trigger logic.

In order to select K_{pmm} or K_{3p} candidate, a vertex satisfying the following common criteria was required: the total charge of the three tracks is ±1; the vertex longitudinal position is within the 98 m long fiducial decay volume; the vertex tracks momentum is between 5 GeV/c and 55 GeV/c; the total momentum of three tracks is consistent with the beam nominal range (55-65) GeV/c; and the total

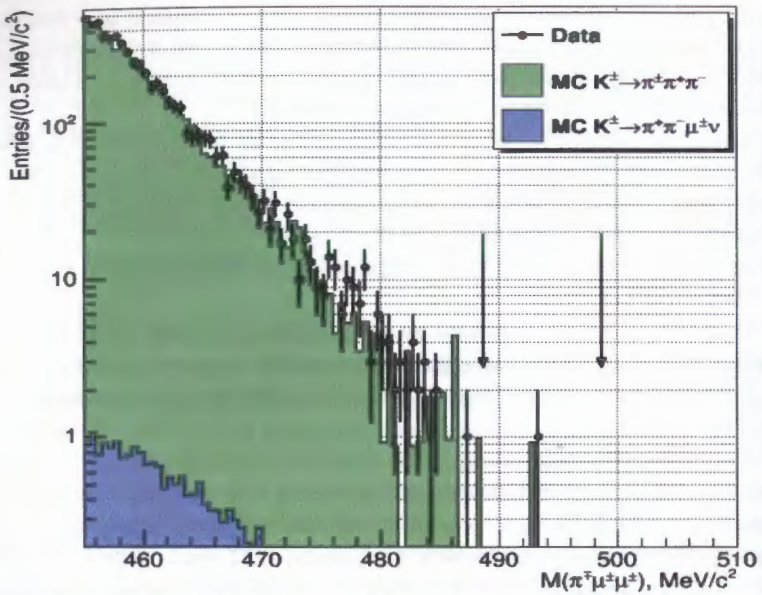

transverse momentum of three tracks with respect to the beam axis is below 0.01 GeV/c.

Figure 1: Lepton number violating $K^{\pm}\to p^{\mp}m^{\pm}m^{\pm}$ decay invariant mass spectrum for data and MC. The signal region is indicated with vertical arrows.

The vertex with a lowest fit c^2 is considered in the case of a few selected combinations. The vertex tracks are required to be consistent in time and to be in DCH, HOD, LKr and MUV geometric acceptances. Track separations are required to exceed 2 cm in the DCH1 plane to suppress photon conversions, and 20 cm in the LKr, MUV1 and MUV2 front planes to minimize particle misidentification due to shower overlaps and Coulomb scattering.

The $K^{\pm}\to$pmm candidate vertex must be composed of one pion candidate (with the ratio of energy E in the LKr calorimeter to momentum p measured in the spectrometer $E/p < 0.95$, and without in-time associated hits in the MUV), and a pair of identically or oppositely charged muon candidates (with $E/p < 0.2$ and with the associated hits in MUV).

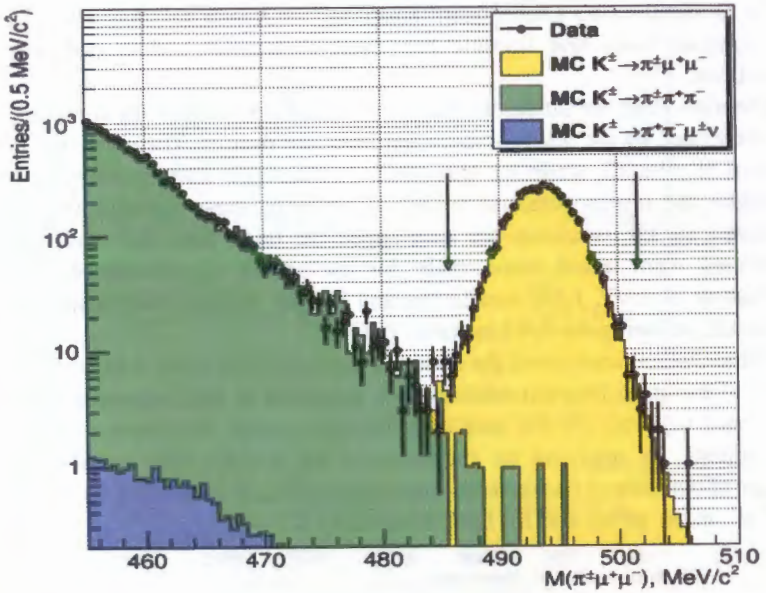

Figure 2: Lepton number conserving $K^{\pm}\to p^{\pm}m^{+}m^{-}$ decay invariant mass spectrum for data and MC. The signal region is indicated with vertical arrows.

The pion candidate is required to have momentum above 15 GeV/c for high muon rejection efficiency. The invariant mass of three tracks in the $K^{\pm}\to$pmm hypothesis must satisfy the requirement of $|M(p^{\mp}m^{\pm}m^{\pm})-M_K| < 5$ MeV/c^2 ($|M(p^{\pm}m^{+}m^{-})-M_K| < 8$ MeV/c^2), where M_K is the PDG kaon mass [1]. The invariant mass distributions for LNV and LNC decay modes are shown in Fig. 1 and Fig. 2.

An additional requirement is applied to the $K^{\pm}\to$pmm samples, when searching for resonances: $|M_{ij} - M_X| < 2s(M_{ij})$, where M_{ij} is the invariant mass of the pair ($ij = p^{\pm}m^{\mp}$ or $m^{+}m^{-}$), M_X is the assumed resonance mass, and $s(M_{ij})$ is the resolution on the invariant masses.

Independently, the following criteria are applied to select the K_{3p} sample: the pion identification criterion is applied to the odd-sign pion only in order to symmetrize the selection of the signal and normalisation modes, and the invariant mass of three tracks in the $3p^{\pm}$ hypothesis is in the range $|M_{3p} - M_K| < 5$ MeV/c^2.

4 Resonance searches

A search for peaks was performed over the distributions of the invariant masses of $p^{\pm}m^{\mp}$ and $m^{+}m^{-}$ pairs. The precise evaluation of acceptance for $K^{\pm}\to m^{\pm}X$ and

$K^{\pm} \to p^{\pm} X$ decays with a subsequent $X \to p^{\pm} m^{\mp}$ or $X \to m^{+} m^{-}$ decay as a function of resonance mass and lifetime has been performed with a dedicated MC simulations.

The mass steps for the resonance searches and the width of the signal window are determined by the resolutions on the invariant masses. The mass step is set to be equal to $s(M_{ij})/2$, while the half-width of the signal mass window is $2s(M_{ij})$. Therefore, the results obtained in the neighbouring mass hypotheses are highly correlated, as the windows are overlapped. In total, 284, 267 and 280 mass hypotheses were tested respectively for the search of resonances in M(pm) distribution of LNV, LNC candidates and in the M(mm) distribution of LNC candidates, covering the full kinematic ranges.

The statistical analysis of the obtained results in each mass window is done by means of the quasi-Newton minimisation algorithm to find numerically the 90% confidence intervals for the case of a Poisson process in presence of unknown backgrounds, by applying an extension of the Rolke-Lopez method [7]. The number of considered background sources for LNV mode was 4 ($3p^{\pm}$, $p^{+}p^{-}m^{\pm}n$, $p^{\pm}m^{+}m^{-}$, $m^{+}m^{-}m^{\pm}n$), and for LNC it was only $K^{\pm} \to 3p^{\pm}$.

5 Results

Only one LNV event is observed, while the estimated background expectation was $1.163 \pm 0.867_{stat} \pm 0.021_{ext} \pm 0.116_{syst}$. So no signal evidence is observed, and a 90% upper limit on the branching ratio $B(K^{\pm} \to p^{\mp} m^{\pm} m^{\pm})$ is set applying the statistical analysis. Using the values of the signal acceptance estimated with MC simulations and the N_{LNV} number of kaon decays in the fiducial volume, the upper limit on the number of signal events leads to a constraint on the signal branching ratio:

$$B(K^{\pm} \to p^{\mp} m^{\pm} m^{\pm}) = B(K_{3p})\, N_{LNV}\, A(K_{3p}) / [N_{3p}\, A(LNV)] < 8.6 \times 10^{-11} \text{ at 90\% CL}$$

The total systematic uncertainty on the quoted upper limit is 1.5%. he largest source is the limited accuracy of the MC simulations (1.0%), followed by the external errors from PDG values of $B(K^{\pm} \to p^{\pm} m^{+} m^{-})$ (0.8%), $B(K_{3p})$(0.73%) and $B(K^{\pm} \to p^{+} p^{-} m^{\pm} n)$ (0.05%).

For each of the three resonance searches a local significance z of the signal has been evaluated for each mass hypothesis: $z = (N_{obs} - N_{exp}) / \sqrt{(dN^2_{obs} + dN^2_{exp})}$, where N_{obs} is the number of observed events, N_{exp} is the number of expected background events, and dN_{obs} (dN_{exp}) is the statistical uncertainty for N_{obs} (N_{exp}). The local significance never exceed 3 standard deviations, therefore no signal is observed.

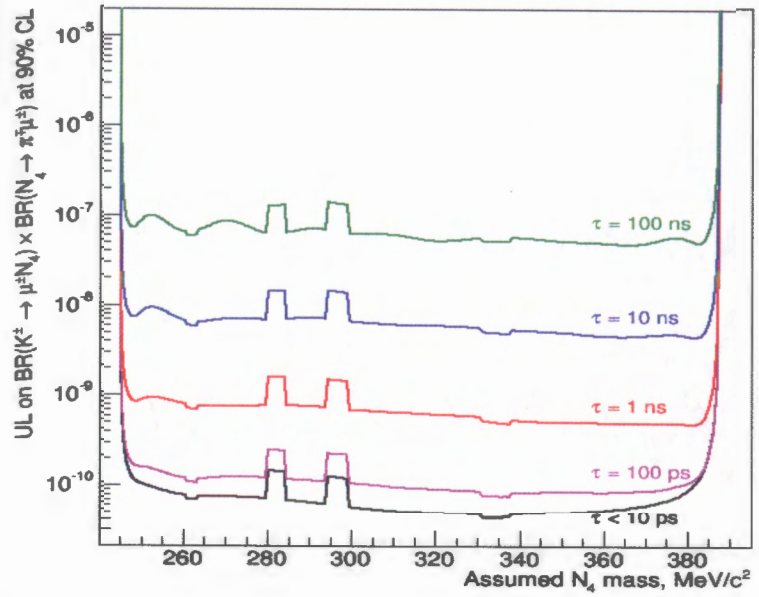

Figure 3: Obtained upper limits at 90% CL on $B(K^{\pm} \to m^{\pm} N_4) B(N_4 \to p^{\mp} m^{\pm})$

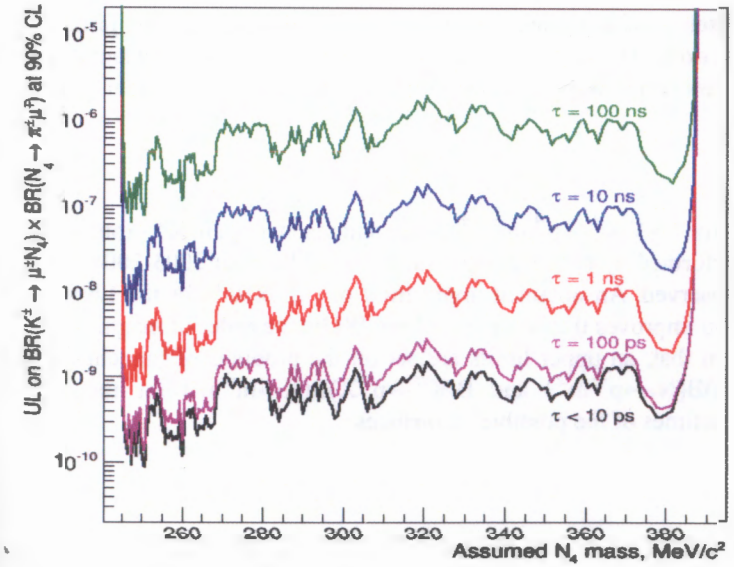

Figure 4: Obtained upper limits at 90% CL on $B(K^{\pm} \to m^{\pm} N_4) B(N_4 \to p^{\pm} m^{\mp})$

$K^{\pm} \to p^{\pm} X$ decays with a subsequent $X \to p^{\pm} m^{\mp}$ or $X \to m^{+} m^{-}$ decay as a functi of resonance mass and lifetime has been performed with a dedicated MC simulations.

The mass steps for the resonance searches and the width of the signal windo are determined by the resolutions on the invariant masses. The mass step is set to be equal to $s(M_{ij})/2$, while the half-width of the signal mass window is $2s(M_{ij})$. Therefore, the results obtained in the neighbouring mass hypotheses are highly correlated, as the windows are overlapped. In total, 284, 267 and 280 mass hypotheses were tested respectively for the search of resonances in M(pm) distribution of LNV, LNC candidates and in the M(mm) distribution of LNC candidates, covering the full kinematic ranges.

The statistical analysis of the obtained results in each mass window is done by means of the quasi-Newton minimisation algorithm to find numerically the 90% confidence intervals for the case of a Poisson process in presence of unknow backgrounds, by applying an extension of the Rolke-Lopez method [7]. The number of considered background sources for LNV mode was 4 ($3p^{\pm}$, $p^{+}p^{-}m^{\pm}n$, $p^{\pm}m^{+}m^{-}$, $m^{+}m^{-}m^{\pm}n$), and for LNC it was only $K^{\pm} \to 3p^{\pm}$.

5 Results

Only one LNV event is observed, while the estimated background expectation was $1.163 \pm 0.867_{stat} \pm 0.021_{ext} \pm 0.116_{syst}$. So no signal evidence is observed, and a 90% upper limit on the branching ratio $B(K^{\pm} \to p^{\mp} m^{\pm} m^{\pm})$ is set applying the statistical analysis. Using the values of the signal acceptance estimated with MC simulation and the N_{LNV} number of kaon decays in the fiducial volume, the upper limit on the number of signal events leads to a constraint on the signal branching ratio:

$$B(K^{\pm} \to p^{\mp} m^{\pm} m^{\pm}) = B(K_{3p})\, N_{LNV}\, A(K_{3p}) / [N_{3p}\, A(LNV)] < 8.6 \times 10^{-11} \text{ at 90\% CL.}$$

The total systematic uncertainty on the quoted upper limit is 1.5%. he largest source is the limited accuracy of the MC simulations (1.0%), followed by the external errors from PDG values of $B(K^{\pm} \to p^{\pm} m^{+} m^{-})$ (0.8%), $B(K_{3p})$(0.73%) and $B(K^{\pm} \to p^{+} p^{-} m^{\pm} n)$ (0.05%).

For each of the three resonance searches a local significance z of the signal has been evaluated for each mass hypothesis: $z = (N_{obs} - N_{exp}) / \sqrt{(dN^2_{obs} + dN^2_{exp})}$, where N_{obs} is the number of observed events, N_{exp} is the number of expecte background events, and dN_{obs} (dN_{exp}) is the statistical uncertainty for N_{obs} (N_{exp}). The local significance never exceed 3 standard deviations, therefore no signal is observed.

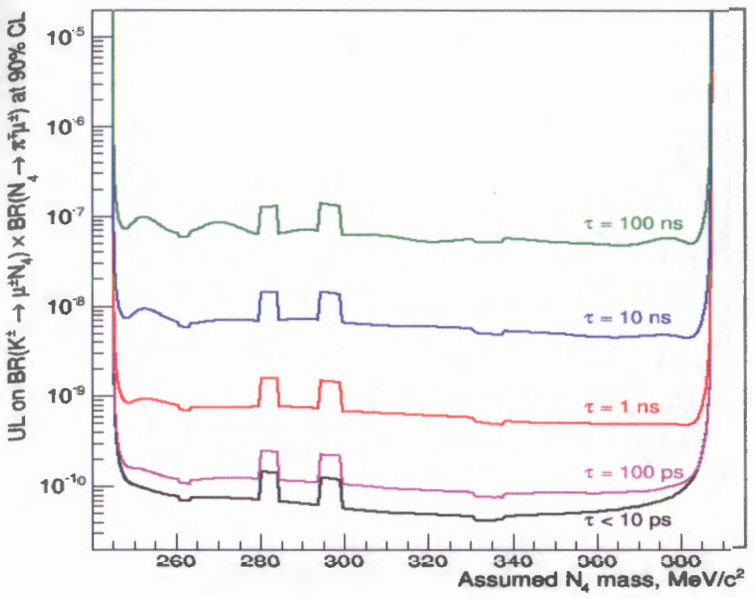

Figure 3: Obtained upper limits at 90% CL on $B(K^{\pm} \to m^{\pm} N_4) B(N_4 \to p^{\mp} m^{\pm})$

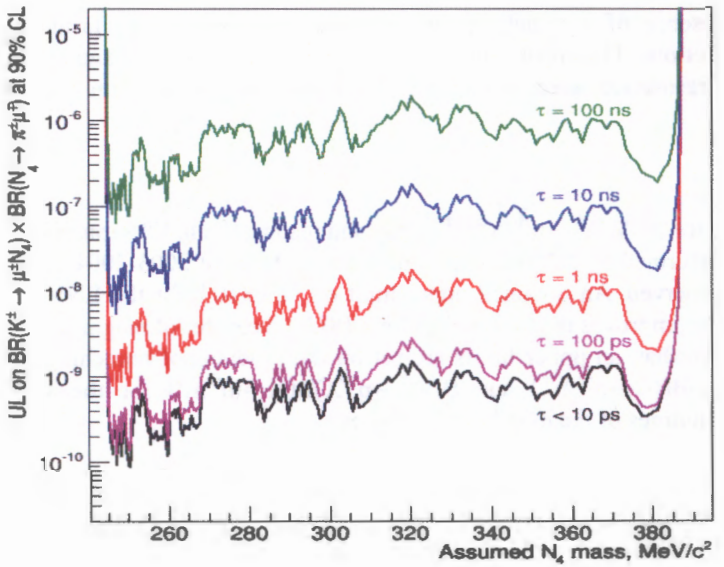

Figure 4: Obtained upper limits at 90% CL on $B(K^{\pm} \to m^{\pm} N_4) B(N_4 \to p^{\pm} m^{\mp})$

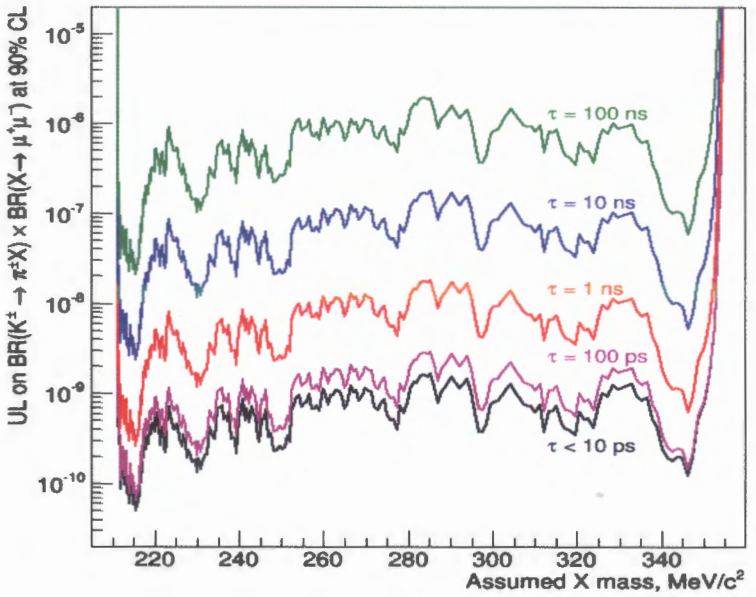

Figure 5: Obtained upper limits at 90% CL on $B(K^{\pm}\to p^{\pm}c)B(c\to m^{+}m^{-})$

In the absence of a signal, upper limits has been set on the products of branching fractions. The upper limits corresponding to the observed signal events for the three resonance searches for several lifetimes are presented on Figures 3, 4, 5.

Conclusion

The searches for LNV $K^{\pm}\to p^{\mp}m^{\pm}m^{\pm}$ decay and resonances in $K^{\pm}\to pmm$ decays have been performed by NA48/2 experiment on the basis of 2003-2004 data. No signals are observed. An obtained upper limit of 8.6×10^{-11} for the LNV decay branching ratio improves the best earlier limit [8] by the order of magnitude.

Apart from that, an upper limits are set on the products of branching ratios $B(K^{\pm}\to m^{\pm}N_4)B(N_4\to p^{\mp}m^{\pm})$ and $B(K^{\pm}\to p^{\pm}X)B(X\to m^{+}m^{-})$ for the various masses and lifetimes of the possible resonances.

References

[1] Particle Data Group, K. Olive *et al.*, Chin. Phys. C **38** (2014) 090001.
[2] T. Asaka and M. Shaposhnikov. Phys. Lett. B **620** (2005) 17.

[3] M. Shaposhnikov and I. Tkachev. Phys. Lett. B **639** (2006) 414 .
[4] J.R.Batley, *et al.*, Eur. Phys. J. C **52** (2007) 875.
[5] J.R.Batley, *et al.*, Phys. Lett. B **769** (2017) 67.
[6] V. Fanti, *et al.*, Nucl.Instrum.Meth. A **574** (2007) 433.
[7] W.A. Rolke and A. M. Lopez, Nucl. Instrum. Meth. A **458** (2001) 745.
[8] J.R. Batley *et al.*, Phys. Lett. B **697** (2011) 107.

Neutral pion form factor by the NA62 experiment

MARCO MIRRA*

Università degli studi di Napoli "Federico II" e Sezione INFN di Napoli, Italy
marco.mirra@na.infn.it

Abstract

The NA62 experiment collected a large sample of charged kaon decays in 2007 with a highly efficient trigger for decays into electrons. A measurement of the π^0 electromagnetic transition form factor slope parameter from 1.11×10^6 fully reconstructed $K^{\pm} \to \pi^{\pm}\pi^0_D$, $\pi_D \to e^+e^-\gamma$ events is reported. The measured value $a = (3.70 \pm 0.53_{stat} \pm 0.36_{syst}) \times 10^{-2}$ is in good agreement with theoretical expectations and previous measurements, and represents the most precise experimental determination of the slope in the time-like momentum transfer region. The limits on dark photon production in π^0 decays from the earlier kaon experiment NA48/2 at CERN are also reported.

*for the NA62 collaboration: F. Ambrosino, A. Antonelli, G. Anzivino, R. Arcidiacono, W. Baldi, S. Balev, J. R. Batley, M. Behler, S. Bifani, C. Biino, A. Bizzeti, T. Blazek, B. Bloch-Devaux, G. Bocquet, V. Bolotov, F. Bucci, N. Cabibbo, M. Calvetti, N. Cartiglia, A. Ceccucci, P. Cenci, C. Cerri, C. Cheshkov, J. B. Chze, M. Clemencic, G. Collazuol, F. Costantini, A. Cotta Ramusino, D. Coward, D. Cundy, A. Dabrowski, G. DAgostini, P. Dalpiaz, C. Damiani, H. Danielsson, M. De Beer, G. Dellacasa, J. Derr, H. Dibon, D. Di Filippo, L. DiLella, N. Doble, V. Duk, J. Engelfried, K. Eppard, V. Falaleev, R. Fantechi, M. Fidecaro, L. Fiorini, M. Fiorini, T. Fonseca Martin, P. L. Frabetti, A. Fucci, S. Gallorini, L. Gatignon, E. Gersabeck, A. Gianoli, S. Giudici, A. Gonidec, E. Goudzovski, S. Goy Lopez, E. Gushchin, B. Hallgren, M. Hita-Hochgesand, M. Holder, P. Hristov, E. Iacopini, E. Imbergamo, M. Jeitler, G. Kalmus, V. Kekelidze, K. Kleinknecht, M. Koval, V. Kozhuharov, W. Kubischta, V. Kurshetsov, G. Lamanna, C. Lazzeroni, M. Lenti, E. Leonardi, L. Litov, D. Madigozhin, A. Maier, I. Mannelli, F. Marchetto, G. Marel, M. Markytan, P. Marouelli, M. Martini, L. Masetti, P. Massarotti, E. Mazzucato, A. Michetti, I. Mikulec, M. Misheva, N. Molokanova, E. Monnier, U. Moosbrugger, C. Morales Morales, M. Moulson, S. Movchan, D.J. Munday, M. Napolitano, A. Nappi, G. Neuhofer, A. Norton, T. Numao, V. Obraztsov, V. Palladino, M. Patel, M. Pepe, A. Peters, F. Petrucci, M. C. Petrucci, B. Peyaud, R. Piandani, M. Piccini, G. Pierazzini, I. Polenkevich, I. Popov, Y. Potrebenikov, M. Raggi, B. Renk, F. Retire, P. Riedler, A. Romano, P. Rubin, G. Ruggiero, A. Salamon, G. Saracino, M. Savri, M. Scarpa, V. Semenov, A. Sergi, M. Serra, M. Shieh, S. Shkarovskiy, M. W. Slater, M. Sozzi, T. Spadaro, S. Stoynev, E. Swallow, M. Szleper, M. Valdata-Nappi, P. Valente, B. Vallage, M. Velasco, M. Veltri, S. Venditti, M. Wache, H. Wahl, A. Walker, R. Wanke, L. Widhalm, A. Winhart, R. Winston, M. D. Wood, S. A. Wotton, O. Yushchenko, A. Zinchenko and M. Ziolkowski

I. THE π^0 ELECTROMAGNETIC TRANSITION FORM FACTOR SLOPE PARAMETER

The π^0 decays almost instantaneously via the electromagnetic interaction with two photons. The second most important decay channel, the so-called Dalitz decay (π^0_D), is $\pi^0_D \to e^+e^-\gamma$ and proceeds via the same π^0 vertex with probability $(1.174 \pm 0.035)\%$ [1]. In the π^0_D process one of the two photons from the π^0 vertex becomes off-shell and decays to an e^+e^- pair. Independent kinematic variables x and y can be defined in terms of particle four-momenta $p_{e^\pm}$ and p_{π^0} :

$$x = \left(\frac{M_{ee}}{m_{\pi^0}}\right)^2 = \frac{(p_{e^+} + p_{e^-})^2}{m^2_{\pi^0}} \qquad y = \frac{2p_{\pi^0}\,(p_{e^+} + p_{e^-})}{m_{\pi^0}\,(1-x)} \tag{1}$$

where M_{ee} is the invariant mass of the e^+e^- pair. The x variable is the normalised square of the electron-positron pair invariant mass, while y is related to the angles between the final state particle momenta. The limits on the variables are given by

$$\mathrm{r}^2 \le \mathrm{x} \le 1 \quad -\beta \le \mathrm{y} \le \beta \quad \text{where} \quad \mathrm{r} = \frac{2\mathrm{m_e}}{\mathrm{m_{\pi^0}}} \quad \text{and} \quad \beta = \sqrt{1 - \frac{\mathrm{r}^2}{\mathrm{x}}} \tag{2}$$

where m_e and m_{π^0} are the the corresponding PDG [1] masses of $e^\pm$ and π^0.
The differential decay width is [2]

$$\frac{d^2\Gamma\left(\pi^0_D\right)}{dxdy} = \frac{\alpha}{4\pi}\Gamma\left(\pi^0_{2\gamma}\right)\frac{(1-x)^3}{x}\left(1 + y^2 + \frac{r^2}{x}\right)(1 + \delta\,(x,y))\,|F\,(x)|^2 \tag{3}$$

where $\Gamma\left(\pi^0_{2\gamma}\right)$ is the $\pi^0 \to \gamma\gamma$ decay width, the function $\delta\,(x,y)$ describes the radiative corrections and $F\,(x)$ is the electromagnetic transition form factor (TFF) of the π^0 to a real and virtual photon. The TFF describes the deviation of this transition from a point-like interaction. It is also an input to the computation of the $\pi^0 \to e^+e^-$ decay rate [3], as well as the hadronic light-by-light scattering contribution to the muon anomalous magnetic moment $(g-2)$ which at present contributes the second largest uncertainty on its Standard Model value [4].
The function $F\,(x)$ is expected to vary slowly in the kinematic region of the π^0_D decay and it is usually approximated by a linear expansion $F\,(x) = 1 + ax$, where a is the slope parameter. The TFF slope has been determined in the time-like momentum transfer region by measuring the π^0_D decay rate [5] [6] [7] [8] [9], all including radiative corrections. The TFF has been also measured in the space-like momentum transfer region in the reaction $e^+e^- \to e^+e^-\pi^0$, where the π^0 is produced by the fusion of two photons radiated by the incoming beams and decays to two detected photons [10]. The current world average $a = 0.032 \pm 0.004$ [1] is obtained from time-like measurements and the extrapolation of space-like data using a vector meson dominance (VMD) model. So a comparison of TFF slope prediction with model independent measurement represents a remarkable test of the theory models.

i. The π^0 TFF slope in NA62

The NA62 experiment at the CERN SPS collected in 2007 a large sample of charged kaons decaying in flight in vacuum with a minimum-bias trigger configuration [17]. The $K^\pm$ decays represent a source of tagged neutral pions by means of the $K^\pm \to \pi^+\pi^0$ ($K_{2\pi}$) decay channel. The mean free path of the neutral pion in the NA62 experimental conditions is negligible (few μm). An analysis of 1.11×10^6 $K_{2\pi}$ decays followed by the prompt π^0_D decay (denoted $K_{2\pi D}$) using the full NA62 2007 data set has been performed: a model-independent measurement of the π^0 TFF slope parameter is reported in this work.

II. NA62 EXPERIMENTAL APPARATUS

The NA62 experimental setup used in 2007 was composed of the NA48 detector [11] and a modified beam line [12] of the earlier NA48/2 experiment. The beam line was designed to provide simultaneously K^+ and K^- beams. The primary 400 GeV/c proton beam delivered by the SPS impinged on a beryllium target of 40 cm length and 0.2 cm diameter. The secondary beam momenta were selected by magnets in a four dipole achromat and a momentum-defining slit incorporated into a beam dump. This 3.2m thick copper/iron block provided the possibility to block either of the K^+ or K^- beams. The selected particles had a central momentum of 74 GeV/c with a spread of $\pm$1.4 GeV/c (rms). The beams were focused and collimated before entering a 114m long cylindrical vacuum tank containing the fiducial decay volume. The beams were mostly composed of $\pi^\pm$, with a $\sim 6\%$ $K^\pm$ fraction. Since the muon halo sweeping system was optimised for the positive beam in 2007, most of the data were recorded with the single K^+ beam to reduce the halo background. In figure 1 a schematic of the setup is shown. The momenta of charged

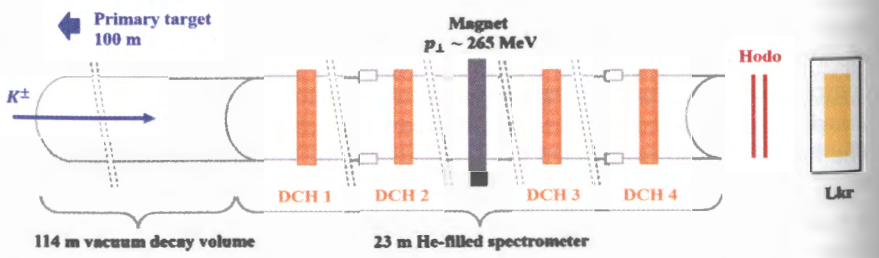

Figure 1: *Layout of the NA62 experimental setup.*

particles were measured by a spectrometer composed of four drift chambers (DCH) and a dipole magnet placed between the second and third chamber providing a transverse momentum kick of 265MeV/c. The measured momentum resolution was $\sigma_p/p = 0.48\% \oplus 0.009\%p$, where the momentum p is expressed in GeV/c. The spectrometer was housed in a tank filled with helium at nearly atmospheric pressu

The photons were detected and measured by a liquid krypton (LKr) electromagnetic calorimeter, which is a quasi-homogeneous ionisation chamber with a thickness of 127 cm, corresponding to $27X_0$. The LKr volume is divided into 13248 cells of about 2×2 cm^2 cross section without longitudinal segmentation. The measured energy resolution was $\sigma_E/E = 3.2\%/\sqrt{(E)} \oplus 9\%/E \oplus 0.42\%$, and the spatial resolution for the transverse coordinates x and y was $0.42\ \text{cm}/\sqrt{E} \oplus 0.06$ cm where the energy is given in GeV in both cases. A scintillator hodoscope (Hodo) was located between the spectrometer and the LKr calorimeter. It consists of a set of scintillators arranged into a plane of 64 vertical counters followed by a plane of 64 horizontal counters. Each plane was divided into four quadrants of 16 counters providing a fast trigger signal for charged particles. The time resolution of the Hodo was $\sim$ 150 ps.

The analysis is based on the full data set collected during 4 months in 2007, corresponding to about 2×10^{10} $K^\pm$ decays in the vacuum tank. A total of 65% (8%) of the K^+ (K^-) flux was collected in single-beam mode while the remaining 27% were collected with simultaneous $K^\pm$ beams with a K^+/K^- flux ratio of 2.0. The 100 kHz kaon decay rate in the vacuum volume during the spill enabled the use of a minimum-bias trigger configuration with a highly efficient trigger chain optimised to select events with at least one electron track. The low level hardware trigger required a coincidence of hits in at least one hodoscope quadrant in both planes, upper and lower cuts on the hit multiplicity in the drift chambers, and a minimum total energy deposit of 10 GeV in the LKr calorimeter. The high level software trigger (HLT) condition required at least one track with 5 GeV/c $< p <$ 90 GeV/c and $E/p > 0.6$, where E is the energy reconstructed in the calorimeter and p is the momentum reconstructed in the spectrometer. Downscaled minimum bias trigger streams were collected to evaluate the trigger efficiencies.

III. MONTECARLO SIMULATION

Monte Carlo (MC) simulations of the $K_{2\pi D}$ decay chain and two other $K^\pm$ decay chains producing π^0 Dalitz decays, $K^\pm \to \pi^0_D e^\pm \nu$ and $K^\pm \to \pi^0_D \mu^\pm \nu$ (denoted K_{e3D} and $K_{\mu 3D}$, respectively), were performed with a π^0 TFF slope $a_{MC} = 3.2 \times 10^2$. Separate simulated samples, proportionally to the number of kaon decays recorded, were produced for each data taking condition. The total simulated sample amounts to 386 M $K_{2\pi D}$, 105 M $K_{\mu 3D}$ and 103 M K_{e3D} events within the fiducial decay region. All these modes contribute to the π^0_D sample, although the selection is optimized for $K_{2\pi D}$. The radiative corrections to the total and differential π^0_D decay widths have been studied extensively since their effect is comparable to the effect of the TFF. The first study of radiative corrections was done in [13] and extended in [14], where diagrams in figures 2 and 3 were considered. Recent improvements in [15] include additional one-loop one-photon irreducible contributions (see figure 4) and they have been applied in this simulation. Higher order correction terms not included in the simulation contribute to the slope by

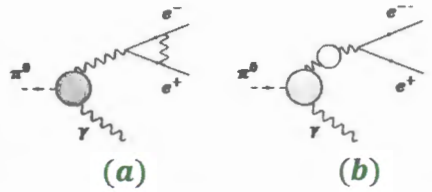

Figure 2: *Virtual radiative corrections to π^0_D: (a) correction to the QED vertex and (b) vacuum polarization insertion*

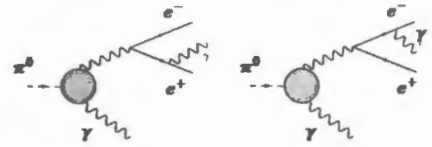

Figure 3: *Bremsstrahlung corrections to π^0_D*

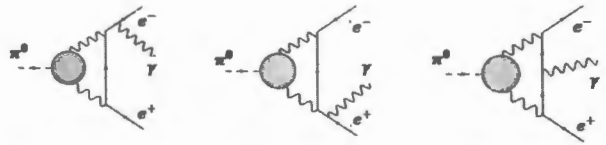

Figure 4: *One-loop one-photon irreducible contribution to π^0_D*

$|a| < 0.01 \times 10^2$, which is considered as a systematic uncertainty.

IV. TFF MEASUREMENT

i. Event selection

The main $K_{2\pi D}$ selection criteria are the following.

- The event should contain exactly one reconstructed 3-track vertex, which should be located within the fiducial decay region and be geometrically compatible with a beam kaon decay. The vertex charge qvtx, defined as the sum of the track charges, should match the beam charge in the single-beam mode. The track with the charge opposite to qvtx is necessarily an $e^{\pm}$ candidate, while the same-sign tracks can be either $\pi^{\pm}$ or $e^{\pm}$ candidates. The tracks are required to be in time and within the geometrical acceptance of the drift chambers. Events with a photon converting into an e^+e^- pair in the material before DCH1 are suppressed by requiring a minimum distance of 2 cm between the impact points of every track pair in the first drift chamber, as verified by simulation.
- Reconstructed clusters of energy deposition in the LKr calorimeter are used to identify photon candidates. A photon candidate cluster should be geometrically isolated from the track impact points in the LKr calorimeter (distance larger than 20 cm from the same-sign tracks and larger than 10 cm from the remaining track), within 10 ns of each track and with more than 2 GeV of energy. The photon 4-momentum is reconstructed assuming that the photon originates from the same vertex as the tracks. If more than one photon candidate is found, the event is rejected.
- The total reconstructed momentum should be compatible with the beam momentum and there should be no missing transverse momentum with respect to the beam axis within the resolution: $p_t^2 < 10^5 (\mathrm{GeV/c})^2$. The π/e ambiguity for the two same-sign tracks is resolved by testing the two possible mass assignments. For each hypothesis, the reconstructed kinematic variables should be $|x|, |y| < 1$, and the reconstructed $e^+e^-\gamma$ and $\pi^{\pm}\pi^0$ masses should be close to the nominal ones: $M_{ee\gamma}$ in the range $(115 - 145)\mathrm{MeV/c^2}$ and $M_{\pi^{\pm}\pi^0}$ in the range $(460 - 520)\mathrm{MeV/c^2}$. Both invariant mass spectra are shown in figure 5; Only events with a single valid hypothesis are selected. The probability of correct (incorrect) mass assignment evaluated with the $K_{2\pi D}$ MC sample is 99.62% (0.02%); the remaining 0.36% of events have either zero or two valid hypotheses are rejected.

The selection was restricted to area with Dalitz variable $x > 0.01$ because a 1% deficit in the data/MC ratio was observed for events with $x < 0.01$ due to the steeply falling acceptance.

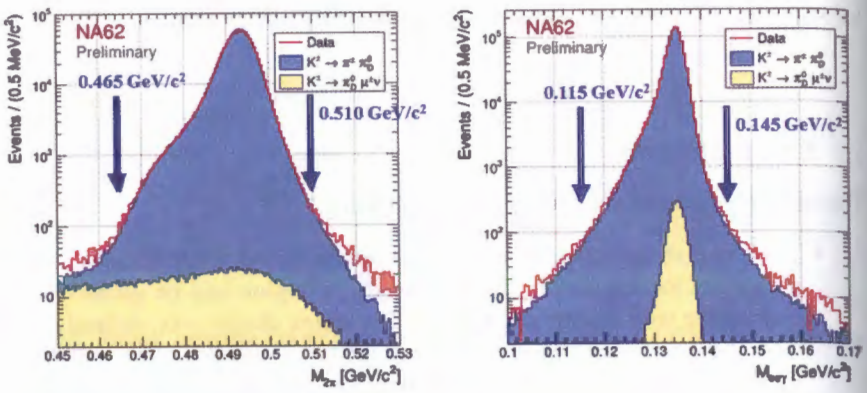

Figure 5: *Reconstructed $\pi^{\pm}\pi^0$ (left) and $e^+e^-\gamma$ (right) mass distributions for data and simulated components. The radiative shoulders in the reconstructed masses are well reproduced in the MC thanks to the simulation of the radiative photon.*

ii. Fit procedure and result

The reconstructed spectrum of the x variable is shown in figure 6 (left). The TFF was obtained by adjusting the simulation to the data x spectrum. In particular a χ^2 fit with free MC normalisation in equally populated bins comparing the data and MC reconstructed x distributions is performed to extract the TFF slope. The fit result is illustrated in figure 6 (right) where the effect of a positive TFF slope is clearly seen from the ratio of the data and MC distribution with $a = 0$. The horizontal positions of black markers correspond to the barycenters of the data divided into 20 equipopulous bins. MC events are re-weighted to obtain the distribution corresponding to the flat form factor (zero TFF slope value). Red solid line represents the TFF function with the slope value equal to the fit central value. Red dashed lines correspond to the 1 σ band.
The NA62 preliminary result on π^0 TFF slope parameter is:

$$a = (3.70 \pm 0.53_{stat} \pm 0.36_{syst}) \times 10^{-2} \quad (4)$$

A comparison with previous π^0 TFF measurements is shown in figure 7 . The measurement performed by NA62 is in good agreement with theoretical expectations and previous measurements, and represents the most precise experimental determination of the slope in the time-like momentum transfer region.

V. A RELATED RESEARCH: DARK PHOTON

In a rather general set of hidden sector models with an extra U(1) gauge symmetry [16], the interaction of the dark photon (DP, denoted A') with the visible sector proceeds through kinetic mixing with the Standard Model (SM) hypercharge. Such

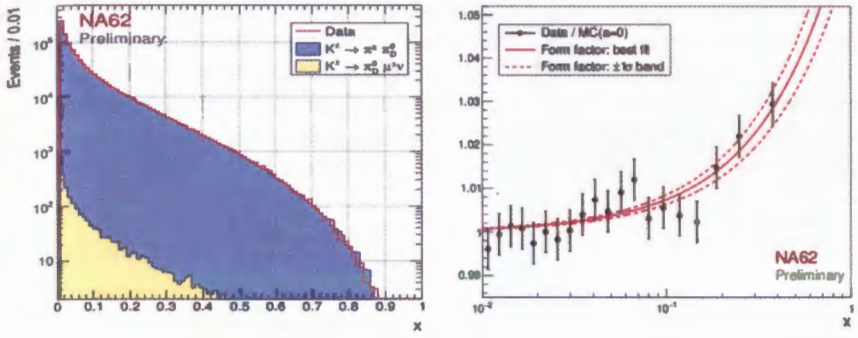

Figure 6: *Left: Spectra of the reconstructed x variable for data and MC components. Right: Ratio of the reconstructed x distributions for data and MC, where the MC sample corresponds to $a = 0$. The effect of a positive TFF slope ($a > 0$) is clearly seen in this illustration. Data and MC events are distributed into 20 equally populated bins; the horizontal positions of the markers correspond to the bin barycentres. The solid line represents $|F(x)|^2$ with the measured central slope value: $a = 3.70 \times 10^2$. The dashed lines indicate the $\pm 1\sigma$ band. Only the statistical uncertainties are shown.*

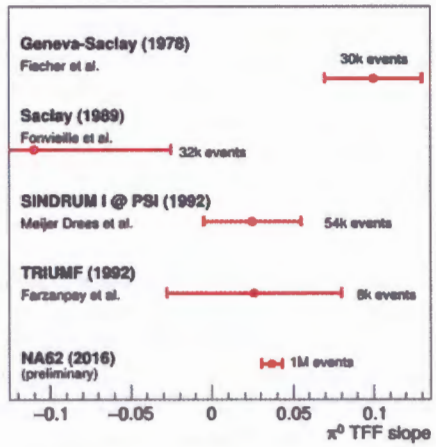

Figure 7: *Results on the TFF slope from π^0_D measurements.*

scenarios with GeV-scale dark matter provide possible explanations to the observed rise in the cosmic-ray positron fraction with energy and the muon gyromagnetic ratio $(g-2)$ measurement [17]. The DP is characterized by two a priori unknown parameters, the mass $m_{A'}$ and the mixing parameter ϵ^2. Its possible production in the π^0 decay and its subsequent decay proceed via the chain $\pi^0 \to \gamma A'$, $A' \to e^+e^-$. The expected branching fraction of the above π^0 decay [18]:

$$BR(\pi^0 \to \gamma A') = 2\epsilon^2 \left(1 - \frac{m_{A'}^2}{m_{\pi^0}}\right)^3 BR\left(\pi^0 \to \gamma\gamma\right) \tag{5}$$

In the DP mass range $2m_e < m_{A'} < m_\pi^0$ accessible in pion decays, the only allowed tree-level decay into SM fermions is $A' \to e^+e^-$. Therefore, for a DP decaying only into SM particles, $BR(A' \to e^+e) \approx 1$, and the expected total decay width is [18]:

$$\Gamma_{A'} \approx \Gamma\left(A' \to e^+e\right) = \frac{1}{3}\alpha\epsilon^2 m_{A'} \sqrt{1 - \frac{4m_e^2}{m_{A'}^2}} \left(1 + \frac{2m_e^2}{m_{A'}^2}\right) \tag{6}$$

It follows that, for $2m_e << m_{A'} < m_\pi^0$, the DP mean proper lifetime τ'_A satisfies the relation

$$c\tau_{A'} = \hbar c/\Gamma_{A'} \approx 0.8\mu\mathrm{m} \left(\frac{10^{-6}}{\epsilon^2}\right) \times \left(\frac{100\mathrm{MeV/c^2}}{\mathrm{m_{A'}}}\right) \tag{7}$$

The DP is assumed to decay at the production point, which is valid for sufficiently large values of $m_{A'}$ and ϵ^2. In this case, the DP production and the signal decay chain has the same particles in the final state as the π^0_D decay, which therefore represents an irreducible but well controlled background and determines the sensitivity. The result of the analysis of the full data set of NA48/2 counting in total $1.69 \times 10^7 \pi^0_D$ reconstructed events is reported. The π^0_D events are selected from kaon decays $K_{2\pi D}$ and $K_{\mu 3D}$. The two event selections are identical up to the momentum, invariant mass and particle identification conditions. A scan for a DP signal in the mass range $9\mathrm{MeV/c^2} \leq \mathrm{m_{A'}} \leq 120\mathrm{MeV/c^2}$ is performed. The lower boundary of the mass range is determined by the limited accuracy of the π^0_D background simulation at low e^+e^- mass. At high DP mass approaching the upper limit of the mass range, the sensitivity to the mixing parameter ϵ^2 is not competitive with the existing limits due to the kinematic suppression of the $\pi^0 \to \gamma A'$ decay. The obtained upper limits on the numbers of DP candidates in each mass hypothesis considered are presented in figure 8 (left). The obtained upper limits at 90% CL on the mixing parameter ϵ^2 for each DP mass value are shown in figure 8 (right), together with the constraints from other experiments.

The obtained limits are more stringent than the previous ones in the mass range 9-70 $\mathrm{MeV/c^2}$. In combination with other experimental searches, this result rules out the DP as an explanation for the muon $(g-2)$ measurement under the assumption that the DP couples to quarks and decays predominantly to SM fermions.

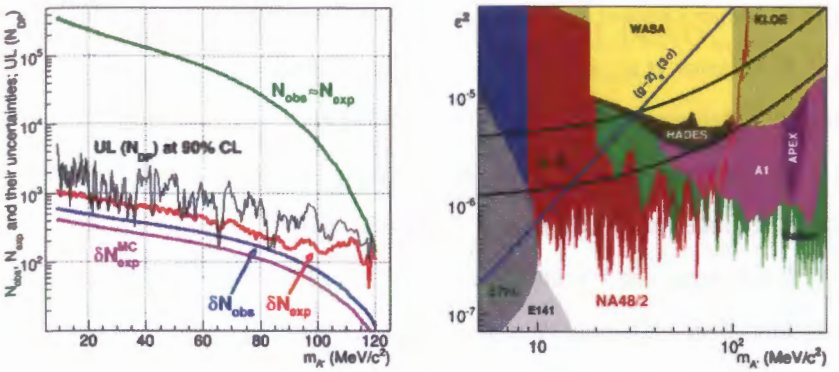

Figure 8: *Left: Numbers of observed data events and expected π^0_D background events passing the selection, estimated uncertainties and obtained upper limits at 90% CL on the numbers of DP candidates for each mass value $m_{A'}$. Right: The NA48/2 preliminary upper limits at 90% CL on the mixing parameter ϵ^2 versus the A' mass, compared to the other published exclusion limits. Also shown are the band for the muon $(g-2)$ and the region excluded by the electron $(g-2)$ measurement.*

VI. Conclusion

Kaon decay in flight experiments are also exposed to large numbers of tagged neutral pion decays. The most precise measurement of the π^0 transition form factor slope has been performed by analyzing the NA62 data set. The final result including slightly smaller uncertainties has been published recently [19].
Improved limits in the 9-70 $\mathrm{MeV/c^2}$ mass range of the dark photon search in π^0 decays has been achieved by exploring NA48/2 data. The whole region favored by $(g-2)$ is excluded now, assuming that DP decays into SM fermions only.

References

[1] C. Patrignani et al., Chin. Phys. C 40, 100001 (2016).

[2] D. W. Joseph, Il Nuovo Cimento 16, 997 (1960).

[3] T. Husek, K. Kampf, and J. Novotny, Eur. Phys. J. C 74, 3010 (2014).

[4] A. Nyffeler, Phys. Rev. D 94, 053006 (2016).

[5] J. Fischer et al., Phys. Lett. B 73, 359 (1978).

[6] H. Fonvieille et al., Phys. Lett. B 233, 65 (1989).

[7] F. Farzanpay et al., Phys. Lett. B 278, 413 (1992).

[8] R. Meijer Drees et al., Phys. Rev. D 45, 1439 (1992).

[9] P. Adlarson et al., arXiv:1611.04739 [hep-ex] (2016).

[10] H. J. Behrend et al., Z. Phys. C 49, 401 (1991).

[11] V. Fanti et al., Nucl. Instrum. Meth. A 574, 433 (2007).

[12] J. R. Batley et al., Eur. Phys. J. C 52, 875 (2007).

[13] B E Lautrup and J Smith, Phys. Rev. D 3, 1122 (1971).

[14] Mikaelian and Smith, Phys. Rev. D 5, (1972) 1763.

[15] T Husek et al, Phys. Rev. D 92, 054027 (2015).

[16] B. Holdom, Phys. Lett. B166 (1986) 196.

[17] M. Pospelov, Phys. Rev. D80 (2009) 095002.

[18] B. Batell, M. Pospelov and A. Ritz, Phys. Rev. D80 (2009) 095024.

[19] CERN-EP-2016-323 and arXiv:1612.08162, accepted for publication by Phys. Lett. B.

Search for $K^+ \to \pi^+ \nu\overline{\nu}$ at NA62

Jacopo Pinzino*
INFN Sezione di Pisa, Italy
E-mail: jacopo.pinzino@cern.ch

March 14, 2017

Abstract

$K^+ \to \pi^+ \nu\overline{\nu}$ is one of the theoretically cleanest meson decay where to look for indirect effects of new physics complementary to LHC searches.

*for the NA62 Collaboration: G. Aglieri Rinella, R. Aliberti, F. Ambrosino, R. Ammendola, B. Angelucci, A. Antonelli, G. Anzivino, R. Arcidiacono, I. Azhinenko, S. Balev, M. Barbanera, J. Bendotti, A. Biagioni, L. Bician, C. Biino, A. Bizzeti, T. Blazek, A. Blik, B. Bloch-Devaux, V. Bolotov, V. Bonaiuto, M. Boretto, M. Bragadireanu, D. Britton, G. Britvich, M.B. Brunetti, D. Bryman, F. Bucci, F. Butin, J. Calvo, E. Capitolo, C. Capoccia, T. Capussela, A. Cassese, A. Catinaccio, A. Cecchetti, A. Ceccucci, P. Cenci, V. Cerny, C. Cerri, B. Checcucci, O. Chikilev, S. Chiozzi, R. Ciaranfi, G. Collazuol, A. Conovaloff, P. Cooke, P. Cooper, G. Corradi, E. Cortina Gil, F. Costantini, F. Cotorobai, A. Cotta Ramusino, D. Coward, G. D'Agostini, J. Dainton, P. Dalpiaz, H. Danielsson, J. Degrange, N. De Simone, D. Di Filippo, L. Di Lella, S. Di Lorenzo, N. Dixon, N. Doble, B. Dobrich, V. Duk, V. Elsha, J. Engelfried, T. Enik, N. Estrada, V. Falaleev, R. Fantechi, V. Fascianelli, L. Federici, S. Fedotov, A. Filippi, M. Fiorini, J. Fry, J. Fu, A. Fucci, L. Fulton, S. Gallorini, S. Galeotti, E. Gamberini, L. Gatignon, G. Georgiev, S. Ghinescu, A. Gianoli, M. Giorgi, S. Giudici, L. Glonti, A. Goncalves Martins, F. Gonnella, E. Goudzovski, R. Guida, E. Gushchin, F. Hahn, B. Hallgren, H. Heath, F. Herman, T. Husek, O. Hutanu, D. Hutchcroft, L. Iacobuzio, E. Iacopini, E. Imbergamo, O. Jamet, P. Jarron, E. Jones, T. Jones K. Kampf, J. Kaplon, V. Kekelidze, S. Kholodenko, G. Khoriauli, A. Khotyantsev, A. Khudyakov, Yu. Kiryushin, A. Kleimenova, K. Kleinknecht, A. Kluge, M. Koval, V. Kozhuharov, M. Krivda, Z. Kucerova, Yu. Kudenko, J. Kunze, G. Lamanna, G. Latino, C. Lazzeroni, G. Lehmann-Miotto, R. Lenci, M. Lenti, E. Leonardi, P. Lichard, R. Lietava, V. Likhacheva, L. Litov, R. Lollini, D. Lomidze, A. Lonardo, M. Lupi, N. Lurkin, K. McCormick, D. Madigozhin, G. Maire, C. Mandeiro, I. Mannelli, G. Mannocchi, A. Mapelli, F. Marchetto, R. Marchevski, S. Martellotti, P. Massarotti, K. Massri, P. Matak, E. Maurice, M. Medvedeva, A. Mefodev, E. Menichetti, E. Migliore, E. Minucci, M. Mirra, M. Misheva, N. Molokanova, J. Morant, M. Morel, M. Moulson, S. Movchan, D. Munday, M. Napolitano, I. Neri, F. Newson,J. Noël, A. Norton, M. Noy, G. Nuessle, T. Numao, V. Obraztsov, A. Ostankov, S. Padolski, R. Page, V. Palladino, G. Paoluzzi, C. Parkinson, E. Pedreschi, M. Pepe, F. Perez Gomez, M. Perrin-Terrin, L. Peruzzo, P. Petrov, F. Petrucci, R. Piandani, M. Piccini, D. Pietreanu, J. Pinzino, I. Polenkevich, L. Pontisso, Yu. Potrebenikov, D. Protopopescu, F. Raffaelli, M. Raggi, P. Riedler, A. Romano, P. Rubin, G. Ruggiero, V. Russo, V. Ryjov, A. Salamon, G. Salina, V. Samsonov, C. Santoni, G. Saracino, F. Sargeni, V. Semenov, A. Sergi, M. Serra, A. Shaikhiev, S. Shkarovskiy, I. Skillicorn, D. Soldi, A. Sotnikov, V. Sugonyaev, M. Sozzi, T. Spadaro, F. Spinella, R. Staley, A. Sturgess, P. Sutcliffe, N. Szilasi, D. Tagnani, S. Trilov, M. Valdata-Nappi, P. Valente, M. Vasile, T. Vassilieva, B. Velghe, M. Veltri, S. Venditti, P. Vicini, R. Volpe, M. Vormstein, H. Wahl, R. Wanke, P. Wertelaers, A. Winhart, R. Winston, B. Wrona, O. Yushchenko, M. Zamkovsky, A. Zinchenko.

The NA62 experiment at CERN SPS is designed to measure the branching ratio of this decay with 10% precision. NA62 took data in pilot runs in 2014 and 2015 reaching the final designed beam intensity. The quality of 2015 data acquired, in view of the final measurement, will be presented.

1 The NA62 experiment

1.1 Introduction

The NA62 experiment is located in the CERN North Area SPS extraction site and it aims at measuring the Branching Ratio of the ultra-rare FCNC kaon decay $K^+ \to \pi^+\nu\bar{\nu}$ collecting about 100 events in two years of data taking [2]. This decay, with its neutral partner $K_L \to \pi^0\nu\bar{\nu}$, is a very useful process to study flavour physics and to obtain a stringent test of the Standard Model; the Branching Ratio of these decays can be computed with high precision [4], $BR(K^+ \to \pi^+\nu\bar{\nu})(SM) = 8.4 \pm 1.0 \times 10^{-11}$ where the uncertainty is dominated by the current precision of the CKM mixing matrix input parameters.

The strong suppression of the SM contributions and the remarkable theoretical precision of the SM rate make this decay a powerful probe for possible new physics, complementary to direct searches at the LHC and potentially sensitive to much higher energy scales. The combination of the Branching Ratio of these two decays ($K^+ \to \pi^+\nu\bar{\nu}$ and $K^0 \to \pi^0\nu\bar{\nu}$) allows to determine the β angle of the Unitarity Triangle from K decays only and, in this way, to have a powerful test on Standard Model.

The most accurate measurement of this decay, $BR(K^+ \to \pi^+\nu\bar{\nu}) = 17.3^{+11.5}_{-10.5} \times 10^{-11}$, was obtained by the E787 experiment and its upgrade E949 at BNL (from 1995 to 2002) which collected seven events [3]. NA62 aims to improving the measurement of this Branching Ratio reaching a precision of at least 10%: the experiment is currently in data taking and the performances achieved in 2015 will be discussed.

1.2 NA62 Experimental Setup

NA62 uses the SPS 400 GeV/*c* proton beam from the SPS in order to produce K^+ decaying in-flight.

The total beam rate at the end of the beam line is of the order of 750 MHz but kaons are about 6% of the flux. Downstream detectors aren't affected by this large flux because the undecayed particles remain inside the beam pipe; the integrated rate over these detectors is of the order of 10 MHz.

The downstream detectors start about 100 m after the beryllium target and are distributed along 170 m longitudinally; the fiducial region for decays extends from 100 m to 165 m after the target. Detectors have an approximate azimuthal symmetry around the beam axis, with an inner hole to let the high

flux of undecayed particles pass through without hitting the downstream detectors.

The NA62 experimental setup [1], shown in figure 1, consists of these detectors:

- The *Cerenkov differential counter* (KTAG) is used to identify K^+ in the beam. It has a time resolution of about 100 ps to tag the kaon time.
- The Gigatracker (GTK) is composed by three silicon pixel stations placed in vacuum, with transverse dimensions which cover the beam area, and is used to measure particles direction and momentum before they enter the decay region. The GTK has to cope with the full beam intensity of about 750 MHz and provides a time resolution of the order 200 ps to avoid a wrong matching of a beam particle to the reconstructed decay downstream, and a resulting error in the calculation of the missing mass. Between the stations, 4 magnetic dipoles make an achromatic spectrometer for any momentum: the momentum resolution is 0.2%, and the angular resolution for the particle direction is about 15 μrad.
- The CHarged ANTIcounter (CHANTI) is a set of scintillator rings that follow the last GTK station used as a veto for charged particles before they enter the decay region.
- A system of photon veto detectors covering a polar angle from 0 to about 50 mrad polar angle with respect to the beam direction using 12 large annular vetos (LAV) made of lead glass crystals with attached photomultipliers (PMT) and covering an angle from 8.5 to 50 mrad, a liquid krypton electromagnetic calorimeter (LKr) for angles between 1 and 8.5 mrad, an intermediate calorimeter (IRC), made of alternating layers of lead and scintillators (shashlik), to cover the ring around the beam and a small angle calorimeter (SAC) placed at the end of the beam line after a sweeping magnet and using the same shashlik technology.
- A magnetic spectrometer (STRAW) made of four straw tube chambers inside the vacuum tank is used to measure the position of the decay vertex, the direction and momentum of the charged secondary particle. The reason to operate in vacuum is to minimize the multiple scattering. The dipole magnet from the earlier NA48 experiment is located after the second chamber and provides a 270 MeV/*c* kick in the horizontal plane, for track momentum determination. In the center of each chamber a region without straw let the beam particles pass undisturbed.
- The Ring Imaging Cerenkov (RICH) is designed to distinguish π and μ in the momentum range between 15 and 35 GeV/*c* and to measure direction and velocity of such particles. This detector is 17 m long, filled with Neon at atmospheric pressure and equipped with 2000 photomultipliers

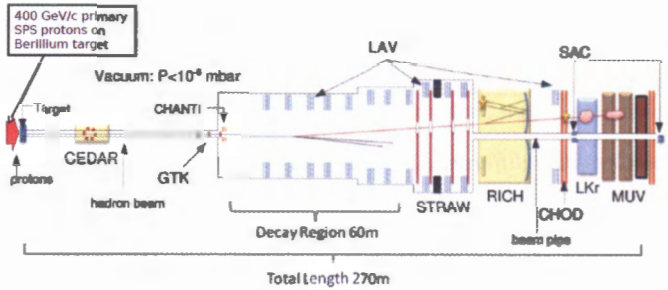

Figure 1: Longitudinal view of the NA62 experimental setup.

and has an inner beam pipe to avoid beam interactions with the gas. The timing resolution is of the order of 100 ps.

- The Charged Hodoscope (CHOD) is placed after the RICH to reduce the inefficiency in photon detection due to conversion or photo-nuclear interactions inside the material of the RICH; moreover it is used for trigger purposes.

- A system of muon vetoes composed of two iron-scintillator hadronic calorimeters (MUV1 and MUV2), and a plane of fast scintillators (MUV3 placed after an iron wall, gives additional power in muon vetoing and a fast trigger information.

2 Experimental strategy

The $K^+ \to \pi^+ \nu\bar{\nu}$ signature is one track in the final state matched in time with one K^+ track upstream the decay region and nothing else, because the two neutrinos are undetectable. Backgrounds can originate from all the kaon decays that result in a single detected charged track with no other particles, or from beam related activity. Kinematic reconstruction is a useful rejection technique the squared missing mass distribution of the signal, $m^2_{miss} \stackrel{def}{=} (P_K - P_{\pi^+})^2$ (where P_K and P_{π^+} are, respectively, the 4-momenta of the kaon and the charged particles produced from kaon decay under the π^+ mass hypothesis) has a three body decay shape, while more than 90% of the charged kaon decays are mostly peaking, as shown in figure 2.

The distribution of the m^2_{miss} for the signal and the main decay modes led to define two signal regions, where the main backgrounds should be limited by the kinematic constrains, around the $K^+ \to \pi^+\pi^0$ peak. Semileptonc decays radiative processes, main kaon decay modes via reconstruction tails and beam induced tracks span across these regions. Therefore kinematic reconstruction

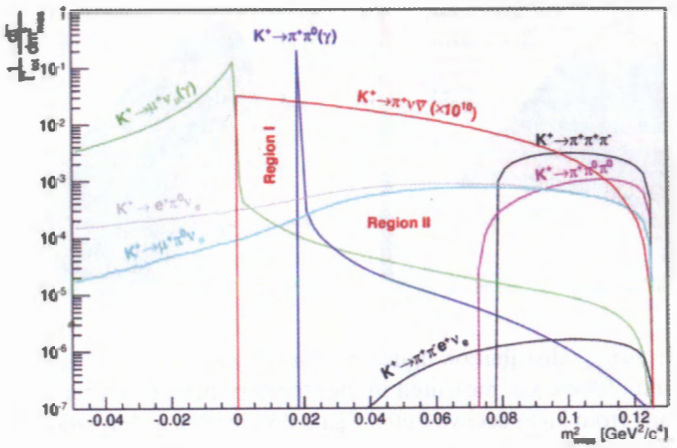

Figure 2: m^2_{miss} distributions for signal and backgrounds from the main K^+ decay modes. The backgrounds are normalized according to their branching fraction; the espected signal is shown multiplied by a factor 10^{10}.

photon rejection, particle identification and sub-nanoseconds timing coincidences between subdetectors must be employed to obtain the final background rejection. A tight requirement on P_{π^+} between 15 and 35 GeV/c boosts the background suppression further, as will be shown in the next section. Monte Carlo studies performed in past years [5] have shown that NA62 can reach the goal, exploiting multiple and almost uncorrelated techniques to suppress the main background sources.

3 Preliminary result of the 2015 run and prospect for the $K^+ \to \pi^+ \nu\bar{\nu}$ measurement

The main goal of the 2015 run was to verify on data the expected detector performances, the timing,, the particle identification and the kinematic and photon rejection. A single track selection was chosen as a preliminary step towards the $K^+ \to \pi^+ \nu\bar{\nu}$ measurement. We selected tracks reconstructed in the STRAW spectrometer matching with CHOD signals and with energy depositions in calorimeters. The CHOD signals define the track time with 200 ps resolution. A single track event is defined by a track not forming a common vertex with any other in-time track within the decay region. The position of the vertex is defined using using a Closest Distance of Approach (CDA) less than 1.5 cm between two tracks. The downstream track has to match a Gigatracker track in time and space, forming a vertex in the decay region with it, in order

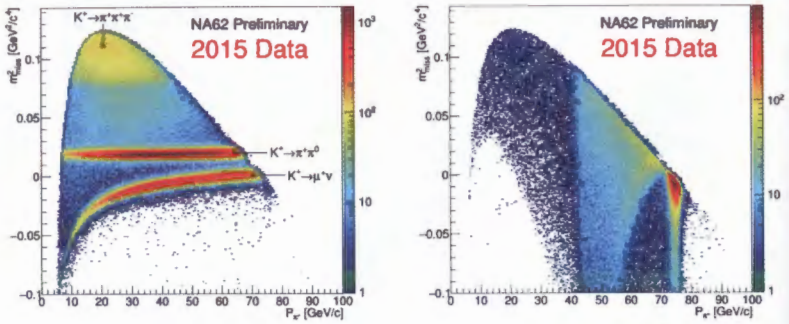

Figure 3: m^2_{miss} distribution under π^+ mass hypothesis as a function of the momentum of the track measured in the straw spectrometer after selection for single track from kaon decays (left). Same distribution as left-side picture, but asking for single track without a positive kaon tag in time in KTAG (right).

to select events originating from kaon decays. The Gigatracker track has to be in-time with a kaon-like signal in KTAG. On the right, the KTAG is used to select events related to kaons. Time resolutions of the KTAG and GTK are found to match the design values (100 and 200 ps respectively). The m^2_{miss} distributions for the 2015 data, recorded at low intensity, are shown in figure 3: the figure on the left is done with a kaon-like signal in the KTAG, while, in the second, the KTAG is used in anti-coincidence with a Gigatracker track to select single track events not related to kaons and shows that decay from beam π^+, elastic scattering of beam particles in the material along the beam line (KTAG and Gigatracker stations) and inelastic scattering in the last Gigatracker station are the main sources of tracks downstream originating from beam related activity.

The resolution of the m^2_{miss} is measured using the width of the $K^+ \to \pi^+\pi^0$ peak and it is found to be $1.2 \times 10^{-3} GeV^2/c^4$ close to design value. The resolution as a function of momentum is shown in figure 4. The resolution is a factor 3 larger if the nominal kaon momentum is taken, instead of the event by event Gigatracker measured value.

The tracking system of NA62 is also designed to provide a rejection factor in the range of $10^4 \div 10^5$ for $K^+ \to \pi^+\pi^0$ and $K^+ \to \mu^+\nu$ using m^2_{miss} to separate signal from backgrounds, respectively. The $K^+ \to \pi^+\pi^0$ kinematic suppression is measured using a sub-sample of single track events from kaon decays selected by requiring the additional presence of two γs' compatible with a π^0 in the LKr calorimeter. This constraint defines a sample of $K^+ \to \pi^+\pi^0$ with negligible background even in the signal m^2_{miss} regions, allowing the study of the far tails of the m^2_{miss}. The measured $K^+ \to \pi^+\pi^0$ kinematic suppression factor is of the order of 10^3. The partial hardware Gigatracker

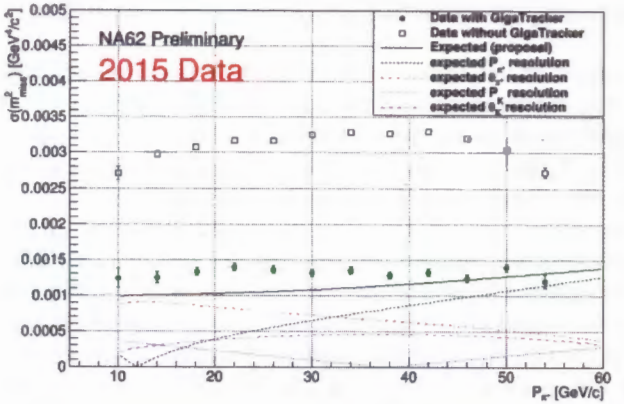

Figure 4: Resolution of the m^2_{miss} miss vs momentum. Empty squares correspond to the values obtained with the nominal kaon momentum, black points - with the kaon momentum measured by GTK.

arrangement used in 2015 mainly limits the suppression because of m^2_{miss} tails due to beam track mis-reconstruction.

The particle identification of NA62 is designed to separate π^+ from μ^+ and e^+ in order to guarantee at least 7 order of magnitude suppression of $K^+ \to \mu^+\nu$ in addition to the kinematic rejection. The identification of secondary charged particles is done employing together RICH and calorimeters. The $K^+ \to \pi^+\pi^0$ sample used for kinematic studies and a pure muon sample of $K^+ \to \mu^+\nu$ were used to study the $\pi^+ - \mu^+$ separation in the RICH. The required muon contamination of 1% was achieved with a π^+ ID efficiency of 80% measured in a momentum region between 15 and 35 GeV/c. The RICH provides also an even better separation between π^+ and e^+. The same π^+ and μ^+ samples allow the calorimetric muon-pion separation to be investigated. Simple cut and count analysis provide a muon suppression factor within $10^4 \div 10^6$ for a π^+ efficiency in a $90\% \div 50\%$ range. Several analysis techniques are under study to get the optimal separation.

The photon veto system is designed to suppress decays with photons in the final state. For photons from π^0 decays the rejection power provided by LAV, LKr, IRC and SAC detectors should be at least 8 orders of magnitude. The measured π^0 veto inefficiency on the 2015 data is statistically limited at 10^6 (90% CL) as an upper limit. The corresponding signal efficiency is above 90%, being the losses mainly due to π^+ interactions in the RICH material producing extra clusters in LKr. To conclude, the preliminary analysis of the low intensity 2015 data shows that NA62 is approaching the design sensitivity for measuring $K^+ \to \pi^+\nu\bar{\nu}$.

4 NA62 physics besides $K^+ \to \pi^+\nu\overline{\nu}$

The performances of the apparatus allow physics opportunities beyond the $K^+ \to \pi^+\nu\overline{\nu}$ to be addressed. NA62 can significantly improve the existing limits on lepton flavour and number violating decays like $K^+ \to \pi^+\mu^\pm e^\mp$ or $K^+ \to \pi^- l^+ l^+$. Experimentally π^0 physics can take advantage of the performances of the electromagnetic calorimeters and processes like $\pi^0 \to invisible$ or dark photon production can be investigated. Thanks to the quality of the kinematic reconstruction, searches for heavy neutrino produced in $K^+ \to l^+\nu$ decays can improve the present sensitivity. The longitudinal scale of the apparatus open the possibility to search for long living particles through their decays, like dark photon, heavy neutral leptons or axion-like particles produced at the target or in beam dump configurations. NA62 is already addressing part of the above physics program simultaneously with the $K^+ \to \pi^+\nu\overline{\nu}$ program. The full exploitation of this physics will constitute the core of the NA62 program beyond 2018.

References

[1] A. Ambrosino et al. "NA62 Technical Design Document". In: (2010). URL: https://na62.web.cern.ch/NA62/Documents/TD_Full_doc_v10.pdf.

[2] G. Anelli et al. "Proposal to measure the rare decay K+ —> pi+ nu anti-nu at the CERN SPS". In: (2005).

[3] A. V. Artamonov et al. "New measurement of the $K^+ \to \pi^+\nu\overline{\nu}$ branching ratio". In: *Phys. Rev. Lett.* 101 (2008), p. 191802. DOI: 10.1103/PhysRevLett.101.191802. arXiv: 0808.2459 [hep-ex].

[4] Andrzej J. Buras et al. "$K^+ \to \pi^+\nu\overline{\nu}$ and $K_L \to \pi^0\nu\overline{\nu}$ in the Standard Model: status and perspectives". In: *JHEP* 11 (2015), p. 033. DOI: 10.1007/JHEP11(2015)033. arXiv: 1503.02693 [hep-ph].

[5] Ferdinand Hahn. "Status and Prospects for $K^+ \to \pi^+\nu\overline{\nu}$ Observation at CERN". In: *PoS* KAON13 (2013), p. 032.

Review of Higgs Results from the ATLAS Experiment at the LHC

I.I. Tsukerman for the ATLAS Collaboration,
National Research Center "Kurchatov Institute", Institute of Theoretical and Experimental Physics (ITEP), Moscow, 117218, Russia
e-mail: Ilya.Tsukerman@cern.ch

Abstract. The LHC has now delivered a large amount of data at 13 TeV center of mass energy. The experimental sensitivity is equivalent to that of Run-1 for the Higgs boson (125 GeV), and surpasses it for searches of higher masses Higgs-like particles. This paper will review recent ATLAS results on both of these topics.

Introduction

A new boson with a mass of 125 GeV was discovered by the ATLAS [1] and CMS [2] Collaborations at the Large Hadron Collider [3] (LHC) more than four years ago. Studies of the Higgs boson properties were based on full dataset accumulated at proton-proton (*pp*) collision at 7 TeV center of mass energy (≈5 fb^{-1}) and on partial of 8 TeV data (≈5 fb^{-1}). Since that time both experiments recorded another 20 fb^{-1} of 8 TeV data in 2012 and about 40 fb^{-1} taken at 13 TeV *pp*-collision energy in 2015–2016. The ATLAS experiment [4] has analyzed the full statistics at 7 and 8 TeV as well as about 40% of the 13 TeV statistics. All measured properties of the new boson are found to be compatible with the Standard Model (SM) predictions for the Higgs boson (*H*). It was a great success of the SM. However, the SM does not explain particle mass hierarchy, dark matter, dark energy, baryon asymmetry of the Universe and has problems with the unification of fundamental interactions [5]. Different extensions of the SM were proposed by theorists to solve these problems. These extensions contain different amount of extra Higgs bosons. The ATLAS Collaboration performed neutral and charged Higgs boson searches in different decay modes. This report contains a short summary of these searches and is organized as follows. Section 1 briefly describes SM Higgs boson decay modes. In Section 2, results on some bosonic and fermionic decay modes obtained at 13 TeV are given. Beyond-the-Standard-Model (BSM) Higgs boson searches are reviewed in Section 3 together with a pair production of Higgs bosons. Section 4 contains summary of results for the SM *H* obtained at 7–8 TeV *pp*-collision energy; the conclusion is drawn in Section 5.

1 SM Higgs boson decay channels

The main production mechanisms of the SM Higgs boson at hadron colliders at LHC energies are gluon fusion (ggF), vector boson fusion (VBF), associated production with a *W*- or a *Z*-boson (*VH*) or with a pair of top quarks (*ttH*); expected cross sections σ_H at the mass 125 GeV [6] are shown in Fig. 1(a) in the *pp* energy

SM is measured to be 1.18 ± 0.15 [31]. This result is obtained from the analysis of the $H \to ZZ^* \to 4\ell$, $H \to \gamma\gamma$, $H \to WW^* \to \ell\nu\ell\nu$, $H \to \tau\tau$ and $H \to bb$ decay channels. Note that the first three channels are seen in the ATLAS experiment.

Table 2. Brief summary of the results related to the SM Higgs boson obtained at 7 and 8 TeV collision energy in the ATLAS experiment.

Parameter	Value	Ref.	Comment
Mass, GeV	125.36 ± 0.41	[29]	125.09 ± 0.24 with the CMS
Average μ	1.18 ± 0.15	[31]	1.09 ± 0.10 with the CMS
μ for $H \to \gamma\gamma$	$1.17^{+0.28}_{-0.26}$	[31]	5.2σ (discovery)
μ for $H \to 4\ell$	$1.46^{+0.40}_{-0.34}$	[31]	8.1σ (discovery)
μ for $H \to \ell\nu\ell\nu$	$1.18^{+0.24}_{-0.21}$	[31]	6.5σ (discovery)
μ for $H \to \tau\tau$	$1.44^{+0.42}_{-0.37}$	[31]	4.5σ (evidence)
μ for $H \to bb$	$0.63^{+0.39}_{-0.37}$	[31]	1.4σ (no evidence)
μ for ggF	$1.23^{+0.23}_{-0.20}$	[31]	$1.03^{+0.17}_{-0.15}$ with the CMS
μ for VBF	$1.23^{+0.32}_{-0.32}$	[31]	$1.18^{+0.25}_{-0.23}$ with the CMS
μ for VH	0.80 ± 0.36	[31]	$0.84^{+0.40}_{-0.38}$ with the CMS
μ for ttH	1.81 ± 0.80	[31]	$2.3^{+0.7}_{-0.6}$ with the CMS
Spin/parity	0^+	[32]	4ℓ, $\ell\nu\ell\nu$ and $\gamma\gamma$ modes
Width, MeV	≤22.7 (95% CL)	[33]	Off-shell $H \to ZZ/WW$
BR($H \to inv.$)	≤0.28 (95% CL)	[34]	Important for WIMP searches

with ≥5σ significance. The resulting signal strength from two LHC experiments is found to be 1.09 ± 0.10 [7]. Analyzing the $H \to ZZ^* \to 4\ell$, $H \to WW^* \to e\nu\mu\nu$ and $H \to \gamma\gamma$ decay modes, we conclude with very high confidence level that a spin-parity of the Higgs boson is 0^+, as predicted by the SM [32]. From the off-shell measurements of the $H \to ZZ^* \to 4\ell$ and $H \to WW^* \to \ell\nu\ell\nu$ channels the upper limit is put to the H width as 22.7 MeV at 95% CL [33]. The ATLAS experiment also looks for invisible decay of the Higgs boson, $H \to inv.$, which is interesting for WIMP searches. The upper limit on BR($H \to inv.$) ≤0.28 is established at 95% CL [34].

In summary, no significant deviation from the SM is observed in the ATLAS studies of the Higgs boson at 7–8 TeV.

5 Conclusion

With the 7 and 8 TeV LHC data the ATLAS experiment measured properties of the Higgs boson such as its couplings, mass, spin and parity. No significant deviation from the SM is found. Using 13-15 fb^{-1} of the 13 TeV LHC data, the ATLAS obtained preliminary results reconfirming the Higgs boson discovery in the 4ℓ and $\gamma\gamma$ modes. With the same dataset, the ATLAS performed searches for neutral and charge Higgs bosons predicted by some extensions of the SM. No evidence for new physics was found yet. Limits on the H boson production cross sections in different models were put. The ATLAS Collaboration continues to study properties of the SM-like H boson improving precision of their measurements and to search for exotic Higgs bosons with new 13 TeV data.

The work is partially supported by MES of Russia, grant RFMEFI61014X0005.

References

[1] ATLAS Collaboration, Phys. Lett. B716, 1 (2012)
[2] CMS Collaboration, Phys. Lett. B716, 30 (2012)
[3] L. Evans and P. Bryant (editors), Journal of Instrumentation 3, S08001 (2008)
[4] ATLAS Collaboration, Journal of Instrumentation, 3, S08003 (2008)
[5] C. Patrignani *et al.* (Particle Data Group), Chin. Phys. C, **40**, 100001 (2016)
[6] LHC Higgs boson cross section working group, https://twiki.cern.ch/twiki/bin/view/LHCPhysics/LHCHXSWG
[7] ATLAS and CMS Collaborations, JHEP 08 (2016) 045
[8] ATLAS Collaboration, ATLAS-CONF-2016-079, http://cds.cern.ch/record/2206253/files/ATLAS-CONF-2016-079.pdf
[9] ATLAS Collaboration, ATLAS-CONF-2016-067, http://cds.cern.ch/record/2206210/files/ATLAS-CONF-2016-067.pdf
[10] ATLAS Collaboration, ATLAS-CONF-2016-081, http://cds.cern.ch/record/2206272/files/ATLAS-CONF-2016-081.pdf
[11] ATLAS Collaboration, ATLAS-CONF-2016-091, http://cds.cern.ch/record/2206813/files/ATLAS-CONF-2016-091.pdf
[12] ATLAS Collaboration, ATLAS-CONF-2016-080, http://cds.cern.ch/record/2206255/files/ATLAS-CONF-2016-080.pdf
[13] ATLAS Collaboration, ATLAS-CONF-2016-058, http://cds.cern.ch/record/2206153/files/ATLAS-CONF-2016-058.pdf
[14] ATLAS Collaboration, ATLAS-CONF-2016-068, http://cds.cern.ch/record/2206211/files/ATLAS-CONF-2016-068.pdf
[15] ATLAS Collaboration, ATLAS-CONF-2016-041, http://cds.cern.ch/record/2206079/files/ATLAS-CONF-2016-041.pdf
[16] ATLAS Collaboration, ATLAS-CONF-2016-059, http://cds.cern.ch/record/2206154/files/ATLAS-CONF-2016-059.pdf
[17] ATLAS Collaboration, ATLAS-CONF-2016-074, http://cds.cern.ch/record/2206243/files/ATLAS-CONF-2016-074.pdf
[18] ATLAS Collaboration, ATLAS-CONF-2016-062, http://cds.cern.ch/record/2206199/files/ATLAS-CONF-2016-062.pdf
[19] ATLAS Collaboration, ATLAS-CONF-2016-056, http://cds.cern.ch/record/2206138/files/ATLAS-CONF-2016-056.pdf
[20] ATLAS Collaboration, ATLAS-CONF-2016-082, http://cds.cern.ch/record/2206275/files/ATLAS-CONF-2016-082.pdf
[21] ATLAS Collaboration, ATLAS-CONF-2016-044,

http://cds.cern.ch/record/2206125/files/ATLAS-CONF-2016-044.pdf
[22] ATLAS Collaboration, JHEP 09 (2016) 1
[23] CMS Collaboration, arXiv:1609.02507, submitted to Phys. Lett. B.
[24] ATLAS Collaboration, ATLAS-CONF-2016-085,
http://cds.cern.ch/record/2206278/files/ATLAS-CONF-2016-085.pdf
[25] ATLAS Collaboration, ATLAS-CONF-2016-089,
http://cds.cern.ch/record/2206809/files/ATLAS-CONF-2016-089.pdf
[26] ATLAS Collaboration, ATLAS-CONF-2016-088
http://cds.cern.ch/record/2206282/files/ATLAS-CONF-2016-088.pdf
[27] ATLAS Collaboration, ATLAS-CONF-2016-071,
http://cds.cern.ch/record/2206222/files/ATLAS-CONF-2016-071.pdf
[28] ATLAS Collaboration, ATLAS-CONF-2016-049,
http://cds.cern.ch/record/2206131/files/ATLAS-CONF-2016-049.pdf

[29] ATLAS Collaboration, Phys. Rev. D90 (2014) 052004
[30] ATLAS and CMS Collaborations, Phys. Rev. Lett. 114 (2015) 191803
[31] ATLAS Collaboration, Europ. Phys. J. C76 (2016) 6
[32] ATLAS Collaboration, Europ. Phys. J. C75 (2015) 476
[33] ATLAS Collaboration, Europ. Phys. J. C75 (2015) 335
[34] ATLAS Collaboration, JHEP 01 (2016) 172

Two-particle Bose–Einstein correlations in pp collisions at $\sqrt{s} = 0.9$ and 7 TeV measured with the ATLAS detector

Y.A. Kulchitsky [1), 2)]

On behalf of the ATLAS Collaboration

[1)] *Joint Institute for Nuclear Research, Dubna, Russia*
[2)] *Institute of Physics, National Academy of Sciences, Minsk, Belarus*

Abstract

The paper presents studies of Bose–Einstein Correlations for pairs of like-sign charged particles measured in the kinematic range $p_T > 100$ MeV and $|\eta| < 2.5$ in proton–proton collisions at centre-of-mass energies of 0.9 and 7 TeV with the ATLAS detector at the CERN Large Hadron Collider. The multiplicity dependence of the Bose–Einstein Correlations parameters characterizing the correlation strength and the correlation source size are investigated for charged-particle multiplicities of up to 240. A saturation effect in the multiplicity dependence of the correlation source size parameter is observed using the high-multiplicity 7 TeV data sample. The dependence of the Bose–Einstein Correlations parameters on the average transverse momentum of the particle pair is also investigated.

1 Introduction

Correlations between identical bosons, called Bose-Einstein correlations (BEC), are a well-known phenomenon in high-energy and nuclear physics. The BEC are often considered to be the analogue of the Hanbury-Brown and Twiss effect [1] in astronomy, describing the interference of incoherently emitted identical bosons [2–4]. They represent a sensitive probe of the space-time geometry of the hadronization region and allow the determination of the size and the shape of the source from which particles are emitted.

The production of identical bosons that are close together in phase space is enhanced by the presence of BEC. The first observation of BEC effects in identically charged pions produced in $p\bar{p}$ collisions was reported in Ref. [5]. Since then, BEC have been studied for systems of two or more identical bosons produced in various types of collisions, from leptonic to hadronic and nuclear collisions.

Studies of the dependence of BEC on particle multiplicity and transverse momentum help to understand the multiparticle production mechanism. The size of the source emitting the correlated particles has been observed to increase with particle multiplicity. This can be understood as arising from the increase in the initial geometrical region of overlap of the colliding objects [6]: a large overlap implies a large multiplicity. While this dependence is natural in nucleus–nucleus collisions, the increase of size with multiplicity has also been observed in hadronic and leptonic interactions. In the latter, it is understood as a result of superposition of many sources [7–9] or related to the number of jets [10, 11]. High-multiplicity data in proton-proton interactions can serve as a reference for studies of nucleus–nucleus collisions. The effect is reproduced in both the hydrodynamical/hydrokinetic [12–14] and Pomeron-based [15, 16] approaches for hadronic interactions where high multiplicities play a crucial role. The dependence on the transverse momentum of the emitter particle pair is another important feature of the BEC effect [17].

In this studies of one-dimensional Bose–Einstein Correlations effects in pp collisions at centre-of-mass energies of 0.9 and 7 TeV, using the ATLAS detector [18] at the Large Hadron Collider (LHC) [19], are presented in the Ref. [20]. At the LHC, BEC have been studied by the CMS [21, 23] and ALICE [24, 25] experiments. In the analysis reported here, the studies are extended to the region of high-multiplicities available thanks to the high multiplicity track trigger.

2 Analysis

2.1 Two-particle correlation function

Bose–Einstein correlations are measured in terms of a two-particle correlation function,

$$C_2(p_1, p_2) = \frac{\rho(p_1, p_2)}{\rho_0(p_1, p_2)}, \tag{1}$$

where p_1 and p_2 are the four-momenta of two identical bosons in the event, ρ is the two-particle density function, and ρ_0 is a two-particle density function (known as the reference function) specially constructed to exclude BEC effects. The densities ρ and ρ_0 are normalized to unity, i.e. they are the probability density functions.

In order to compare with data over the widest possible range of centre-of-mass energies and system sizes, the density function is parameterized in terms of the Lorentz-invariant four-momentum difference squared, Q^2, of the two particles,

$$Q^2 = -(p_1 - p_2)^2. \tag{2}$$

The BEC effect is usually described by a function with two parameters: the effective radius parameter R and the strength parameter λ [26], where the latter is also called the incoherence or chaoticity parameter. A typical functional form is

$$C_2(Q) = \frac{\rho(Q)}{\rho_0(Q)} = C_0[1 + \Omega(\lambda, QR)](1 + \varepsilon Q). \tag{3}$$

In a simplified scheme for fully coherent emission of identical bosons, $\lambda = 0$, while for incoherent (chaotic) emission, $\lambda = 1$. The QR dependence comes from the Fourier transform of the distribution of the space-time points of boson emission. Several different functional forms have been proposed for $\Omega(\lambda, QR)$. Those used in this paper are described in Sect. 2.4. The fitted parameter ε takes into account long-distance correlations not fully removed from ρ_0. Finally, C_0 is a normalization constant, typically chosen such that $C_2(Q)$ is unity for large Q. In this paper, the density function ρ is calculated for like-sign charged-particle pairs, with both the $++$ and $--$ combinations included, $\rho(Q) \equiv \rho(++, --)$. All particles are treated as charged pions and no particle identification is attempted. The purity of the analysis sample in terms of identical boson pairs is estimated from MC to be about 70% (where about 69% are $\pi^{\pm}\pi^{\pm}$ and about 1% are $K^{\pm}K^{\pm}$). The effect of the purity is absorbed in the strength parameter λ, while the results of the analysis on the effective radius parameter R were found to be not affected.

2.2 Coulomb correction

The long-range Coulomb force causes a momentum shift between the like-sign and unlike-sign pairs of particles. The density distributions are corrected for this effect by applying the Gamow penetration factor per track pair with a weight $1/G(Q)$ [27–29],

$$\rho_{\mathrm{corr}}(Q) = \frac{\rho(Q)}{G(Q)}, \tag{4}$$

where the Gamow factor $G(Q)$ is given by

$$G(Q) = \frac{2\pi\zeta}{\mathrm{e}^{2\pi\zeta} - 1} \tag{5}$$

with the dimensionless parameter ζ defined as

$$\zeta = \pm\frac{\alpha m}{Q}. \tag{6}$$

Here α is the electromagnetic fine-structure constant and m is the pion mass. The sign of ζ is positive for like-sign pairs and negative for unlike-sign pairs. The resulting correction on $\rho(Q)$ decreases with increasing Q

and at $Q = 0.03$ GeV it is about 20%. A systematic uncertainty on $G(Q)$ is considered to cover effects like the extended size of the emission source and other effects, see discussion in Ref. [30]. Neither the Coulomb interaction nor the BEC effect are present in the generation of MC event samples which are used in the analysis. The Coulomb correction is thus not applied to MC events.

2.3 Reference sample

A good choice of the reference sample is important to allow the experimental detection of the BEC signal. Ideally, $\rho_0(Q)$ should include all momentum correlations except those arising from BEC. Thus, several different choices have been studied to construct an appropriate reference sample.

Most of the proposed approaches use random pairing of particles, such as mixing particles from different events (the "mixed event" technique [31]), or choosing them from the same event but from opposite hemispheres or by rotating the transverse momentum vector of one of the particles of the like-sign pair [32]. Although these mixing techniques reproduce the topology and some properties of the event under consideration and destroy BEC, they violate energy-momentum conservation. Moreover, there are many possible ways to construct the pairs, such as mixing the particles randomly, or keeping some topological constraints such as the event multiplicity, the invariant mass of the pair or the rapidity of the pair. All of these introduce additional biases in the BEC observables. For example, it was observed in dedicated MC studies that the single-ratio correlation functions C_2 using reference samples constructed with the event mixing or opposite hemispheres techniques exhibit an increase in the low-Q BEC sensitive region. This effect is found to be more pronounced with increase of the multiplicity or average particle-pair transverse momentum and indicates that these reference samples are not suitable.

A natural choice is to use the unlike-sign particle pairs from the same events that are used to form pairs of like-sign particles, i.e., $\rho_0(Q) \equiv \rho(+-)$, called in the following the unlike-charge reference sample. This sample has the same topology and global properties as the like sign sample $\rho(++,--)$, but is naturally free of any BEC effect. Studying the C_2 correlation functions on MC, none of the deficits of the event mixing and opposite hemispheres techniques described above were observed. However, this sample contains hadron pairs from the decay of resonances such as ρ, η, η', ω, ϕ, K^*, which are not present in the like-sign combinations. These contribute to the low-Q region and can give a spurious BEC signature with a large effective radius of the source [33–39].

In this paper, the unlike-charge reference sample is used. To account for the effects of resonances, the two-particle correlation function $C_2(Q)$ is corrected using Monte Carlo simulation without BEC effects via a double-

ratio $R_2(Q)$ defined as

$$R_2(Q) = \frac{C_2(Q)}{C_2^{MC}(Q)} = \frac{\rho(++,--)}{\rho(+-)} \quad \frac{\rho^{MC}(++,--)}{\rho^{MC}(+-)}. \tag{7}$$

2.4 The parameterizations of BEC

Various parameterizations of the $\Omega(\lambda, QR)$ function can be found in the literature, each assuming a different shape for the particle-emitting source. In the studies presented here, the data are analysed using the following parameterizations:

- the Goldhaber parameterization [5] of a static Gaussian source in the plane-wave approach,

$$\Omega = \lambda \cdot \exp\left(-R^2Q^2\right), \tag{8}$$

  which assumes a spherical shape with a radial Gaussian distribution of the emitter;

- the exponential parameterization of a static source

$$\Omega = \lambda \cdot \exp\left(-RQ\right), \tag{9}$$

  which assumes a radial Lorentzian distribution of the source. This parameterization provides a better description of the data at small Q values, as discussed in [32].

The first moment of the $\Omega\,(QR)$ distribution corresponds to $1\,/R$ for the exponential form and to $1/(R\sqrt{\pi})$ for the Gaussian form. To compare the values of the radius parameters obtained from the two functions, the R value of the Gaussian should be compared to $R/\sqrt{\pi}$ of the exponential form.

3 Experimental details

3.1 The ATLAS detector

The ATLAS detector [18] is a multi-purpose particle physics experiment operating at one of the beam interaction points of the LHC. The detector covers almost the whole solid angle around the collision point with layers of tracking detectors, calorimeters and muon chambers. It is designed to study a wide range of physics topics at LHC energies. For the measurements presented in this paper, the tracking devices and the trigger system are of particular importance.

The innermost part of the ATLAS detector is the inner detector (ID), which has full coverage in ϕ and covers the pseudorapidity range $|\eta| < 2.5$.

It consists of a silicon pixel detector (Pixel), a silicon microstrip detector (SCT) and a transition radiation tracker (TRT). These detectors are immersed in a 2 T solenoidal magnetic field. The Pixel, SCT, and TRT detectors have typical position resolutions of 10, 17 and 130 μm for the r-ϕ coordinate, respectively. In the case of the Pixel and SCT, the resolutions are 115 and 580 μm, respectively, for the second measured coordinate. A track from a charged particle traversing the full radial extent of the ID would typically have three Pixel hits, eight or more SCT hits and more than 30 TRT hits.

High-multiplicity track (HM) events were collected at 7 TeV using a dedicated high-multiplicity track trigger. At level trigger L1, the collisions were triggered using the summed transverse energy (ΣE_{T}) in all calorimeters, calibrated at the electromagnetic energy scale [40]. The high-multiplicity minimum-bias (MB) events were required to have $\Sigma E_{\mathrm{T}} > 20$ GeV. A high number of hits in the SCT was required at level trigger L2, while at the Event Filter EF level at least 124 tracks with $p_{\mathrm{T}} > 400$ MeV were required to originate from a single vertex.

3.2 Data and Monte Carlo samples

The study is carried out using the pp-collision datasets at the centre-of-mass energies $\sqrt{s} = 0.9$ and 7 TeV that were used in previously published ATLAS studies of minimum-bias interactions [41,42].

The event and track selection criteria are the same as the ones used for the ATLAS minimum-bias multiplicity analysis [41] with the same minimum-bias trigger and quality criteria for the track reconstruction. All events in these datasets are required to have at least one vertex [43], formed from a minimum of two tracks with $p_{\mathrm{T}} > 100$ MeV and consistent with the average beam spot position within the ATLAS detector (primary vertex) [44]. The tracks satisfying the above-mentioned selection criteria are used as the input to determine the corrected distributions, as described in Sect. 3.3. The multiplicity of selected tracks with $p_{\mathrm{T}} > 100$ MeV and $|\eta| < 2.5$ within an event is denoted by n_{sel}.

The same event selection criteria are applied to high-multiplicity events, which are defined to be those with at least 120 selected tracks. To estimate the possible influence of multiple pp interactions in the 7 TeV high-multiplicity track trigger data, the distribution of the distances Δz between the z coordinates of primary and pile-up vertices are studied. The study shows that on average there is less than one pile-up track selected in the HM sample, which has a negligible influence on the BEC studies.

Large Monte Carlo samples of minimum-bias and high-multiplicity events were generated using the PYTHIA 6.421 Monte Carlo event generator [45] with the ATLAS MC09 set of optimised parameters (tune) [46] (1.1×10^7 for $\sqrt{s} = 900$ GeV, 2.7×10^7 for $\sqrt{s} = 7$ TeV and 1.8×10^6 for $\sqrt{s} = 7$ TeV high-multiplicity data) with non-diffractive, single-diffractive and double-diffractive processes included in proportion to the cross sections predicted by the model. As discussed in Sec. 2.2, no simulation of the BEC effect is implemented in the generator. This is the baseline Monte Carlo generator which reproduces single-particle spectra [42]. The generated events were passed through the ATLAS simulation and reconstruction chain; the detector simulation program [47] is based on GEANT4 [48]. Dedicated sets of high-multiplicity events were also generated.

3.3 Data correction procedure

Following the procedure applied in the previous ATLAS minimum-bias measurements [41,42], each track is assigned a weight which corrects for the track reconstruction efficiency, for the fraction of secondary particles, for the fraction of the primary particles outside the kinematic range and for the fraction of fake tracks. In addition, the effect of events lost due to trigger and vertex reconstruction inefficiencies is corrected for using an event-by-event weight applied to pairs of particles in the Q distribution.

The multiplicity distributions are corrected to the particle level using an iterative method that follows the Bayesian approach [49] as it is described in Refs. [41,42].

4 Systematic uncertainties

The following contributions to the systematic uncertainties on the fitted parameters, R and λ, are considered. The systematic uncertainties resulting from the track reconstruction efficiency, which are parameterized in bins of p_{T} and η, were determined in earlier analyses [41,42]. These cause uncertainties in the track weights of particle pairs in the Q distributions entering the correlation functions.

The effects of the track splitting and merging are sizeable only for very low Q values (smaller than 5 MeV), and are found to be negligible for the measurements with $Q \geq 20$ MeV. The leading source of systematic uncertainty is due to differences in the Monte Carlo generators used to calculate the R_2 correlation function from the C_2 correlation function. The corresponding contribution to the systematic uncertainty is estimated as the root-mean-squared (RMS) spread of the results obtained for the different Monte Carlo datasets. The statistical uncertainties arising from the Monte Carlo datasets are negligibly small. The systematic uncertainty due to Coulomb corrections is estimated by varying the corrections by $\pm 20\%$. The influence of the fit range is estimated by changing the upper bound of the Q range from the nominal 2 GeV: decreasing it to 1.5 GeV and increasing it up to 2.5 GeV. The latter better estimates the uncertainty due the long-

range correlations. This contribution is taken into account by the value of ε, the parameter in the linear term of Eq. (3) describing the long-range correlations. Other effects contributing to the systematic uncertainties are the lowest value of Q for the fit, the bin size and exclusion of the interval $0.5 \leq Q \leq 0.9$ GeV due to the overestimate of the ρ meson contribution in the Monte Carlo simulations, as discussed in the following Sec. 5.1. These uncertainties are estimated by varying the lowest Q value in the fit by ± 10 MeV, by changing the bin size by ± 10 MeV, and by broadening the excluded interval by 100 MeV on both sides, respectively. The background of photon conversions into e^+e^- pairs was studied and found to be negligible. To test the effect of treating all charged particles as pions, the double-ratio correlation functions R_2 are also obtained using only identical particles in the Monte Carlo sample to compute the correction. The resulting BEC parameters fitted to the R_2 functions defined this way show negligible differences to the nominal result and no further systematic uncertainties are assigned. The same sources of uncertainty are considered for the differential measurements in $n_{\rm ch}$ and the average transverse momentum $k_{\rm T}$ of a pair, and their impact on the fit parameters is found to be similar in size.

5 Results

5.1 Two-particle correlations

In Fig. 1 the double-ratio $R_2(Q)$ distributions, measured for 0.9 and 7 TeV, are compared with Gaussian and exponential fitting functions, Eqs. (8) and (9). The fits are performed in the Q range 0.02 GeV to 2 GeV and with a bin width of 0.02 GeV. The upper Q limit is chosen to be far away from the low-Q region, which is sensitive to BEC effects and resonances. Around $Q \sim 0.7$ GeV there is a visible bump which is due to an overestimate of $\rho \to \pi^+\pi^-$ decays in the Monte Carlo simulation. Therefore the region $0.5 \leq Q \leq 0.9$ GeV is excluded from the fits. As seen in Fig. 1, the Gaussian function does not describe the low-Q region while the exponential function provides a good description of the data.

The resolution of the Q variable is better than 10 MeV for the region most sensitive to BEC effect, $Q < 0.4$ GeV. The Q resolution is included in the fit of R_2 by convolving the fitting function with a Gaussian detector resolution function. The change in the fit results from those with no convolution applied is found to be negligible.

In the process of fitting $R_2(Q)$ with the exponential function, large χ^2 values are observed, in particular for the 7 TeV sample where statistical uncertainties on the fitted data points are below 2–4%. These large χ^2 values can be traced back to a small number of individual points or small cluster of points. The removal of these points does not change the results of the fit

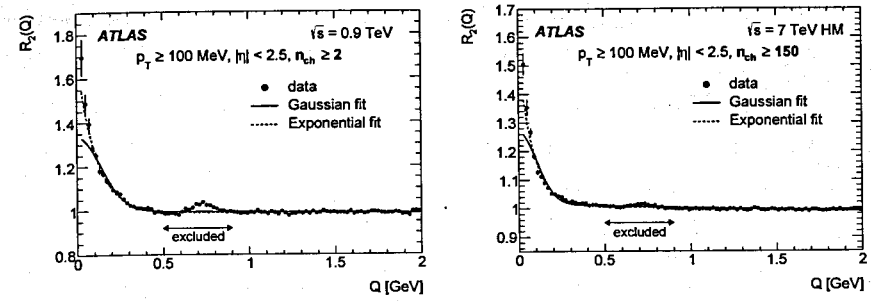

(a) (b)

Figure 1: The two-particle double-ratio correlation function $R_2(Q)$ for charged particles in pp collisions at (a) $\sqrt{s}$ =0.9 TeVand (b) 7 TeV high-multiplicity events. The lines show the Gaussian and exponential fits as described in the legend. The region excluded from the fits is indicated. The error bars represent the statistical uncertainties.

while the χ^2 substantially improves. In the analysis of the 7 TeV data, for most of the considered cases, the expected statistical uncertainties are small compared to the systematic ones, therefore only total uncertainties on the fitted parameters are given. The latter include the statistical uncertainties rescaled by $\sqrt{\chi^2/\mathrm{ndf}}$ [22]. For consistency, the same treatment is applied to the 0.9 TeV analysis where the statistical uncertainties are of the same order of magnitude as the systematic ones.

The results of BEC parameters for exponential fits of the two-particle double-ratio correlation function $R_2(Q)$ for events with the unlike-charge reference sample are

$$\lambda = 0.74 \pm 0.11,\ R = (1.83 \pm 0.25)\ \text{fm at}\ \sqrt{s} = 0.9\ \text{TeV for}\ n_{\rm ch} \geq 2,$$
$$\lambda = 0.71 \pm 0.07,\ R = (2.06 \pm 0.22)\ \text{fm at}\ \sqrt{s} = 7\ \text{TeV for}\ n_{\rm ch} \geq 2,$$
$$\lambda = 0.52 \pm 0.06,\ R = (2.36 \pm 0.30)\ \text{fm at}\ \sqrt{s} = 7\ \text{TeV for}\ n_{\rm ch} \geq 150.$$

The values of the fitted parameters are close to the values obtained by the CMS [23] and ALICE [24] experiments.

5.2 Multiplicity dependence

The multiplicity intervals are chosen so as to be similarly populated and comparable to those used by other LHC experiments [21, 23–25]. Only the exponential fit is shown. As in the fit procedure for the inclusive case, the detector Q resolution is included in the fits.

Within the multiplicity studies, the BEC parameters are also measured by excluding the low-multiplicity events, $n_{\rm ch} < 8$, expected to be contaminated by diffractive physics [42]. No noticeable changes in the strength and

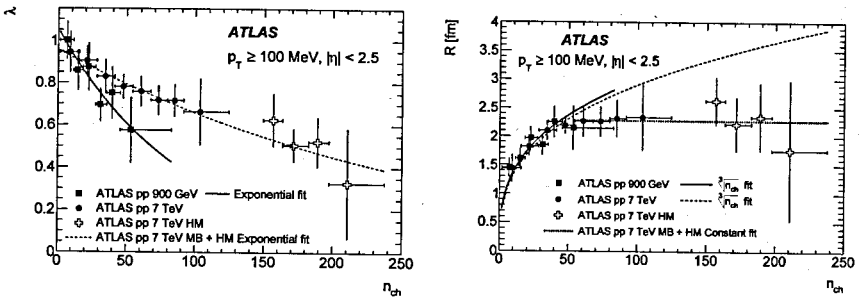

(a) (b)

Figure 2: Multiplicity, $n_{\rm ch}$, dependence of the parameters (a) λ and (b) R obtained from the exponential fit to the two-particle double-ratio correlation functions $R_2(Q)$ at $\sqrt{s}$ =0.9 and 7 TeV. The solid and dashed curves are the results of (a) the exponential and (b) $\sqrt[3]{n_{\rm ch}}$ for $n_{\rm ch} < 55$ fits. The dotted line in (b) is a result of a constant fit to minimum-bias and high-multiplicity events data at 7 TeVfor $n_{\rm ch} \geq 55$. The error bars represent the quadratic sum of the statistical and systematic uncertainties.

radius parameters for $n_{\rm ch} \geq 8$ are observed compared to the full multiplicity range for $n_{\rm ch} \geq 2$.

The multiplicity dependence of the λ and R parameters is shown in Fig. 2. The λ parameter decreases with multiplicity, faster for 0.9 TeV than for 7 TeV interactions. The decrease of the λ parameter with $n_{\rm ch}$ is found to be well fitted with the exponential function $\lambda(n_{\rm ch}) = \gamma\, e^{-\delta n_{\rm ch}}$.

The R parameter increases with multiplicity up to about $n_{\rm ch} \simeq 50$ independently of the center of mass energy. For higher multiplicities, the measured R parameter is observed to be independent of multiplicity. For $n_{\rm ch} \leq 82$ at 0.9 TeV and $n_{\rm ch} < 55$ at 7 TeV the $n_{\rm ch}$ dependence of R is fitted with the function $R(n_{\rm ch}) = \alpha \sqrt[3]{n_{\rm ch}}$, similar to that used in heavy-ion studies [25]. The results of the fit are close to the CMS results [23]. The fit parameters do not change significantly within uncertainties if data points with $n_{\rm ch} > 55$ are included in the fit, while the quality of the fit significantly degrades. Therefore the fit is limited to the data points with $n_{\rm ch} \leq 55$. The $n_{\rm ch}$ dependence of R at 7 TeV is fitted with a constant $R(n_{\rm ch}) = \beta$ for $n_{\rm ch} > 55$. Qualitatively CMS [23] and UA1 [50] results for radius parameter follow the same trend as a function of $n_{\rm ch}$ as ATLAS data points up to $n_{\rm ch} \leq 55$. The ATLAS and ALICE [24, 25] results on the multiplicity dependence of the radius parameter cannot be directly compared due to much narrower η region used by ALICE.

The observed change of the fitted parameters with multiplicity has been predicted in Refs. [7–9, 32], and is similar to the one also observed in e^+e^-

interactions [10], however the saturation of R for very high multiplicity is observed for the first time.

The saturation of R at high multiplicities is expected in a Pomeron-based model [15,16] as the consequence of the overlap of colliding protons, with the value of the radius parameter at $n_{\rm ch} \approx 70$ close to the one obtained in the present studies. However, the same model predicts that above $n_{\rm ch} \approx 70$, R will decrease with multiplicity, returning to its low-multiplicity value which is not supported by the data.

5.3 Dependence on the transverse momentum

The average transverse momentum $k_{\rm T}$ of a particle pair is defined as half of the magnitude of the vector sum of the two transverse momenta, $k_{\rm T} = |\mathbf{p}_{\rm T,1} + \mathbf{p}_{\rm T,2}|/2$. The study is performed in the $k_{\rm T}$ intervals which are chosen in a way to be similarly populated and, as for the multiplicity bins, to be similar to the intervals used by other LHC experiments [21, 23–25].

For the $R_2(Q)$ correlation function measured at 7 TeV, there is an indication that the Monte Carlo simulation overestimates the production and decay of the ω-meson in the Q region of 0.3–0.44 GeV. This region is thus excluded from the fit range for $k_{\rm T} > 500$ MeV bin results.

In the region most important for the BEC parameters, the quality of the exponential fit is found to deteriorate as $k_{\rm T}$ increases. This is due to the fact that at large $k_{\rm T}$ values, the characteristic BEC peak becomes steeper than the exponential function can accommodate. Despite the deteriorating fit quality, the behaviour of the fitted parameters is presented for comparison with previous experiments.

The fit values of the λ and R parameters are shown in Fig. 3 as a function of $k_{\rm T}$. The values of both λ and R decrease with increasing $k_{\rm T}$.

The decrease of λ with $k_{\rm T}$ is well described by an exponential function, $\lambda(k_{\rm T}) = \mu\, e^{-\nu k_{\rm T}}$. The $k_{\rm T}$ dependence of the R parameter is also found to follow an exponential decrease, $R(k_{\rm T}) = \xi\, e^{-\kappa k_{\rm T}}$. The shapes of the $k_{\rm T}$ dependence are similar for the 7 TeV and the 7 TeV high-multiplicity data.

In Fig. 3(b), the $k_{\rm T}$ dependence of the R parameter is compared to the measurements performed by the E735 [51] and the STAR [52] experiments with mixed-event reference samples. These earlier results were obtained from Gaussian fits to the single-ratio correlation functions and therefore the values of the measured radius parameters are multiplied by $\sqrt{\pi}$ as discussed in Sect. 2.4. The values of the parameters are observed to be energy-independent within the uncertainties.

In Fig. 4, the $k_{\rm T}$ dependence of λ and R, obtained for the 7 TeV data, is also studied in various multiplicity regions: $2 \leq n_{\rm ch} \leq 9$; $10 \leq n_{\rm ch} \leq 24$; $25 \leq n_{\rm ch} \leq 80$; and $81 \leq n_{\rm ch} \leq 125$. The decrease of λ with $k_{\rm T}$ is nearly independent of multiplicity for $n_{\rm ch} > 9$ and the same as for the inclusive case. For $n_{\rm ch} \leq 9$ no conclusions can be drawn due to the large uncertainties.

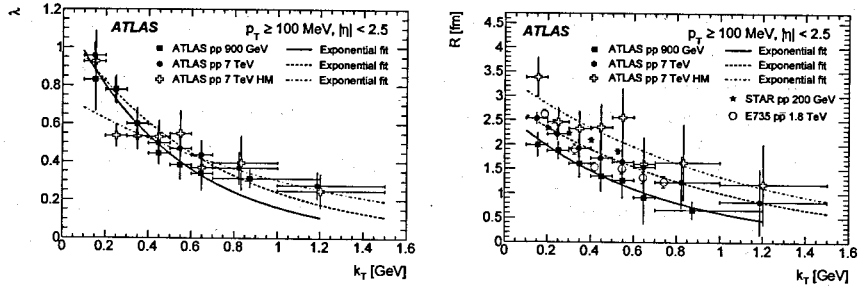

(a) (b)

Figure 3: The k_T dependence of the fitted parameters (a) λ and (b) R obtained from the exponential fit to two-particle double-ratio at $\sqrt{s}$ =0.9 TeV, 7 TeV and 7 TeV high-multiplicity events. The average transverse momentum k_T of the particle pairs is defined as $k_T = |\mathbf{p}_{T,1} + \mathbf{p}_{T,2}|/2$. The solid, dashed and dash-dotted curves are results of the exponential fits for 0.9 TeV, 7 TeV and 7 TeV high-multiplicity data, respectively. The results are compared to the corresponding measurements by the E735 experiment at the Tevatron [51], and by the STAR experiment at RHIC [52]. The error bars represent the quadratic sum of the statistical and systematic uncertainties.

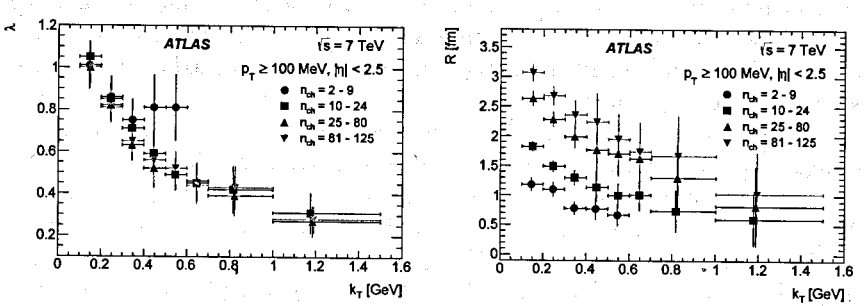

(a) (b)

Figure 4: The k_T dependence of the fitted parameters (a) λ and (b) R obtained from the exponential fit to the two-particle double-ratio correlation function $R_2(Q)$ at $\sqrt{s} = 7$ TeV for the different multiplicity regions: $2 \leq n_{ch} \leq 9$ (circles), $10 \leq n_{ch} \leq 24$ (squares), $25 \leq n_{ch} \leq 80$ (triangles) and $81 \leq n_{ch} \leq 125$ (inverted triangles). The average transverse momentum k_T of the particle pairs is defined as $k_T = |\mathbf{p}_{T,1} + \mathbf{p}_{T,2}|/2$. The error bars represent the quadratic sum of the statistical and systematic uncertainties.

The R-parameter decreases with k_T and exhibits an increase with increasing multiplicity as was observed for the fully inclusive case.

6 Conclusions

The two-particle Bose–Einstein correlations of like-sign hadrons with $p_T >$ 100 MeV and $|\eta| < 2.5$ produced in pp collisions recorded by the ATLAS detector at 0.9 and 7 TeV at the CERN Large Hadron Collider are studied. In addition to minimum-bias data, high-multiplicity data recorded at 7 TeV using a dedicated trigger are investigated. The integrated luminosities are about 7 μb^{-1}, 190 μb^{-1} and 12.4 nb^{-1} for 0.9 TeV, 7 TeV minimum-bias and 7 TeV high-multiplicity data samples, respectively. The studies were performed using the double-ratio correlation function. In the double-ratio method, the single-ratio correlation function obtained from the data is divided by a similar single-ratio calculated using Monte Carlo events, which do not have BEC effects. The reference sample for each of the two single-ratios is constructed from unlike-sign charged-particle pairs. The BEC parameters are studied as a function of the charged-particle multiplicity and the transverse momentum of the particle pair. A decrease of the correlation strength λ along with an increase of the correlation source size parameter R are found with increasing charged-particle multiplicity. On the other hand no dependence of R on the centre-of-mass energy of pp collisions is observed. For the first time a saturation of the source size parameter is observed for multiplicity $n_{ch} \geq 55$. The correlation strength λ and the source size parameter R are found to decrease with increasing average transverse momentum of a pair. The study of BEC in (n_{ch}, k_T) bins at 7 TeV shows a decrease of the R parameter with k_T for different multiplicity ranges, while the R values increase with multiplicity. The λ parameter is found to decrease with k_T independently of the multiplicity range. These resemble the dependences for the inclusive case at 7 TeV for minimum-bias and high-multiplicity data.

References

[1] R. Hanbury Brown and R.Q. Twiss, Phil. Mag. **45**, 663 (1954)

[2] G.I. Kopylov and M.I. Podgoretskiĭ, Sov. J. Nucl Phys. **18**, 336 (1974)

[3] E.V. Shuryak, Phys. Lett. B **44**, 387 (1973)

[4] G. Cocconi, Phys. Lett. B **49**, 459 (1974)

[5] G. Goldhaber *et al.*, Phys. Rev. **120**, 300 (1960)

[6] S. Barshay, Phys. Lett. B **130**, 220 (1983)

[7] N. Suzuki, M. Biyajima, Phys. Rev. C **60**, 034903 (1999)

[8] B. Buschbeck, H.C. Eggers, P. Lipa, Phys. Lett. B **481**, 187 (2000)

[9] G. Alexander, E.K.G. Sarkisyan, Phys. Lett. B **487**, 215 (2000)

[10] OPAL Collaboration, Z. Phys. C **72**, 389 (1996)

[11] G. Alexander, J. Phys. G **39**, 085007 (2012)

[12] Yu.M. Sinyukov, V.M. Shapoval, Phys. Rev. D **87**, 094024 (2013) [13]

V.M. Shapoval, *et al.*, Phys. Lett. B **725**, 139 (2013)

[14] Yu.M. Sinyukov, *et al.*, Adv. High Energy Phys. **2013**, 198928 (2013)

[15] V. A. Schegelsky, *et al.*, Phys. Lett. B **703**, 288 (2011)

[16] M.Ryskin, V.Schegelsky, Nucl.Phys.Proc.Suppl. **219-220**, 10 (2011) [17]

For review see: E. Shuryak, arXiv:1412.8393.

[18] ATLAS Collaboration, JINST **3**, S08003 (2008).

[19] L. Evans and P. Bryant (editors) 2008 JINST 3 S08001

[20] ATLAS Collaboration, Eur. Phys. J. C **75**, no. 10, 466 (2015)

[21] CMS Collaboration, Phys. Rev. Lett. **105**, 032001 (2010)

[22] Particle Data Group Chin. Phys. C **38**, 090001 (2014)

[23] CMS Collaboration, J. High Energy Phys. **05**, 029 (2011)

[24] ALICE Collaboration, Phys. Rev. D **82**, 052001 (2010)

[25] ALICE Collaboration, Phys. Rev. D **84**, 112004 (2011)

[26] M. Deutschmann *et al.*, Nucl. Phys. B **204**, 333 (1982)

[27] M. Gyulassy, *et al.*, Phys. Rev. C **20**, 2267 (1979)

[28] S. Pratt, Phys. Rev. D **33**, 72 (1986)

[29] I. Juricic, *et al.*, Phys. Rev. D **39**, 1 (1989)

[30] R.M. Weiner, Phys. Rep. **327**, 249 (2000)

[31] G.I. Kopylov, Phys. Lett. B **50**, 472 (1974)

[32] W. Kittel and E.A. De Wolf, *Soft Multihadron Dynamics* (World Scientific, Singapore, 2005)

[33] P. Grassberger, Nucl. Phys. B **120**, 231 (1977)

[34] M. Gyulassy and S. S. Padula, Phys. Lett. B **217**, 181 (1989)

[35] S. S. Padula and M. Gyulassy, Nucl. Phys. A **498**, 555C (1989)

[36] K. Kulka and B. Lörstad, Z. Phys. C **45**, 581 (1990)

[37] M.G Bowler, Z. Phys. C **46**, 305 (1990)

[38] R. Lednický and T.B. Progulova, Z. Phys. C **55**, 295 (1992)

[39] S.S. Padula and M. Gyulassy, Nucl. Phys. A **544**, 537c (1992)

[40] ATLAS Collaboration, ATLAS-LARG-PUB-2008-002 (2008).

[41] ATLAS Collaboration, Phys. Lett. B **688**, 21 (2010)

[42] ATLAS Collaboration, New J. Phys. **13**, 053033 (2011)

[43] G. Piacquadio, *et al.*, J. Phys. Conf. Ser. **119**, 032033 (2008)

[44] ATLAS Collaboration, ATLAS-CONF-2010-027 (2010)

[45] T. Sjöstrand, *et al.*, J. High Energy Phys. **05**, 026 (2006)

[46] ATLAS Collaboration, ATL-PHYS-PUB-2010-002 (2010).

[47] ATLAS Collaboration, Eur. Phys. J. C **70**, 823 (2010)

[48] GEANT4 Collaboration, Nucl. Instrum. Methods A **506**, 250 (2002)

[49] G. D' Agostini, Nucl. Instr. Meth. A **362**, 487 (1995)

[50] UA1 Collaboration, Phys. Lett. B **226**, 410 (1989)

[51] T. Alexopoulos *et al.*, Phys. Rev. D **48**, 1931 (1993)

[52] STAR Collaboration, Phys. Rev. C **83**, 064905 (2011)

SECTION "ADVANCES IN THEORETICAL PHYSICS"

Near-mass-shell form factor f_- of the pion β-decay

M. I. Krivoruchenko[a,b,c]

[a]Institute for Theoretical and Experimental Physics
B. Cheremushkinskaya 25, 117218 Moscow, Russia
[b]Moscow Institute of Physics and Technology
141700 Dolgoprudny, Russia
[c]Bogoliubov Laboratory of Theoretical Physics, JINR
141980 Dubna, Russia

Abstract

The generalized Ward-Takahashi identity (gWTI) in the pion sector for broken isotopic symmetry is derived and used for the model-independent estimate of the longitudinal form factor f_- of the π_{e3} weak vector vertex. The on-shell f_- is found to be proportional to the mass difference of the pions and the difference between the vector isospin $T=1$ and scalar isospin $T=2$ pion radii. Off-shell form factors are in general ambiguous because of the gauge dependence and the freedom in the parameterization of the fields. The near-mass-shell f_- appears to be an exception, allowing for experimental verification of the consequences of the gWTI. We calculate the near-mass-shell f_- using the gWTI and dispersion techniques. The results are discussed in the context of the conservation of vector current (CVC) hypothesis.

1. Introduction

The pion β-decay decay (π_{e3}) is one of the main semileptonic electroweak processes. The vector nature of the transition, its simple kinematics, and the precise measurement of the partial width make this decay particularly attractive for testing the Standard Model.

Radiative corrections and pion structure effects in the π_{e3} decay have been calculated with high accuracy [1-4], sufficient for verification of the unitarity of the CKM matrix. The experimental data, however, are not yet sufficiently precise for this purpose. Measurements of the π_{e3} decay are also motivated by the possibility of testing the conservation of vector current (CVC) in the meson sector.

The CVC hypothesis [5-7] suggests that the isovector component of the electromagnetic current and the charged components of the weak vector current belong to the same isospin triplet. In the limit of exact isotopic symmetry, conservation of the electromagnetic current implies conservation of the weak vector current.

Off the mass shell, the CVC is equivalent to the Ward-Takahashi identity (WTI) for the isospin $SU(2)$ group. The WTI, however, is of greater generality and leads to useful relationships between off-shell form factors, including those that vanish when some of the external legs are on shell. The violation of isotopic

symmetry, associated with the small mass difference between the up and down quarks and the electromagnetic and weak interactions, results in the non-conservation of the charge-changing components of the weak vector current. For the broken symmetry, the CVC condition and the WTI are replaced by partial CVC and the generalized WTI (gWTI), which are especially sensitive to the pattern of isotopic symmetry breaking.

The parameterization of the degrees of freedom associated with the pion field can be performed in various ways, which produces off-shell ambiguity in the amplitudes. The on-shell form factors are related to the asymptotic states and are uniquely defined. This statement is known as the equivalence theorem (ET) [8-10]. The off-shell form factors depend on this parameterization and cannot be measured experimentally [11-12].

A notable exception to this rule is established in Ref. [13]. The longitudinal part of the π_{e3} vertex appears to be uniquely defined near the mass shell and accessible to measurements. As an application of the gWTI, we derive a model-independent expression for the longitudinal form factor f_- and provide its numerical estimate.

2. *U*(1) vector vertex

The on-shell conserved vector current of a charged scalar particle (π^+) is determined by one form factor. Off the mass shell, there are two form factors. In the most general case, the current can be written as follows

$$\Gamma_\mu(p',p)=(p'+p)_\mu\mathcal{F}_1+q_\mu(p'^2-p^2)\mathcal{F}_2, \qquad (1)$$

where $q=p'-p$ is the momentum transfer. The form factors $\mathcal{F}_i$ are symmetric functions of p'^2 and p^2 and arbitrary functions of q^2 and the physical mass m of the charged pion. The factor p'^2-p^2 in the second term is added to ensure the negative C parity of the vertex. The decomposition (1) arises e.g., in the scalar quantum electrodynamics. The WTI of the $U(1)$ symmetry group establishes a relationship between $\mathcal{F}_1$ and $\mathcal{F}_2$:

$$q^2\mathcal{F}_2(p'^2,p^2,q^2)=\frac{\Delta^{-1}(p')-\Delta^{-1}(p)}{p'^2-p^2}-\mathcal{F}_1(p'^2,p^2,q^2), \qquad (2)$$

where $\Delta(p)=p^2-m^2-\Sigma(p^2,m)$ is the renormalized pion propagator, $\Sigma(p^2,m)$ is the self-energy operator. In the limit $p'^2=p^2=m^2$, we obtain

$$\mathcal{F}_2(m^2,m^2,q^2)=\frac{1-\mathcal{F}_1(m^2,m^2,q^2)}{q^2}.$$

In the vicinity of $q^2=0$, the form factor $\mathcal{F}_1$ can be expanded to give

$$\mathcal{F}_2(m^2,m^2,0)=-\frac{1}{6}\langle r^2\rangle_v,$$

where $\langle r^2\rangle_v$ is the vector charge radius of π^+.

The equivalence of the Coulomb and Lorentz gauges in QED was rigorously proved by Bialynicki-Birula [14]. On shell, the amplitudes are gauge-invariant, whereas the off-shell dependence on the gauge persists. $\mathcal{F}_1$ and $\mathcal{F}_2$ are thus uniquely defined, when both legs of the charged pion are on the mass shell. To first order in the displacement from the mass shell, the longitudinal component of the vertex is also gauge invariant, as is evident from Eq. (1).

$\mathcal{F}_2$ with two on-shell legs $p'^2=p^2=m^2$ does not contribute to the current. Off the mass shell, however, $\mathcal{F}_2$ does contribute, and its contribution is uniquely determined by the WTI. Isotopic rotation of $\mathcal{F}_2$ is not sufficient to obtain a full weak-interaction vertex. We show that the violation of isotopic symmetry generates an isospin $T=2$ contribution that is unrelated to isotopic rotation.

3. *SU*(2) vector vertex

The $SU(2)$ vector vertex expansion in scalar functions $\mathcal{F}^a_{i\pm}(p'^2,p^2,q^2)$ that are symmetric in p'^2 and p^2 takes the form

$$\Gamma^a_\mu(p',p)=(p'+p)_\mu\left(\mathcal{F}^a_{1-}+(p'^2-p^2)\mathcal{F}^a_{1+}\right)+q_\mu\left((p'^2-p^2)\mathcal{F}^a_{2-}+\mathcal{F}^a_{2+}\right), \qquad (3)$$

The lower index $\pm$ indicates the symmetry with respect to permutation of the isospin indices: $\tilde{\mathcal{F}}^a_{i\pm}=\pm\mathcal{F}^a_{i\pm}$.

If there were no isospin symmetry breaking, we could have $\mathcal{F}^a_{i-}=T^a\mathcal{F}_{i-}$, as there are no other $SU(2)$ generators, and $\mathcal{F}^a_{i+}=0$, implying that $\Gamma^a_\mu(m^2,m^2,q^2)\propto T^a$.

In order to find relationships for $\mathcal{F}^a_{i\pm}(p'^2,p^2,q^2)$, we derive a generalization of the WTI associated with the replacement of the exact $U(1)$ symmetry by the broken $SU(2)$ symmetry. Using the gWTI gives

$$\mathcal{F}^a_{2+}(m^2,m^2,q^2) = [m^2+\Sigma(m^2),T^a]\frac{1/D_J^{T=2}(q^2)-1}{q^2}, \qquad (4)$$

$$\mathcal{F}^a_{2-}(m^2,m^2,q^2) = T^a\frac{1-\mathcal{F}_{1-}(m^2,m^2,q^2)}{q^2}. \qquad (5)$$

As a consequence of elastic unitarity and analyticity, the q^2 dependence of the on-mass-shell form factor $\mathcal{F}^a_{2+}$ is determined by the Jost function

$$D^T_f(s) = \exp\left(-\frac{s}{\pi}\int_{4m^2}^{+\infty}\frac{\delta^T(s')ds'}{s'(s'-s)}\right), \quad (6)$$

that can be constructed in terms of the phase shift in the corresponding channel; here, the S-wave $T=2$ channel of the pion-pion scattering is relevant.

The on-shell weak vector current is usually parameterized in the form

$$\langle\pi^0(p')|\bar{d}\gamma_\mu(1-\gamma_5)u|\pi^+(p)\rangle = \sqrt{2}((p'+p)_\mu f_+ + q_\mu f_-), \quad (7)$$

where $q_\mu = (p'-p)_\mu$.

The exact CVC condition implies

$$f_- = 0. \quad (8)$$

Partial CVC yields

$$f_- = \frac{m^2_{\pi^+} - m^2_{\pi^0}}{6}\left(\langle r^2\rangle^{T=1}_v - \langle r^2\rangle^{T=2}_s\right). \quad (9)$$

The isovector radius squared is determined by the electromagnetic form factor of the charged pion, whereas the isotensor one can be found from the low-q^2 expansion of the Lorentz scalar $\pi^+\pi^0$ transition form factor. Remarkably, for a dressed vertex, the $W^\pm$ boson, being a member of the weak isospin triplet, is coupled to both the strong isospin triplet and the strong isospin quintet.

The WTI of exact symmetry implies, to first order in the displacement $p'^2 - p^2$ and for low momentum transfers,

$$f_- = -\frac{p'^2 - p^2}{6}\langle r^2\rangle^{T=1}_v. \quad (10)$$

The WTI of broken symmetry implies, to first order in $\Delta m^2_\pi = m^2_{\pi^0} - m^2_{\pi^+}$ and the displacement $p'^2 - p^2$ and for low momentum transfers,

$$f_- = -\frac{p'^2 - p^2}{6}\langle r^2\rangle^{T=1}_v + \frac{m^2_{\pi^0} - m^2_{\pi^+}}{6}\langle r^2\rangle^{T=2}_s. \quad (11)$$

The on-shell form factor $\mathcal{F}^a_{1-}$ is independent of both the gauge and the parameterization. By virtue of Eqs. (4) and (5), the on-shell form factors $\mathcal{F}^a_{2\pm}$ are also uniquely defined. The longitudinal component of the vertex ((3)) contains the factor $p'^2 - p^2$ in $\mathcal{F}^a_{2-}$, whereas $\mathcal{F}^a_{2+}$ has smallness of $O(\Delta m^2_\pi)$. We thus conclude that the longitudinal component of $\Gamma^a_\mu(p', p)$ is uniquely defined in

the neighborhood of the mass shell to first order in the pion mass splitting and the displacement $p'^2 - p^2$. In the neighborhood of the mass shell, the longitudinal form factor f_- escapes the general rule [8-13] that states that off-shell amplitudes are ambiguous.

The results obtained for the near-mass-shell representation of f_- in terms of the physical masses and radii of the pions exhibit explicit independence on the gauge and the parameterization of the pion field.

The generality of the relationships (9) and (11) is influenced by only the CVC condition at a bare interaction vertex. This condition is satisfied in the Standard Model, so any violation of these relationships can be interpreted as an indication for new physics at or above the electroweak scale.

4. Numerical estimates

Experimental value of the π^+ charge radius equals [15]

$$\langle r^2\rangle^{T=1}_v = (0.672 \pm 0.008\,\text{fm})^2.$$

We employ the dispersion techniques for numerical estimation of the pion radius $\langle r^2\rangle^{T=2}_s$, entering the equations (9) and (11). Expanding the Jost function in the vicinity of $s=0$, we obtain

$$\langle r^2\rangle^T_s = \frac{6}{\pi}\int_{4m^2}^{+\infty}\frac{\delta^T(s')}{s'^2}ds'. \quad (12)$$

The phase shifts between the experimental points of Refs. [15-17] are interpolated linearly. We obtain the value

$$\langle r^2\rangle^{T=2}_s = -0.10 \pm 0.05\,\text{fm}^2$$

and, with the help of Eq. (9),

$$f_- = (2.97 \pm 0.25)\times 10^{-3}. \quad (13)$$

This result is a factor of two greater than the light-front quark model prediction [3].

Contribution of the longitudinal form factor to the pion β-decay rate can be estimated to give $\Delta B/B = -0.94\times 10^{-3} f_-$; the additional small factor in f_- arises for kinematic reasons. The experimental error in B is 0.6% [15]. We thus reaffirm earlier conclusions that f_- is currently beyond the capabilities of the experimental study. The possibility of measuring the longitudinal weak vector current in the neutron β-decay [19], muon capture [20] and in the $\tau^- \to \pi^-\pi^0\nu_\tau$ and $\tau^- \to K^-K^0\nu_\tau$ decays could be more promising.

5. Conclusion

A generalization of the WTI was derived in the pion sector to account for the isotopic symmetry breaking. It was shown that the isovector $T=1$ part of the

current can be reconstructed through isotopic rotation of the off-shell pion electromagnetic form factors, whereas the isotensor $T = 2$ part has no analogs but rather is uniquely determined by the gWTI combined with the elastic unitarity, analyticity, and the pion-pion scattering data.

The various versions of the CVC condition are distinguished depending on whether the isotopic symmetry is exact or broken and whether the outer legs in the vertex are on or off shell. The corresponding predictions for the longitudinal form factor f_- are given in Eqs. (8), (9), (10), and (11). In the case of the exact isotopic symmetry, the bare and dressed weak vertices are pure isospin triplets; the CVC and the WTI hold on and off shell, respectively. In the case of the broken isotopic symmetry, the dressed weak vertex is no longer a pure isospin triplet; partial CVC and the gWTI hold on and off shell.

To first order in the pion mass splitting and the displacement from the mass shell, the longitudinal component is independent of both the gauge and the parameterization, and therefore, the near-mass-shell form factor f_- appears to be a unique object whose properties are unambiguously determined by the partial CVC condition (the gWTI).

Acknowledgments

This work was supported by RFBR Grant No. 13-02-01442 and Grant No. HLP-2015-18 of the Heisenberg-Landau Program.

References

[1] A. Sirlin, Rev. Mod. Phys. **50** (1978) 573 [Erratum ibid. **50** (1978) 905].
[2] V. Cirigliano, M. Knecht, H. Neufeld, H. Pichl, Eur. Phys. J. C **27** (2003) 255.
[3] W. Jaus, Phys. Rev. D **60** (1999) 054026.
[4] W. Jaus, Phys. Rev. D **63** (2001) 053009.
[5] S. S. Gerstein and Ya. B. Zeldovich, ZhETF **29** (1955) 698 [in Russian].
[6] S. S. Gerstein and Ya. B. Zeldovich, Sov. JETP **2** (1956) 576.
[7] R. P. Feynman, M. Gell-Mann, Phys. Rev. **109**, 193 (1958).
[8] R. Haag, Phys. Rev. **112** (1958) 669.
[9] J. S. R. Chisholm, Nucl. Phys. **26** (1961) 469.
[10] S. Kamefuchi, L. O'Raifeartaigh, and A. Salam, Nucl. Phys. **28** (1961) 529.
[11] H. W. Fearing, Few-Body Syst. Suppl. **12** (2000) 263.
[12] H. W. Fearing, S. Scherer, Phys. Rev. C **62** (2000) 034003.
[13] M. I. Krivoruchenko, Adv. High Energy Phys. **2015** (2015) 656239.
[14] I. Bialynicki-Birula, Phys. Rev. D **12** (1970) 2877.
[15] K. A. Olive et al. (Particle Data Group), Chin. Phys. C **38** (2014) 090001.
[16] D. Cohen, T. Ferbel, P. Slattery, and B. Werner, Phys. Rev. D **7** (1973) 661.
[17] N. B. Durusoy et al., Phys. Lett. B **45** (1973) 517.
[18] W. Hoogland et al., Nucl. Phys. B **126** (1977) 109.
[19] H. Abele, Prog. Part. Nucl. Phys. **60** (2008) 1.
[20] D. Gazit, Phys. Lett. B **666** (2008) 472.

Left-left squark mixing in the $K^+ \to \pi^+ \nu\bar{\nu}$ decay

Tomáš Blažek* and Peter Maták†

Comenius University in Bratislava, Slovak Republic

Abstract

We study the effects of supersymmetry with non-minimal flavor violation in the rare kaon decay, $K^+ \to \pi^+ \nu\bar{\nu}$. Focusing on the role of the left-left mass matrix elements of the up type squarks we perform the numerical scan through the MSSM parameter space. We demonstrate that in case of the large stop trilinear couplings the observable deviations from the standard model branching ratio are still possible. This study extends our earlier analyses and provides new updated results.

1 Introduction

In the standard model effective theory, there is only one dimension-six effective operator,

$$\mathcal{O}_L = (\bar{s}\gamma^\mu P_L d)(\bar{\nu}_l \gamma_\mu P_L \nu_l), \tag{1}$$

contributing to the amplitude of $K^+ \to \pi^+ \nu\bar{\nu}$. New physics in general introduces $\mathcal{O}_R$ with the right-handed quarks in the first bilinear. Then, the short-distance effects are represented by the effective Lagrangian [1–3]

$$\mathcal{L}_{\text{s.d.}} = \frac{4G_F}{\sqrt{2}} \frac{\alpha}{2\pi \sin^2\theta_W} \sum_{l=e,\mu,\tau} (X_L \mathcal{O}_L + X_R \mathcal{O}_R). \tag{2}$$

With the approximate isospin symmetry, the non-perturbative matrix elements of this operator can be extracted from the tree-level $K^+ \to \pi^0 e^+ \nu_e$ decay [4]. The precise way in which the Wilson coefficients $X_{L,R}$ enter the branching ratio is straightforward and can be found in Ref. 5, where further references are given. In the following we are only interested in a way in which new physics, supersymmetry in particular, modifies the value of $X = X_L + X_R$.

*blazek@fmph.uniba.sk
†peter.matak@fmph.uniba.sk

For the standard model case, this quantity has been calculated, including NLO QCD [6] and two-loop electroweak [7] corrections, leading to $X_{SM} = 1.481 \pm 0.005_{\text{th.}} \pm 0.008_{\text{exp.}}$ [5] and the branching ratio [5]

$$\mathcal{B}(K^+ \to \pi^+ \nu\bar{\nu})_{\text{SM}} = (7.62^{+0.69}_{-0.70}) \times 10^{-11}. \tag{3}$$

On the experimental side, the value measured by E-787, E-949 at Brookhaven equals [8,9]

$$\mathcal{B}(K^+ \to \pi^+ \nu\bar{\nu})_{\text{exp.}} = (1.73^{+1.15}_{-1.05}) \times 10^{-10}. \tag{4}$$

The NA62 experiment at CERN started taking data recently and is expected to improve the measured branching fraction aiming at a 10% uncertainty of the standard model value. Almost any new physics containing flavored degrees of freedom, if discovered at the LHC, will be effectively constrained by Flavor Changing Neutral Currents (FCNC), among which the $K^+ \to \pi^+ \nu\bar{\nu}$ decay plays a very important role.

2 Supersymmetry in charged kaon decay

Supersymmetry affects the FCNC amplitudes in two different ways. First, even in the minimal model, it increases the number of flavor changing loops containing contributions of the scalar partners and additional Higgs bosons. After the quark fields are rotated to their mass eigenstates, the CKM factors appear in the vertices of new particles, contributing to the flavor changing amplitudes in a similar way, as it is in the standard model.

However, quark and squark mass matrices are not necessarily flavor-diagonal in the same basis. By rotating scalars in the same way as their standard model counterparts we obtain the so-called super-CKM basis. The complete squark mass matrices have the general form

$$\mathcal{M}^2_{\tilde{q}} = \begin{pmatrix} \mathcal{M}^2_{\tilde{q},LL} & \mathcal{M}^2_{\tilde{q},LR} \\ \mathcal{M}^2_{\tilde{q},RL} & \mathcal{M}^2_{\tilde{q},RR} \end{pmatrix}, \tag{5}$$

where each block represents 3×3 matrix in the family space. We keep in mind that left-handed up- and down-type squarks come from the same isospin doublet and therefore, their left-left blocks cannot be independent. Instead, they are subject to following constraints

$$\mathcal{M}^2_{\tilde{u},LL} = V_{CKM} \mathcal{M}^2_{\tilde{d},LL} V_{CKM}{}^\dagger. \tag{6}$$

According to the standard notation, we introduce dimensionless parameters originating in general flavor structure of the soft supersymmetry breaking terms,

$$\delta^{ij}_{\tilde{q}XY} = \frac{(\mathcal{M}^2_{\tilde{q},XY})^{ij}}{\sqrt{(\mathcal{M}^2_{\tilde{q},XX})^{ii} (\mathcal{M}^2_{\tilde{q},YY})^{jj}}}, \tag{7}$$

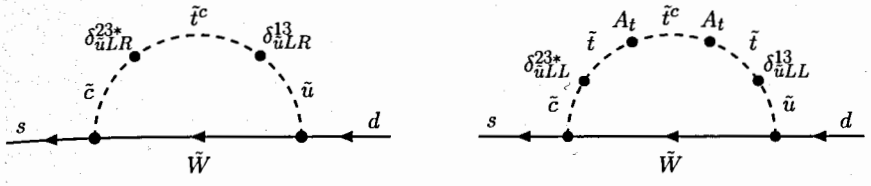

Figure 1: Chargino and stop contribution to the kaon decay amplitude in the mass insertion approximation [1, 16]. The loops represent the entire group of diagrams, in which Z^0 propagator connects to any of the stop, chargino, or quark line.

$\lvert V_{us}\rvert = 0.2253 \pm 0.0008$ [17]	$\lvert V_{ub}\rvert = (3.28 \pm 0.29) \times 10^{-3}$ [18]
$\lvert V_{cb}\rvert = (38.94 \pm 0.76) \times 10^{-3}$ [18]	$\gamma = (73.2^{+6.3}_{-7.0})^\circ$, [19]
$\mathcal{B}(B \to X_s\gamma) = (3.12 \pm 0.23) \times 10^{-4}$ [20]	$\varepsilon_K = (2.23 \pm 0.25) \times 10^{-3}$ [5,17]
$\mathcal{B}(B^0 \to \mu\mu) = (3.9 \pm 1.6) \times 10^{-10}$ [18]	$\Delta M_d = 0.506 \pm 0.090\ \text{ps}^{-1}$ [18]
$\mathcal{B}(B^0_s \to \mu\mu) = (3.1 \pm 0.5) \times 10^{-9}$ [18]	$\Delta M_s = 17.757 \pm 2.37\ \text{ps}^{-1}$ [18]

Table 1: The flavor changing constraints used in the numerical analysis. The values of the $\lvert V_{ub}\rvert$ and $\lvert V_{cb}\rvert$ CKM elements come from the exclusive measurement of $\bar{B} \to \pi l^- \bar{\nu}$ and $\bar{B} \to D^* l^- \bar{\nu}$ decays, respectively [18].

with $i \neq j$ being flavor indices, while X, Y equals L or R denoting scalar partners of quarks with different chiralities. Hermiticity of 5 requires $\delta_{\tilde{q},RL} = \delta_{\tilde{q},LR}{}^\dagger$.

In the literature the dependence of the kaon decay amplitude on the $\delta_{\tilde{u},RL}$ has been investigated in a detail [1, 10–13]. However, this mass insertions are constrained by the vacuum stability bounds [14, 15] and for the current limits on the stop and chargino masses their effects are rather limited. Instead, as we suggested in our previous analysis [16], for the large values of the soft supersymmetry breaking stop trilinear coupling A_t, motivated by the observed value of the Higgs mass, the non-negligible effect may come from the left-left block of the squark mass matrix 5. In the mass insertion approximation, this contribution can be represented by the second loop diagram in Figure 1.

For our numerical analysis publicly available program `SUSY_FLAVOR 2.54` [21–23] has been used. The CKM parameters as well as the experimental constraints that we have taken into account are listed in table 1. Regarding the supersymmetric parameters, we used the unification condition for gaugino masses, $M_2 = 700$ GeV and $M_3 = 3000$ GeV. Such a heavy gluinos make the gluino loops almost irrelevant for the kaon decay itself. On the other hand, the constraints coming from meson mixing processes are partialy reduced. Higgsino mass has been fixed at $\mu = 700$ GeV, while the diagonal squark soft masses were $m_{\tilde{Q}} = m_{\tilde{q}} = 1.3$ TeV. We have performed numerical scan through the values $\tan\beta \in \langle 3, 7\rangle$ and $\lvert A_t\rvert \in \langle 2.5, 3.5\rangle$ TeV. Finally, the left-left mass squark insertions